Antenna Arraying Techniques in the Deep Space Network

David H. Rogstad
Alexander Mileant
Timothy T. Pham

MONOGRAPH 5
DEEP SPACE COMMUNICATIONS AND NAVIGATION SERIES

Antenna Arraying Techniques in the Deep Space Network

DEEP SPACE COMMUNICATIONS AND NAVIGATION SERIES

Issued by the Deep Space Communications and Navigation Systems
Center of Excellence
Jet Propulsion Laboratory
California Institute of Technology

Joseph H. Yuen, Editor-in-Chief

Previously Published Monographs in this Series

1. *Radiometric Tracking Techniques for Deep-Space Navigation*
C. L. Thornton and J. S. Border

2. *Formulation for Observed and Computed Values of Deep Space Network Data Types for Navigation*
Theodore D. Moyer

3. *Bandwidth-Efficient Digital Modulation with Application to Deep-Space Communications*
Marvin K. Simon

4. *Large Antennas of the Deep Space Network*
William A. Imbriale

Antenna Arraying Techniques in the Deep Space Network

David H. Rogstad
Alexander Mileant
Timothy T. Pham

Jet Propulsion Laboratory
California Institute of Technology

MONOGRAPH 5
DEEP SPACE COMMUNICATIONS AND NAVIGATION SERIES

Antenna Arraying Techniques in the Deep Space Network
(JPL Publication 03-001)

January 2003

The research described in this publication was carried out at the
Jet Propulsion Laboratory, California Institute of Technology, under
a contract with the National Aeronautics and Space Administration.

Table of Contents

Foreword

The Deep Space Communications and Navigation Systems Center of Excellence (DESCANSO) was established in 1998 by the National Aeronautics and Space Administration (NASA) at the California Institute of Technology's Jet Propulsion Laboratory (JPL). DESCANSO is chartered to harness and promote excellence and innovation to meet the communications and navigation needs of future deep-space exploration.

DESCANSO's vision is to achieve continuous communications and precise navigation—any time, anywhere. In support of that vision, DESCANSO aims to seek out and advocate new concepts, systems, and technologies; foster key technical talents; and sponsor seminars, workshops, and symposia to facilitate interaction and idea exchange.

The Deep Space Communications and Navigation Series, authored by scientists and engineers with many years of experience in their respective fields, lays a foundation for innovation by communicating state-of-the-art knowledge in key technologies. The series also captures fundamental principles and practices developed during decades of deep-space exploration at JPL. In addition, it celebrates successes and imparts lessons learned. Finally, the series will serve to guide a new generation of scientists and engineers.

Joseph H. Yuen
DESCANSO Leader

Preface

This monograph provides an introduction to the development and use of antenna arraying in the Deep Space Network (DSN). It is intended to serve as a starting point for anyone wishing to gain an understanding of the techniques that have been analyzed and implemented. A complete discussion of the general subject of arraying has not been provided. Only those parts relevant to what has been used in the DSN have been included.

While baseband arraying, symbol combining, and carrier arraying were discussed and developed fairly early in the history of the DSN, it wasn't until the failure of the main antenna onboard the Jupiter-bound Galileo spacecraft that arraying antennas became more critical. In response to this crisis, two methods were analyzed: full-spectrum arraying and complex-symbol combining. While both methods were further developed, it was full-spectrum arraying that was finally implemented to support the Galileo data playback. This effort was so successful that a follow-on implementation of full-spectrum arraying was begun that provided for much higher data rates than for the Galileo Mission and allowed for arraying of up to six antennas within the Goldstone Complex. In addition to providing a backup to the 70-m antenna, this array (the Full Spectrum Processing Array, or FSPA) allows future missions to use a varying number of antennas as a function of time, and thereby to optimize the use of resources. This capability is also being implemented at the other DSN complexes.

We present here a description of this development, including some historical background, an analysis of several methods of arraying, a comparison of these methods and combinations thereof, a discussion of several correlation techniques used for obtaining the combining weights, the results of several arraying experiments, and some suggestions for future work. The content has been drawn from the work of many colleagues at JPL who have participated in

the effort to develop arraying techniques and capabilities. We are indebted to the large number of scientists, engineers, testers, and operators who have played a crucial role in the implementation of antenna arraying in the DSN. Finally, we acknowledge the primary role of NASA, its Deep Space Network, and especially the Galileo Project in the development of this exciting capability.

David H. Rogstad
Alexander Mileant
Timothy T. Pham

Acknowledgments

We are especially grateful, and wish to dedicate this work, to George M. Resch (1941–2001) for his untiring support in pursuing the use of very long baseline interferometry (VLBI) techniques and equipment to implement full-spectrum arraying. His encouragement and expertise led to its being developed originally as a technology project and finally as a method to enhance telemetry for the Galileo Project.

We would also like to express our appreciation to the large number of people who have contributed to arraying development in the DSN, and consequently to many parts of this monograph on the subject. While it is not possible to name everyone, certain individuals deserve special mention because of their key contribution to the preparation of the material presented here: Roger A. Lee, Robert Kahn, Andre Jongeling, Sue Finley, Dave Fort, William Hurd, James Ulvestad, Biren Shah, Sampson Million, and Joseph Statman. One individual who deserves special acknowledgment is Sami Hinedi. His work, together with that of one of the authors (Alexander Mileant), provided the basis for much of the receiver and array analysis presented in Chapters 5 through 7.

Chapter 1
Introduction

As the signal arriving from a receding deep-space spacecraft becomes weaker and weaker, the need arises for devising schemes to compensate for the reduction in signal-to-noise ratio (SNR). With maximum antenna apertures and lower receiver noise temperatures pushed to their limits, one remaining method for improving the effective SNR is to combine the signals from several antennas. This is referred to as arraying, and it has enabled the National Aeronautics and Space Administration (NASA) Deep Space Network (DSN) to extend the missions of some spacecraft beyond their planned lifetimes. A related benefit provided by arraying has been its ability to receive higher data rates than can be supported with a single antenna. As an example, symbol-stream combining was used to array symbols between the Very Large Array (VLA) radio telescope, located in New Mexico, and Goldstone's antennas, located in California, during Voyager's encounter at Neptune [1,2]. That technique increased the scientific return from the spacecraft by allowing data transmission at a higher rate. In general, arraying enables a communication link to operate in effect with a larger antenna than is physically available.

Antenna arraying can be employed with any signal modulation format, be it binary phase-shift keying (BPSK), quadrature phase-shift keying (QPSK), continuous phase modulation (CPM), etc. In this discussion, the NASA standard deep-space signal format will be used to illustrate the different arraying techniques, but the results can be extended to other formats, including suppressed carrier.

This monograph compares the various arraying algorithms and techniques by unifying their analyses and then discussing their relative advantages and disadvantages. The five arraying schemes that can be employed in receiving signals from deep-space probes are treated. These include full-spectrum combining (FSC), complex-symbol combining (CSC), symbol-stream

combining (SSC), baseband combining (BC), and carrier arraying (CA). In addition, sideband aiding (SA) is also included and compared even though it is not an arraying scheme since it employs a single antenna. Combinations of these schemes are also discussed, such as carrier arraying with sideband aiding and baseband combining (CA/SA/BC) or carrier arraying with symbol-stream combining (CA/SSC), just to name a few. We discuss complexity versus performance trade-offs, and the benefits of reception of signals from existing spacecraft. It should be noted here that only the FSC method has application for arraying of signals that are not telemetry. Consequently, all of the analysis and comparisons referred to above are done using telemetry signals. There is no reason to believe that the performance of FSC on non-telemetry signals will not yield similar results.

The most recent implementation of arraying for telemetry within the DSN is the Goldstone array [3], which supports full-spectrum combining of up to six antennas within the complex. Specific techniques that are used in this array are discussed, and results from several experiments are presented. Finally, directions for future research and implementation are discussed.

1.1 Benefits of Arraying

Arraying holds many tantalizing possibilities: better performance, increased operational robustness, implementation cost saving, more programmatic flexibility, and broader support to the science community. Each of these topics is discussed further in the following sections.

1.1.1 Performance Benefits

For larger antennas, the beamwidth naturally is narrower. As a result, antenna-pointing error becomes more critical. To stay within the main beam and incur minimal loss, antenna pointing has to be more precise. Yet this is difficult to achieve for larger structures.

With an array configuration of smaller antennas, antenna-pointing error is not an issue. The difficulty is transferred from the mechanical to the electronic domain. The wider beamwidth associated with the smaller aperture of each array element makes the array more tolerant to pointing error. As long as the combining process is performed with minimal signal degradation, an optimal gain can be achieved.

Arraying also allows for an increase in effective aperture beyond the present 70-m capability for supporting a mission at a time of need. In the past, the Voyager Mission relied on arraying to increase its data return during Uranus and Neptune encounters in the late 1980s. The Galileo Mission provides a recent example in which arraying was used to increase the science data return by a factor of 3. (When combined with other improvements, such as a better

coding scheme, a more efficient data compression, and a reduction of system noise temperature, a total improvement of a factor of 10 was actually realized.)

Future missions also can benefit from arraying. These include the class of missions that, during certain operational phases, require more performance than a single antenna can offer. For example, the Cassini Mission requires only a single 34-m antenna during cruise phase, but upon entering the Saturn orbit, in order to return 4 Gbits/day mapping data, it will need an array of a 70-m and a 34-m antenna [4]. Missions that need to relay critical science data back to Earth in the shortest possible time also are potential beneficiaries. The Stardust Mission, for example, can reduce single-event risk by increasing the data rate for its encounter with the Wild 2 comet in 2004.

1.1.2 Operability Benefits

Arraying can increase system operability. First, higher resource utilization can be achieved. With a single-aperture configuration, a shortfall in the 34-m link performance will immediately require the use of the 70-m antenna, increasing the potential for over-subscription of the 70-m service. In the case of an array, however, the set can be partitioned into many subsets supporting different missions simultaneously, each tailored according to the link requirements. In so doing, resource utilization can be enhanced.

Secondly, arraying offers high system availability and maintenance flexibility. Suppose the array is built with 10 percent spare elements. The regular preventive maintenance can be done on a rotating basis while allowing the system to be fully functional at all times.

Thirdly, the cost of spare components would be smaller. Instead of having to supply the system with 100 percent spares in order to make it fully functional around the clock, the array offers an option of furnishing spares at a fractional level.

Equally important is the operational robustness against failures. With a single resource, failure tends to bring the system down. With an array, failure in an array element degrades system performance but does not result in a service shutdown.

1.1.3 Cost Benefits

A cost saving is realized from the fact that smaller antennas, because of their weight and size, are easier to build. The fabrication process can be automated to reduce the cost. Many commercial vendors can participate in the antenna construction business, and the market competition will bring the cost down further.

It is often approximated that the antenna construction cost is proportional to the antenna volume. The reception capability, however, is proportional to the antenna surface area. For example, halving the antenna aperture reduces the

construction cost of a single antenna by a factor of 8; however, four antennas would be needed to achieve an equivalent aperture. The net advantage is an approximate 50 percent cost saving. Note, however, that antenna construction is only a part of the overall life cycle cost for the entire system deployment and operations. To calculate the actual savings, one needs to account for the cost of the extra electronics required at multiple array elements and the cost related to the increase in system complexity. Reference [5] documents the most recent DSN effort in estimating such cost.

1.1.4 Flexibility Benefits

Arraying offers a programmatic flexibility because additional elements can be incrementally added to increase the total aperture at the time of mission need. This option allows for a spread in required funding and minimizes the need to have all the cost incurred at one time. The addition of new elements can be done with little impact to the existing facilities that support ongoing operations.

1.1.5 Science Benefits

An array with a large baseline can be exploited to support science applications that rely on interferometry, such as very long baseline interferometry (VLBI) and radio astronomy. With future development of the large array described in Chapter 10, the DSN implementation would be synergistic with the international Square Kilometer Array (SKA) effort. Such a system, if implemented in time, can serve as a test bed for demonstration of capability, albeit on a smaller scale.

References

[1] J. W. Layland, P. J. Napier, and A. R. Thompson, "A VLA Experiment—Planning for Voyager at Neptune," *The Telecommunications and Data Acquisition Progress Report 42-82, April–June 1985*, Jet Propulsion Laboratory, Pasadena, California, pp. 136–142, August 15, 1985. http://ipnpr.jpl.nasa.gov/progress_report/

[2] J. S. Ulvestad, "Phasing the Antennas of the Very Large Array for Reception of Telemetry from Voyager 2 at Neptune Encounter," *The Telecommunications and Data Acquisition Progress Report 42-94, April–June 1988*, Jet Propulsion Laboratory, Pasadena, California, pp. 257–273, August 15, 1988. http://ipnpr.jpl.nasa.gov/progress_report/

[3] T. T. Pham, A. P. Jongeling, and D. H., "Enhancing Telemetry and Navigation Performance with Full Spectrum Arraying," IEEE Aerospace Conference, Big Sky, Montana, March 2000.

[4] *Deep Space Network, Near Earth and Deep Space Mission Support Requirements*, JPL D-0787 (internal document), Jet Propulsion Laboratory, Pasadena, California, October 1996.

[5] G. M. Resch, T. A. Cwik, V. Jamnejad, R. T. Logan, R. B. Miller, and D. H. Rogstad, *Synthesis of a Large Communications Aperture Using Small Antenna*, JPL Publication 94-15, Jet Propulsion Laboratory, Pasadena, California, 1994.

Chapter 2
Background of Arraying in the Deep Space Network

The Jet Propulsion Laboratory (JPL) operates the Deep Space Network (DSN) for the National Aeronautics and Space Administration (NASA) in order to communicate with spacecraft that are sent out to explore the solar system. The distances over which this communication takes place are extraordinarily large by Earth-based standards, and the power available for transmitting from the spacecraft is very low (typically 20 W or less). As a result, the communications links are invariably operated with very low margin, and there is a premium placed on improving all aspects of the ground system (i.e., antennas, low-noise amplifiers, receivers, coding, etc.).

An early system analysis of both the ground and flight aspects of deep-space communications by Potter et al. [1] concluded that the optimum ground configuration should be centered around large (i.e., at that time, 64-meter-diameter-class) antennas rather than arraying smaller antennas to create the equivalent capture area. This analysis was based on the concept of a dedicated link between a single ground antenna, a spacecraft that was continuously monitored from rise to set, and the highest possible data rate that technology would allow when the spacecraft encountered a distant planet.

In the more than 30 years since the Potter et al. study, a number of assumptions have changed. First, it was realized that spacecraft have emergencies, and no matter how much collecting area an agency had on the ground, that agency always wanted more in an emergency. One alternative was to "borrow" aperture from other agencies, but this implied arraying capability. Second, during an encounter with a distant planet, the scientists always wanted the maximum possible data return. Since it was not always politically or economically feasible to put up new 64-m antennas, again the pressure grew to

borrow other apertures to increase the data return. This culminated in the concept of interagency arraying when the 27 antennas of the radio astronomy community's Very Large Array were borrowed during the Voyager 2 encounter with Neptune in the mid-1980s and arrayed with the 70-m and two 34-m antennas at the Goldstone Deep Space Communications Complex to provide a data return that was not considered possible when the mission was launched. Third, it was realized that, during the long cruise phase of an interplanetary mission, the communications requirements were rather modest and could easily be satisfied by a much smaller antenna than one of 64 or 70 m in diameter. In this way, the DSN developed the concept of a collection of 34-m antennas that could be individually targeted for the increasing number of missions being envisioned, but that could also be arrayed for "special" events.

A more recent study by Resch et al. [2] examined the cost and performance ratio of a single 70-m aperture versus an array of paraboloids with the diameter of the paraboloid as a parameter. They concluded there was no obvious cost saving with an array configuration, but it did offer scheduling flexibility not possible with a single aperture.

2.1 Early Development

During the late 1960s and 1970s, interest in arraying within the DSN grew slowly, and two very different approaches to the problem were developed. The first approach capitalized on the fact that most deep-space missions modulate the carrier signal from the spacecraft with a subcarrier and then modulate the subcarrier with data. Since typically about 20 percent of the power radiated by the spacecraft is in the carrier, this carrier can serve as a beacon. If two or more antennas on Earth can lock onto this beacon, then the radio frequency (RF) spectrum at each antenna can be heterodyned to a much lower intermediate frequency (IF) range, the difference in time of arrival (i.e., the delay) compensated, and the IF spectrum from each antenna added in phase.

The second approach to arraying developed synergistically with a program that was intended to pursue scientific investigations of geodesy, Earth rotation, and radio astronomy. This program involved the observation of natural radio sources whose spectrum was pure noise, and the array was a collection of antennas functioning as a compound interferometer. The intent of the scientific investigations was to use the radio interferometer, whose elements commonly were separated by nearly an Earth diameter, as a device to measure parameters like the baseline length, the position of radio sources, and small changes in the rotation rate of the Earth. The quantity measured was the difference in time of arrival of the signal at the various antennas. However, as equipment and techniques were perfected, it was realized that, if the measurements could be done with enough accuracy, then the delay could be compensated, either in real time or after the fact if the data were recorded, and the resulting outputs from

all elements of the compound interferometer added in phase (rather than multiplied, as in interferometry) to yield an enhanced signal.

In 1977, JPL launched two Voyager spacecraft ostensibly with the purpose of exploring Jupiter but with the option of continuing on into the far solar system to fly by the outer planets. In fact, when these spacecraft were launched, it was not clear how much data could be returned from distances greater than that of Jupiter, and this question motivated a more intense study of arraying.

Voyager 2 obtained a gravitational assist from Jupiter and went on to fly by Saturn, Uranus, and Neptune. Saturn is almost twice as far from the Sun as Jupiter, Uranus almost four times as far, and Neptune six times as far. If nothing had been done to improve the link, then we would have expected about one-quarter of the data from Saturn as compared to that received from Jupiter; Uranus would have provided only one-sixteenth; and Neptune a mere one-thirty-sixth.

The data rate at Saturn was improved by upgrading the DSN 64-m antennas to a diameter of 70 m and lowering their system noise temperatures. At Uranus, the 70-m antenna in Australia was arrayed with a 64-m antenna belonging to the Commonwealth Scientific and Industrial Research Organization (CSIRO) and located approximated 180 km distant from the DSN 70-m antenna. At Neptune, arraying was accomplished using the 70-m and two 34-m antennas at Goldstone together with the 27 antennas of the Very Large Array (each 25 m in diameter) located in the middle of New Mexico. All of these efforts were successful in improving the data-rate return from the Voyager Mission. An important result was that the improvement obtained was very close to what the engineers predicted based on theoretical studies of the techniques used.

2.2 Current Status of Development

In this section, we discuss the systems that are in use in the DSN. It covers three systems whose deployments span a period of 8 years, from 1996 to 2003. All three employ the full-spectrum arraying technique.

In 1996, the first full-spectrum arraying system was developed and deployed to support the Galileo Mission [3]. The signal processing is done in near-real time, with a latency of a few minutes. A specially designed front-end processing captures the appropriate signal spectrum that contains telemetry information from each antenna participating in the array. The data then are turned into data records and stored on commercial computing workstations. The follow-on functions of correlating and combining, as well as the demodulating and decoding of the combined signal, are all done in software. Since the correlation and combining are implemented in software, the array can be applied to configurations that span over large baselines, e.g., thousand of kilometers in the case of the Galileo Mission, using a standard Internet-type connection. A drawback, however, is the bandwidth constraint of this

connection. In order to meet a reasonable latency performance (i.e., a few minutes), this system tends to be more useful to missions of low data rates, which is the case with the Galileo Mission because of the limited equivalent isotropic radiative power (EIRP) from the spacecraft's low-gain antenna. The Galileo system as designed is constrained by a maximum data rate of 1 ksym/s. This ceiling is a result of three factors:

1) The technology and cost constraints associated with that particular implementation. The objective was to deliver a system within given cost and schedule constraints, as dictated by Galileo Mission events.
2) A design that is specifically created for the Galileo Mission but can be extended for multimission support. For example, only certain output data rates most likely used by Galileo are built, tested, and delivered to operations. The current capability works within performance specifications for a data rate up to 1 ksym/s; however, with small software modifications, it can be extended to about 10 ksym/s. This upper limit is due to a constraint set by the bus bandwidth used in the electronics of the system.
3) In post-combining processing, the demodulation and decoding functions being done in the software. A software decoder allows for implementation of a new design of concatenated (14,1/4) convolutional and variable-redundancy Reed–Solomon codes that can offer a much higher coding gain. The software receiver allows reprocessing of data gaps, thus increasing the return of usable data. The drawback, however, is that software processing is throughput limited, making the system less adaptable to a large set of high-data-rate missions.

In 2001, a second full-spectrum arraying system became operational at the Goldstone Complex. It is a follow-on to the Galileo system and is called the Full Spectrum Processing Array (FSPA) system. The correlation and combining functions are done in real time, using hardware of field programmable gate array (FPGA) technology. In addition, the post-processing functions of demodulation and decoding are accomplished by the standard hardware that supports multimissions, rather than special-built equipment as in the Galileo system. In so doing, the real-time array system at Goldstone can support data rates in the range of Msym/s, and it allows for up to six-antenna arraying within a DSN complex. Note that, due to the hardware nature of the processing and its larger bandwidth, this system is limited to arraying within a single DSN site. The capability to array between two DSN complexes is not supported. The array is capable of operating at X-band frequency (8.4 GHz), which is the most common frequency used for deep-space communications; however, because the arraying is actually done at IF frequency after the first RF/IF downconversion, the corresponding IF frequency for S-band (2.3-GHz) and Ka-band (32-GHz)

signals is also within the range of captured bandwidth. As a result, existing missions that operate at S-band and future missions using Ka-band also can be arrayed, if desired.

In 2003, a third array system, which is functionally equivalent to the FSPA system described above, will be ready for deployment at the two overseas DSN facilities: Madrid and Canberra. Since these sites have fewer antennas, the deployed system has been downscaled to support four-antenna arraying. In this system, the design is further consolidated with more advanced FPGA technology. Functions that previously were done on application-specific boards, such as digital downconversion, delay, phase rotation, correlation, and combining, now reside on one board of a common design. Differences in functionality are handled by the FPGA programming. With a more powerful processor from recent technology advances, more functions can be packed onto the board. As a result, the system becomes much more compact. While the old design requires four fully populated racks, the new system can fit in two racks.

2.3 Anticipated Applications with Current Capabilities

An anticipated near-term use of DSN arraying is support for the return of high-value science data for the Cassini Mission. This mission has a commitment to return 4 Gb of data per day during its orbital phase. A single 70-m antenna does not provide adequate margin to support this required data rate. However, an array of one 70-m and one 34-m antenna is sufficient. This configuration increases the data return by 25 percent relative to that of the 70-m antenna. The arraying is being planned over the Goldstone and Madrid Complexes. It occurs in late 2004 and continues periodically until 2008.

Arraying is also likely to be used during the asteroid encounter of the Deep Impact Mission. In July 2005, the Deep Impact spacecraft will be releasing an impactor into the nucleus of the comet Tempel 1. With the data collected from the impact, scientists will be able to better understand the chemical and physical property of comets. Since this is a single-event observation most critical to the mission and it is occurring in a potentially hazardous environment, it is desirable to return the data as quickly as possible. An array of the 70-m and several 34-m antennas will help to increase the data rate.

Aside from increasing the mission data return, the array also is used as a tool to provide the backup support to the 70-m antenna during critical periods or during long maintenance periods. The backup support, however, is limited, not a full replacement of the 70-m antenna functionality. The backup capability applies to downlink telemetry and radio metric functions, but not to uplink commanding. Also, at the overseas complexes, there are not sufficient 34-m antennas to provide the equivalent aperture of a 70-m antenna. In Madrid, with a new 34-m BWG antenna scheduled for completion in 2003, there will be three 34-m antennas available. They can make up 75 percent of the reception

capability of the 70-m antenna. In Canberra, the 34-m subnet consists of only two antennas; thus, about 50 percent of a 70-m antenna's capacity can be realized via array. Goldstone, on the other hand, has four 34-m antennas and thus can closely match the 70-m capability.

References

[1] P. D. Potter, W. D. Merrick, and A. C. Ludwig, *Large Antenna Apertures and Arrays for Deep Space Communications*, JPL Technical Report 32-848, Jet Propulsion Laboratory, Pasadena, California, November 1, 1965.

[2] G. M. Resch, T. A. Cwik, V. Jamnejad, R. T. Logan, R. B. Miller, and D. H. Rogstad, *Synthesis of a Large Communications Aperture Using Small Antennas*, JPL Publication 94-15, Jet Propulsion Laboratory, Pasadena, California, July 1, 1994.

[3] T. T. Pham, S. Shambayati, D. E. Hardi, and S. G. Finley, "Tracking the Galileo Spacecraft with the DSCC Galileo Telemetry Prototype," *The Telecommunications and Data Acquisition Progress Report 42-119, July–September 1994*, Jet Propulsion Laboratory, Pasadena, California, pp. 221–235, November 15, 1994. http://ipnpr.jpl.nasa.gov/progress_report/

Chapter 3
Arraying Concepts

The gain of an antenna divided by its system temperature, G/T, is one of the parameters that determine how much data can be sent over a communications link with a specified SNR. Our first goal in any study to understand arraying is to outline some of the practical aspects of arraying by treating the problem as adding individual G/T's. Next, we must recognize the bounds on performance achievable with current technology and attempt to parameterize both performance and cost in a way that can be related to antenna diameter. Then we must understand how the overall reliability and availability of an array are related to cost and how an array compares to a single aperture.

3.1 An Array as an Interferometer

Figure 3-1 shows two antennas located somewhere on the surface of a rotating Earth, viewing a distant radio source and forming a simple interferometer [1]. In vector notation, the difference in time of arrival, τ_g, of a radio wave from an infinitely distant source is simply

$$\tau_1 - \tau_2 = \tau_g = \frac{\mathbf{B} \bullet \mathbf{i}}{c} = \frac{B\sin(\theta)}{c} \qquad (3.1\text{-}1)$$

where B is the baseline vector extending from the intersection of axes on antenna number 1 to the intersection of axes on antenna number 2, i is a unit vector pointing to the radio source, and c is the speed of light (see Appendix A for how to determine the antenna intersection of axes). If the source is not at infinite distance, then the wave front is slightly curved and the vector expression is somewhat more complicated, but the process is essentially the same. We can write an expression for the difference in time of arrival in terms

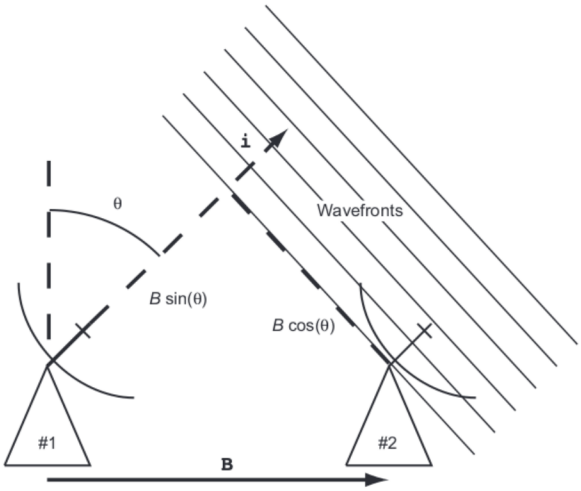

Fig. 3-1. A simple interferometer.

of the baseline and source directions. In effect, the accuracy with which we can calculate the delay is determined by the accuracy with which we can determine the baseline and source direction in a consistent reference frame.

Let us assume each antenna is observing a strong distant source at a radio frequency f, and the output of each antenna is connected to a multiplier by means of equal-length cables. The output of this multiplier, or correlator, at time t, then has the form

$$V_{\text{out}} \propto 2\sin(2\pi ft)\sin\left(2\pi f\left(t-\tau_g\right)\right) \tag{3.1-2}$$

If we expand this expression and run it through a low-pass filter, the result we are left with is

$$V_{\text{out}} \propto \cos\left(2\pi f\tau_g\right) \tag{3.1-3}$$

which is simply the coherent multiplication of the voltages from each element of the interferometer. Suppose the radio source being observed is a celestial source. Then τ_g will change by virtue of the Earth's rotation, and the output of the multiplier, or correlator, will exhibit the cosinusoidal variation described in Eq. (3.1-3) as the two signals go from in phase to out of phase.

If we know τ_g, or can somehow sense it, it is possible to build a compensating delay into one or both cables from the antennas such that the total cable delay and geometric delay is perfectly compensated. In this case, V_{out} for the multiplier is at maximum and the voltages are in phase. If we include an adding circuit in parallel with the multiplier, we can obtain the coherent sum of two antenna's voltages. It is just this kind of processing, using correlation to phase up the signals and then adding them, that constitutes a system that can perform antenna arraying.

For two identical antennas and receivers, this scheme for coherently adding the antenna signals doubles the SNR. However, it requires we implement a programmable delay line and calculate or derive, with some precision, the geometrical delay. The required precision of this delay is a function of the bandwidth of our receivers and can be determined as follows: Let us assume that our two antennas have identical receivers, centered at a frequency f_o, and have bandwidth Δf. If we make an error in the compensation of the geometric delay, we will in effect lose coherence, where the phase of the signal in the upper part of the band slips relative to the phase in the lower part. The requirement for coherence over the band becomes

$$\Delta f \, \Delta\tau \ll 1 \tag{3.1-4}$$

where Δf is in cycles and $\Delta\tau$ is in seconds. This requirement is simply stating that the phase shift across the bandpass due to an error in delay should be a small part of a cycle (less than or equal to 0.01 would work well). Therefore, for a bandwidth of 1 MHz, the error in delay compensation must be much less than a microsecond, or we will lose coherence in both the multiplication as well as the addition of the signals.

To see how errors in the length of the baseline (B) and errors in position of the source (θ, in radians) translate into errors in delay, we take the derivative of Eq. (3.1-1). Since these two errors are at right angles to each other, this derivative must take the form of a gradiant:

$$\nabla\tau_g = \Delta\tau_g = \left(\frac{\sin\theta}{c}\right)\Delta B\,\mathbf{u_B} + \left(\frac{B\cos\theta}{c}\right)\Delta\theta\,\mathbf{u_\theta} \tag{3.1-5}$$

where vectors are indicated by boldface, the unit vectors are along the direction of B, and the direction of θ is at right angles to B.

The error in the calculation of geometric delay is simply the modulus of Eq. (3.1-5), or

$$\Delta\tau_g = \sqrt{\left(\frac{\sin\theta}{c}\right)^2 \Delta B^2 + \left(\frac{B\cos\theta}{c}\right)^2 \Delta\theta^2} \tag{3.1-6}$$

As an example, if our bandwidth were 10 MHz and we wished to keep our delay errors to 10^{-2} of the coherence function, then the above expressions indicate that the baseline error should be kept below 1 ns or 30 cm. A similar bound could be placed on the source position error $\Delta\theta$.

3.2 Detectability

The detectability of the signals that are discussed here will always relate to a sensitivity factor, known as G/T, where G is typically the gain of the antenna used to gather energy from the signal of interest and T is the total system temperature. Putting aside for the moment the question of how to coherently add apertures, the maximum possible sensitivity factor for an ideal array (i.e., no combining losses) is simply the sum of the sensitivity factors for each element, or

$$\left[\frac{G}{T}\right]_{\text{array}} = \sum_{i=1}^{N}\left(\frac{G}{T}\right)_i \tag{3.2-1}$$

In the case of a homogeneous array, having elements of equal collecting area and system temperature, the sensitivity factor is

$$\left[\frac{G}{T}\right]_{\text{array}} = \left(\frac{G}{T}\right)_0 \sum_{i=1}^{N} 1 = N\left(\frac{G}{T}\right)_0 \tag{3.2-2}$$

where the quantity in square brackets divided by $(G/T)_0$ is called the array gain and is usually expressed in decibels (dB). Figure 3-2 illustrates this by plotting the array gain versus the number of elements in the array (assumed to have equal G/T). It can be seen that, as the number of array elements increases, the incremental improvement in performance decreases. For instance (again assuming no combining loss), going from a single antenna to two antennas doubles the SNR and results in a 3-dB gain. However, going from two to three antennas results in a 4.8-dB overall gain, or an increase of 1.8 dB over the two-element array, and adding a tenth element to a nine-element array increases the SNR by only 0.46 dB.

For an inhomogeneous array, i.e., one having elements with different G_i's and T_i's, the arithmetic is more complicated but the reasoning is the same and can be evaluated easily. In this case, array gain typically is computed by adding G/T to the most sensitive element. If you array two antennas, the first having a G/T that is ten times the second, then the array gain will be about 0.4 dB. The cost of adding the second array element can be quantified, but only the customer can decide if the 0.4 dB is worth the cost.

Given these considerations, it seems reasonable that, for the case of large, costly elements, we not consider any element for addition to an array unless it

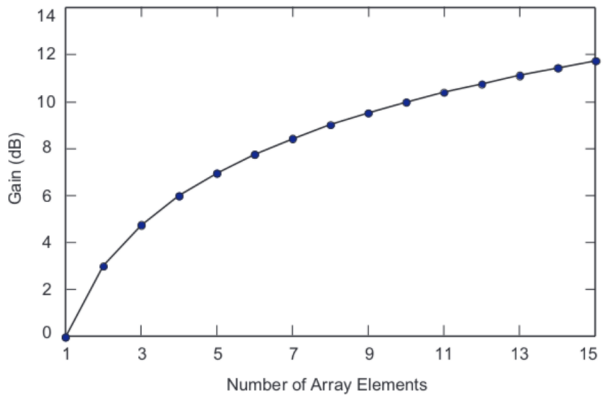

Fig. 3-2. Array gain as a function of the number of elements.

adds at least 10 percent to the aggregate G/T of the array. This suggests a rule of thumb that we not consider arrays larger than 10 elements. A particular example that might be of interest to the DSN is the arraying of, say, two 34-m elements with one 70-m element. If we assume all three have the same receiver temperature, then, since a 70-m antenna is about twice the diameter of a 34-m antenna, the G/T of the 70-m antenna is about four times that of the 34-m. Therefore, an additional 34 m will improve the G/T of an array of a 70-m antenna and a 34-m antenna by about one-fifth, or about 0.8 dB.

3.3 Gain Limits for an Antenna and Array

The gain, G, of an antenna is given in terms of its effective collecting area, A_e, at an operating wavelength, λ, as

$$G = \frac{4\pi}{\lambda^2} A_e \tag{3.3-1}$$

The effective collecting area, as well, can be written as the product of the physical aperture area, A_p, times a factor, η, that is termed the aperture efficiency.

Ruze [2] has pointed out that various mechanisms cause deviations in the reflector surface that result in a systematic or random phase error. These errors can be mapped into the aperture plane and lead to a net loss of gain such that the relative gain is given by the expression

$$\frac{G}{G_0} = \exp\left[-\left(\frac{4\pi\sigma}{\lambda}\right)^2\right] \tag{3.3-2}$$

where σ^2 is the variance of the phase error in the aperture plane. While Eq. (3.3-1) predicts that the gain of an antenna should increase as the square of the frequency, Eq. (3.3-2) predicts that when $(\sigma/\lambda) > 1$, the gain drops rapidly. If we use Eq. (3.3-1) as the G_0 in Eq. (3.3-2) and then set its derivative with respect to λ equal to zero, we calculate that the gain will be a maximum at a wavelength λ_{min}, which is approximately equal to 13 times the root-mean-square (rms) surface error σ. This point is known as the gain limit of the antenna. Note that the concept of gain limit is equally valid for a synthesized aperture.

The phase error in the aperture plane of a single antenna is composed of several components: the surface roughness of the reflector (σ), mechanical distortions from a designed, specified parabolic shape, and the propagation medium, which could include the radome of the antenna if it has one, the atmosphere, and the ionosphere. Clearly, there are distortions in the effective aperture plane of an array that result in phase errors that are analogous to those of a single aperture. While most of these errors will be reduced with calibration by the arraying algorithm, any residuals will lead to a loss of gain for the array.

One of the potential disadvantages of an array is due to the fact that its physical extent is always larger than the equivalent single-antenna aperture that it synthesizes. As a result, phase errors due to atmospheric fluctuations, which increase as the distance between individual elements increases, can limit the gain of the array. A typical example of this phenomenon is in the case of the troposphere, where over short distances (<1 km) the phase fluctuations are coherent because they come from the same atmospheric cell. Therefore, for antennas close together, the phase variations between the two antennas cancel each other out. As the distance between the antennas increases, the phase variations are coming from different atmospheric cells and are no longer coherent. Therefore, cancellation no longer takes place.

3.4 System Temperature

In characterizing the performance of antenna and receiver systems, it is common practice to specify the noise power of a receiving system in terms of the temperature of a matched resistive load that would produce an equal power level in an equivalent noise-free receiver. This temperature is usually called the "system temperature" and consists of two components: the temperature corresponding to the receiver itself due to internal noise in its front-end amplifier, and the temperature corresponding to antenna losses or spurious signals coming from ground radiation, atmospheric attenuation, cosmic background, and other sources. The term "antenna temperature" usually is used

to express the power received from an external radio source and is related to the intensity of the source as well as to the collecting area and efficiency of the antenna. In what follows, we will use this terminology to characterize various receiver systems that have been used in the DSN [3]. Clearly, any improvement that can be made in the area of system temperature on a specific antenna should be considered before taking the steps to array several such antennas.

There is a new generation of transistor amplifiers called high electron mobility transistors (HEMTs). Figure 3-3 illustrates the state of this technology in 1989. In this figure, the effective noise temperature of an 8.4-GHz (X-band) HEMT amplifier is plotted against the physical temperature of the device. It can be seen that the noise temperature of the amplifier varies almost linearly with the physical temperature. The data were fitted with a straight line (shown as the solid line) that indicates the amplifier noise improves at the rate of 0.44 kelvin per kelvin, or 0.44 K/K, in the region where the physical temperature is >150 K.

Figure 3-4 shows HEMT amplifier noise performance versus frequency for three common cooling configurations. The first is at room temperature, the second is cooled to approximately –50 deg C with a Peltier-effect cooler, and the third uses a closed-cycle helium refrigerator capable of lowering the device temperature to 15 K. Note that cooling has the most benefit at the higher frequencies. It is also important to remember that this technology has been highly dynamic for the past several years. As in most areas of microelectronics, there have been rapid improvements in performance, accompanied by reduced costs.

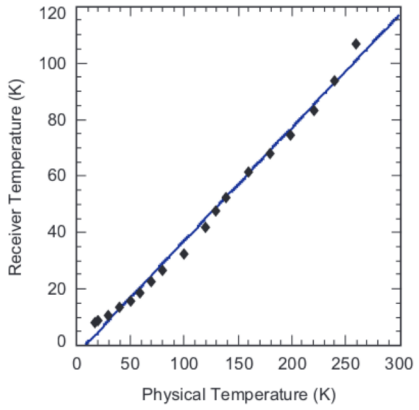

Fig. 3-3. Amplifier performance versus temperature.

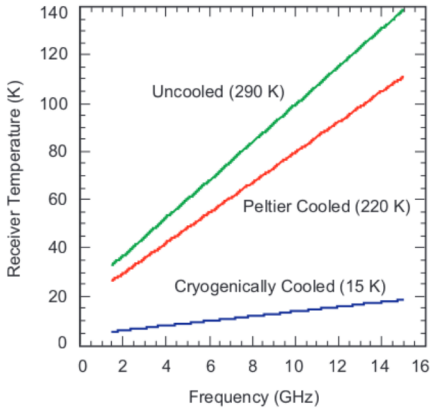

Fig. 3-4. Amplifier performance versus frequency.

Table 3-1 lists the various noise contributions to the total system temperature we might expect for a HEMT RF package at both 4 GHz (C-band) and 13 GHz (Ku-band). The atmospheric contribution comes from thermal noise generated by atmospheric gases and varies as the amount of atmosphere along the line of sight, i.e., as the secant of the zenith angle Z. The cosmic blackbody background is a constant 2.7 K. Spillover and scattering will depend on antenna [e.g., prime focus, Cassegrain, or beam waveguide (BWG)], feed, and support structure design.

3.5 Reliability and Availability

In the following discussion, we will compare results for communication links made up of arrays of various sizes. As we will see, there are certain advantages for availability that occur when using a large number of smaller elements verses a small number of large elements to achieve a given level of performance.

The specification of a communications link requires knowledge of the availability of the link components, one of which is the ground aperture, or array element. If we were to operate an array with no link margin (by margin, we mean extra capacity over what is necessary to meet requirements), we would find that increasing the array size beyond some number $N_{\max}$ leads to the interesting conclusion that the total data return is decreased!

Table 3-1. Range of total system temperature.

Noise Source	4.0 GHz	13.0 GHz
Atmosphere (K)	5.0 s(Z)	7.8 s(Z)
Cosmic background	2.7	2.7
Spillover, scattering	4–8	4–8
Microwave losses	4–12	4–16
Subtotal	16–28	19–31
Receiver temperature		
Room temperature (290 K)	40	110
Peltier (220 K)	30	90
Cryogenic (15 K)	8	17
Total (zenith)		
Room temperature (290 K)	56–68	129–141
Peltier (210 K)	46–58	109–121
Cryogenic (15 K)	24–36	36–48

In order to clarify this assertion, consider the following simplified argument. Define the availability, A_T, of a system to be the percentage of time that the system is operable for scheduled support. Thus, the down time required for maintenance is not counted. We should keep in mind that the overall availability is a product of all subsystem availabilities, although, for the remainder of this discussion, we will focus on the antenna availability. The total data return, D_T, can be written in terms of the system availability, A_T, and the integral of the data rate:

$$D_T = A_T \int D_R(t)dt \tag{3.5-1}$$

where the integral is taken over the interesting portion of the mission. Suppose the data rate, $D_R(t)$, is adjusted to the highest level that can be supported by the total ground aperture used to receive the signal. If we use an array on the ground of N elements, each having availability p, and the total signal from the array is near the detection threshold, then the total data return can be written in the form

$$D_T = Np^N f(t) \tag{3.5-2}$$

where $f(t)$ is some function of time and includes all of the factors that enter into link performance (e.g., distance, antenna gain, duration of a pass, etc.), and p^N is the availability of the entire array. Very often $f(t)$ cannot be increased, and the total data return can be increased only by increasing the ground array (e.g., a signal of interest transmits only for a finite duration and does not repeat). Since $p<1$, we see that D_T has a maximum value at the value of N given by

$$N_{\max} = \frac{-1}{\ln(p)} \tag{3.5-3}$$

A graph of $N_{\max}$ as a function of the individual array-element availability p is shown in Fig. 3-5. Using Eq. (3.5-2), we see for an array whose size is greater than $N_{\max}$ that the data return drops precipitously. This result stems directly from our assumption that the data rate would be increased to take advantage of *all* the ground aperture—that is how it is done with a single antenna. In fact, use of an array requires that we consider antenna availability in a different way than we do for a single antenna. In a link with a single antenna, the antenna is a single point of failure. In an array, the concept of availability must be merged with that of link margin.

In Appendix B, we derive relations that give the array availability as a function of the number of antenna elements (spare elements) over and above the minimum number needed to achieve the required G/T. In order to make a comparative assessment of the performance of various arrays, Fig. 3-6 shows the array availability plotted as a function of the fraction of extra elements that are devoted to sparing for three array sizes (designated in the figure by N_e for the number of required elements) and for a fixed-element availability of $p = 0.9$. The following interesting observation can be made: *The availability of*

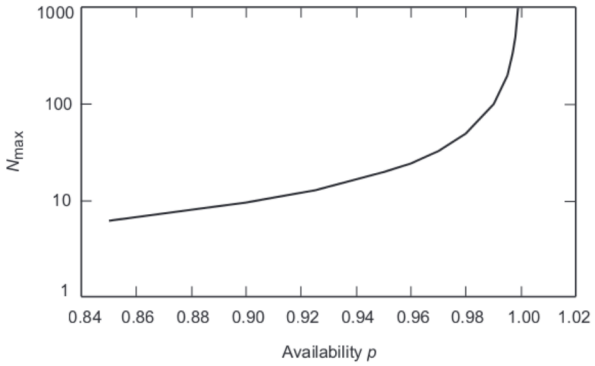

Fig. 3-5. $N_{\max}$ versus availability.

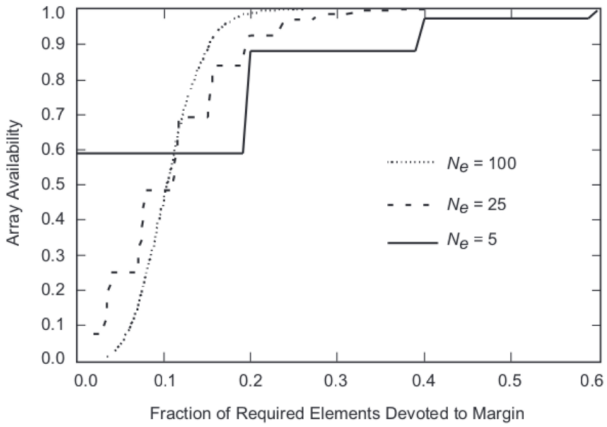

Fig. 3-6. Array availability versus element margin.

the array can be increased by increasing the number of spare elements. The array availability starts with a value much below the element availability, but increases rapidly and surpasses the element availability for a margin of less than about 30 percent, or 1 dB. The rate of increase of array availability is faster for arrays with a larger number of elements, even though it starts with a much smaller value. At some point as the sparing level increases, all the arrays with different numbers of elements reach approximately the same availability, beyond which a given sparing results in higher availability for larger arrays than for smaller arrays.

For larger arrays, sparing can be increased more gradually, since each additional element constitutes a smaller fraction of the total array. For an element availability of 0.9 for example, the minimum availability of a two-element array is 0.81, which increases to 0.972 by the addition of one element. This is the smallest increment possible and constitutes a 50 percent increase in the collecting area, or a 1.76-dB margin. In contrast, for a 10-element array with the same element availability, the minimum array availability is 0.349, but by the addition of three elements (a 30 percent increase, or a 1.1-dB margin), an array availability of 0.966 is achieved. Typically, for a given level of sparing or percentage of increase in the collecting aperture, a higher array availability is achieved in arrays with larger numbers of elements.

This discussion demonstrates some of the advantages of a large array of smaller apertures in comparison with a small array (few elements) of larger apertures, in terms of providing a more gradual way of increasing the performance margin or, conversely, a more gradual degradation in case of

element failure. Furthermore, since a higher array availability is achieved in arrays with larger numbers of elements (for a given margin or percentage of increase in the collecting aperture), the designer of a large array can trade off element reliability for cost, while still maintaining the same overall reliability as that of an array with a smaller number of elements with higher individual reliability. Interestingly enough, the smaller elements used in larger arrays typically have a much higher reliability than do their larger counterparts to begin with, since they are less complex and easier to maintain.

References

[1] A. R. Thompson, J. M. Moran, and G. W. Swenson, Jr., *Interferometry and Synthesis in Radio Astronomy*, New York: Wiley, 1986.

[2] J. Ruze, "Antenna Tolerance Theory—A Review," *Proceedings of the IEEE*, vol. 54, no. 4, pp. 633–640, April 1966.

[3] *DSMS Telecommunications Link Design Handbook*, JPL 810-5, D-10379, Rev. E., Jet Propulsion Laboratory, Pasadena, California, January 2001.

Chapter 4
Overview of Arraying Techniques

There are five basic signal-processing schemes that can be employed to combine the output of separate antennas that are observing a spacecraft-type signal. These schemes have come to be known as: (1) full-spectrum combining (FSC), (2) complex-symbol combining (CSC), (3) symbol-stream combining (SSC), (4) baseband combining (BC), and (5) carrier arraying (CA). Mileant et al. [1] have analyzed the performance of these techniques and have discussed the complexity of the reception of spacecraft signals. Their analysis will merely be summarized here but is presented in detail in Chapter 6. It should be noted that four of these schemes (CSC, SSC, BC, and CA) work *only* with a signal that has well-defined modulation characteristics. They utilize the fact that the signal source has a unique spectral characteristic and process those signals accordingly. The first scheme, FSC, works equally well with signals that are unknown or noise-like, as in the case of astronomical radio quasars.

All of the arraying techniques fall in the general category of signal processing. The overall SNR is determined by the capture area of the antennas and the thermal noise generated by the first amplifier. In a typical signal-flow diagram, the low-noise amplifier is followed by open-loop downconverters (typically two stages) that heterodyne the portion of the spectrum occupied by the spacecraft signal to a frequency that can be easily digitized. Digital signal-processing techniques are then employed, and ultimately an estimate is made of the data bits impressed on the carrier at the spacecraft. The data are then delivered to the project that operates the spacecraft. Although the front end of the signal-flow diagram is identical for all of the arraying techniques, and the ultimate goal is the same, the details of implementation vary. This results in very different capital investment and operations costs. These differences make it extremely difficult to unambiguously determine a "best" arraying technique. The following sections provide general characterizations of these techniques.

4.1 Full-Spectrum Combining (FSC)

The block diagram of FSC is shown in Fig. 4-1 and has been analyzed by Rogstad [2]. In FSC, the intermediate frequency (IF) signals from each antenna are transmitted to the combining site, where they are combined. To ensure coherence, the signals must be delayed and phase adjusted prior to combining. An estimate of the correct delay and phase normally is accomplished by correlating the signal streams.

The primary advantage of FSC is that it can utilize the spectral characteristics of the signal source but does not crucially depend on them, i.e., the received spectrum can be filtered if the spectral characteristics are known or accepted in total if the spectrum is unknown or noise-like. FSC can be used when the carrier is too weak to track or is not possible to track with a single antenna. In this case, the gross relative delays and phases between antennas are determined a priori from geometry calculations. Then the residual relative delays and phases are determined by cross-correlation of the signals from each antenna. These delays and phases are used to correct the antenna IF signals, and then they are combined.

One cost driver with FSC arises when the signal spectrum is unknown or noise-like. The entire signal bandwidth must then be transmitted to the combining site. If the transmission is analog, then the link must have high phase stability and low dispersion in order to maintain phase coherence at the radio frequency. If the link is digital, it must have relatively large bandwidth (assuming multibit digitization). Depending on the compactness of the array

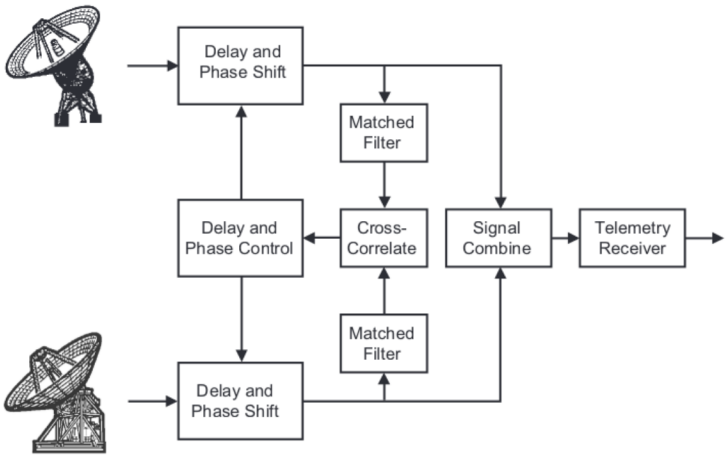

Fig. 4-1. Full-spectrum combining.

and the cost to install fiber-optic cabling, this may or may not be a real disadvantage.

4.2 Complex-Symbol Combining (CSC)

The block diagram of CSC is shown in Fig. 4-2. The intermediate frequency (IF) signal from each antenna is fed to a receiver, where it is open-loop carrier tracked using the best available carrier predicts. If this tracking is kept within a frequency error much less than the symbol rate, it can then be subcarrier demodulated (if used), and then symbol synchronization (sync) can be performed. These complex symbols (because of the unlocked carrier) are sent to the combining site, where they are combined. To ensure coherence, the signals must be phase adjusted prior to combining. An estimate of the correct phase normally is accomplished by correlating the various signal streams.

An advantage of this technique is that the data are transmitted to some central combining site at only slightly higher than the symbol rate. The symbol rate is some multiple of the data rate, dependent on the coding scheme, and for most applications is relatively modest. The rate at which data are communicated to a central site is an important cost consideration since most users want their data in real time. However, as with FSC, there are stringent requirements on instrumental phase stability.

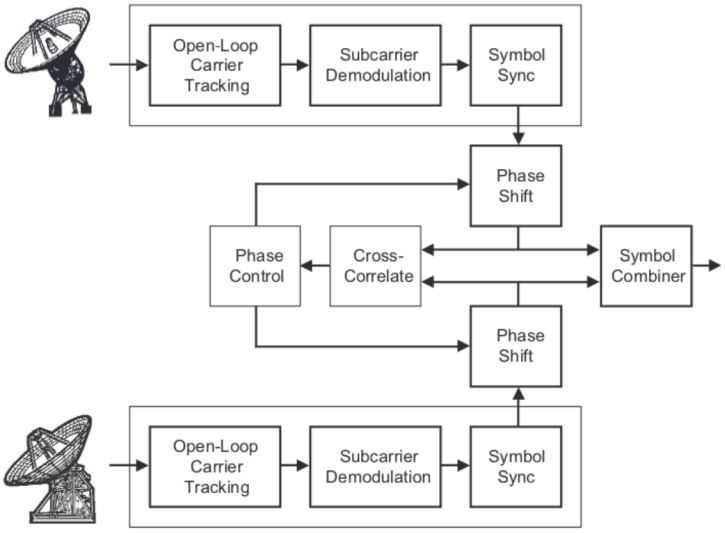

Fig. 4-2. Complex-symbol combining.

The disadvantages of CSC stem from the requirement that, like SSC, a carrier, subcarrier (if used), and symbol-tracking device must be provided for each antenna. The fact that the carrier-tracking loops are left open lessens the demand for an SNR as high as the one in the SSC case (see the next section).

4.3 Symbol-Stream Combining (SSC)

The block diagram of SSC is shown in Fig. 4-3. The signal from each antenna is used by the receiver to track the carrier (and subcarrier, if present) and to perform symbol synchronization. Once symbol synchronization is achieved, it is relatively straightforward to delay one data stream relative to the other in order to align the symbols in time. The symbols are then combined with the appropriate weights to form an estimate of a "soft" symbol, i.e., the raw telemetry data, before a decision is made as to whether a given bit (derived from the symbols through data decoding) is +1 or –1.

One advantage of this technique is that the data are transmitted to some central combining site at the symbol rate. The symbol rate is some multiple of the data rate, dependent on the coding scheme, and for most applications is relatively modest. The rate at which data are communicated to a central site is an important cost consideration since most users want their data in real time. In addition, there are no stringent requirements on instrumental phase stability.

The disadvantages of SSC stem from the requirement that a carrier, subcarrier (if used), and symbol-tracking device be provided for each antenna. Given that the cost per unit of complexity for digital electronics is rapidly decreasing with time, it may well be possible to build a "receiver on a chip" for just a few dollars, so the cost impact may be negligible. However, performance is another matter. The fact that all of the tracking loops must be locked demands that we have high loop SNR. This is achieved through a combination of high signal strength and small loop bandwidth. For small antennas with inherently low signal strength, the implied narrow loop bandwidth could become very difficult to obtain, and the technique could become impractical.

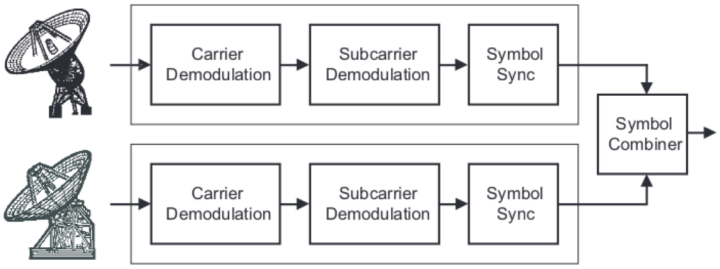

Fig. 4-3. Symbol-stream combining.

As a side note here, loop bandwidth can be thought of as inversely related to the amount of signal averaging that goes on within a phase-locked loop to obtain the error signal used to lock the loop. A narrow loop bandwidth means more averaging or integration in time, and therefore more SNR to lock. However, if the incoming signal is inherently unstable and varies significantly in frequency (phase noise), then the loop bandwidth must be kept large enough to maintain track. This trade-off determines the performance of the loop.

4.4 Baseband Combining (BC)

The block diagram of BC is shown in Fig. 4-4. In BC, the signal from each antenna is carrier locked. The output of the carrier loop is at a baseband frequency and consists of the subcarrier harmonics. The baseband signal is digitized, delayed, weighted, and then combined. The delay offsets usually are obtained by cross-correlating the baseband signals from the various antennas. The combined signal is used to achieve subcarrier lock and symbol demodulation. This technique collapses to SSC if no subcarrier is used.

In effect, the carrier signal from the spacecraft is used as a phase reference so that locking to the carrier eliminates the radio-frequency phase differences between antennas imposed by the propagation medium. The information bandwidth containing the subcarrier and its harmonics is relatively narrow and can be heterodyned to baseband. The low baseband frequency then imposes instrumental stability requirements that are relatively easy to compensate. The baseband data that must be transmitted to a central combining site contain all of the significant subcarrier harmonics and therefore can be more of a cost consideration than with SSC.

The disadvantage of this technique is that carrier lock is required on the signal from each individual antenna. As the antenna diameter decreases, the carrier SNR is reduced and must be compensated for either by a longer

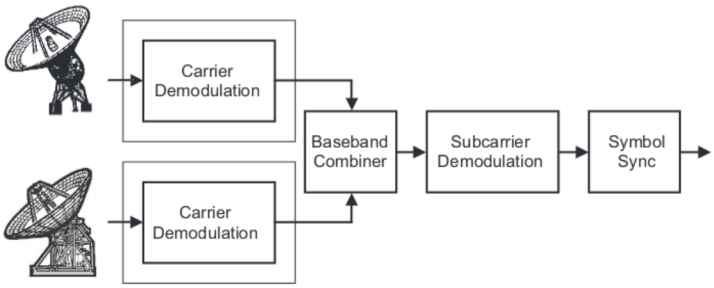

Fig. 4-4. Baseband combining.

integration time or by having the spacecraft increase the amount of power in the carrier. Halving the carrier SNR implies twice as much integration time (or, equivalently, a narrower bandwidth in the phase-locked tracking loop), which sometimes is possible but cannot be carried out indefinitely because of lack of signal stability due either to the transmitter, receiver, or propagation medium. If the spacecraft is programmed to increase the carrier power, there is less power available for the data, and the data rate must be reduced.

4.5 Carrier Arraying (CA)

The block diagram of CA is shown in Fig. 4-5. In carrier arraying, the individual carrier-tracking loops on each array element are "coupled" in order to enhance the received carrier SNR, thereby decreasing the "radio" loss due to an imperfect carrier lock on a single antenna [3].

In effect, all of the carrier-tracking devices are used to arrive at a "global" estimate of the best carrier synchronization. Alternatively, a single large antenna can provide carrier-lock information to a number of smaller antennas. The actual combining then can be done either at an intermediate frequency or at baseband, with the attendant advantages and disadvantages of each. However, carrier-lock information must be transmitted to a central site, and the global solution must be transmitted back to each antenna. For antennas separated by a large distance, the carrier-lock information must be corrected for different geometries. Estimates of the delay offsets normally are accomplished by correlating the signal streams from the various antennas.

Table 4-1 summarizes the requirements for each of the five types of arraying. Some of these are discussed in more detail in Chapter 6.

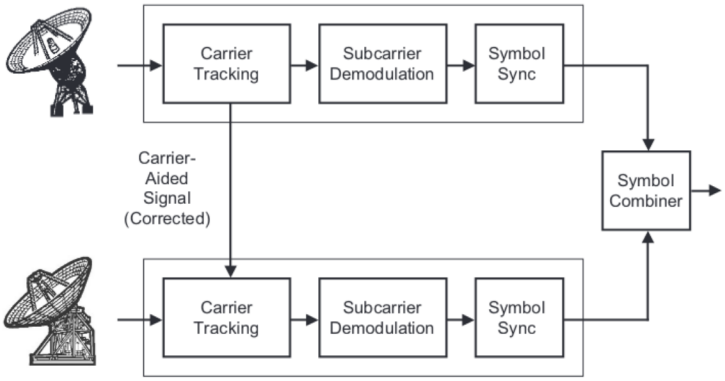

Fig. 4-5. Carrier arraying.

Table 4-1. Summary of requirements for combining techniques.

Requirements	FSC	CSC	SSC	BC	CA
Carrier lock at individual antennas	No	No	Yes	Yes	Yes
Bandwidth into combiner (in units of the symbol rate)	~10	~1	~1	~10	~1
Phase stability to antennas	High	High	Low	Low	High
Dependent on signal spectrum	No	Yes	Yes	Yes	Yes

References

[1] A. Mileant and S. Hinedi, "Overview of Arraying Techniques in the Deep Space Network," *The Telecommunications and Data Acquisition Progress Report 42-104, October–December 1990*, Jet Propulsion Laboratory, Pasadena, California, pp. 109–139, February 15, 1991.

http://ipnpr.jpl.nasa.gov/progress_report/

[2] D. H. Rogstad, "Suppressed Carrier Full-Spectrum Combining," *The Telecommunications and Data Acquisition Progress Report 42-107, July–September 1991*, Jet Propulsion Laboratory, Pasadena, California, pp. 12–20, November 15, 1991. http://ipnpr.jpl.nasa.gov/progress_report/

[3] S. A. Butman, L. J. Deutsch, R. G. Lipes, and R. L. Miller, "Sideband-Aided Receiver Arraying," *The Telecommunications and Data Acquisition Progress Report 42-67, November–December 1981*, Jet Propulsion Laboratory, Pasadena, California, pp. 39–53, February 15, 1982.

http://ipnpr.jpl.nasa.gov/progress_report/

Chapter 5
Single-Receiver Performance

In this chapter, the performance characteristics of a single receiver are derived in such a way that the parameters defining this performance can be carried over to an array, allowing comparison between the various arraying techniques.

5.1 Basic Equations

In deep-space communications, the downlink symbols first are modulated onto a square-wave subcarrier, and then the modulated subcarrier is modulated onto an RF carrier [1]. This allows transmission of a residual-carrier component whose frequency does not coincide with the data spectrum and, therefore, minimizes interference between the two. At the receiver, the deep-space signal is demodulated using a carrier-tracking loop, a subcarrier-tracking loop [2], and a symbol-synchronizer loop [3], as shown in Fig. 5-1. Depending on the modulation index, carrier tracking can be achieved by a phase-locked loop (PLL), Costas loop, or both [4]. The PLL or a combination of loops is used for modulation indices less than 90 deg, whereas a Costas loop is used when the modulation index is 90 deg. The received signal from a deep-space spacecraft can be modeled as

$$r(t) = s(t) + n(t)$$

where

$$\begin{aligned} s(t) &= \sqrt{2P}\sin\left[\omega_c t + \Delta d(t) Sqr\left(\omega_{sc} t + \theta_{sc}\right) + \theta_c\right] \\ &= \sqrt{2P_c}\sin\left(\omega_c t + \theta_c\right) + \sqrt{2P_d}\, d(t) Sqr\left(\omega_{sc} t + \theta_{sc}\right)\cos\left(\omega_c t + \theta_c\right) \end{aligned} \tag{5.1-1}$$

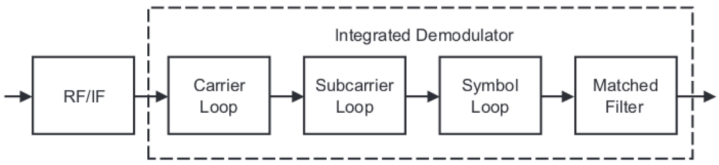

Fig. 5-1. A general coherent receiver model.

The carrier and data powers, denoted P_c and P_d, are given by $P\cos^2\Delta$ and $P\sin^2\Delta$, respectively, and P is the total received signal power, Δ is the modulation index, ω_c and θ_c are the carrier frequency and phase, $n(t)$ is an additive bandlimited white Gaussian noise process, $d(t)$ is the nonreturn-to-zero (NRZ) or Manchester data, and $Sqr(\ )$ designates the square-wave subcarrier with frequency ω_{sc} and phase θ_{sc}. Here the first component, the residual carrier, typically is tracked by a phase-locked loop, and the second component, the suppressed carrier, can be tracked by a Costas loop. The modulation $d(t)$ is given by

$$d(t) = \sum_{k=-\infty}^{\infty} d_k\, p(t - kT_s) \tag{5.1-2}$$

where d_k is the ±1 binary data, T_s is the symbol period, and $p(t)$ is a baseband pulse of unit power and limited to T_s seconds. The narrowband noise $n(t)$ can be written as

$$n(t) = \sqrt{2}n_c(t)\cos(\omega_c t + \theta_c) - \sqrt{2}n_s(t)\sin(\omega_c t + \theta_c) \tag{5.1-3}$$

where $n_c(t)$ and $n_s(t)$ are statistically independent, stationary, bandlimited white Gaussian noise processes with one-sided spectral density level N_0 (W/Hz) and one-sided bandwidth B (Hz), which is large compared to $1/T_s$.

The primary function of a receiver is to coherently detect the transmitted symbols as illustrated in Fig. 5-1. The demodulation process requires carrier, subcarrier, and symbol synchronization. The output of the receiver, v_k, is derived in Appendix C and given by

$$v_k = \sqrt{P_d}\, C_c\, C_{sc}\, C_{sy}\, d_k + n_k \tag{5.1-4}$$

where C_c, C_{sc}, and C_{sy} denote the carrier-, subcarrier-, and symbol-reduction functions and are given by

$$
\begin{aligned}
C_c &= \cos\phi_c \\
C_{sc} &= \left(1 - \frac{2}{\pi}|\phi_{sc}|\right) \\
C_{sy} &= \left(1 - \frac{1}{2\pi}|\phi_{sy}|\right)
\end{aligned}
\tag{5.1-5}
$$

and ϕ_c, ϕ_{sc}, and ϕ_{sy} denote carrier, subcarrier, and symbol phase errors, respectively, and n_k is a Gaussian random variable with variance $\sigma_n^2 = N_0/2T_s$. Symbol SNR degradation is defined as the average reduction in SNR at the symbol matched-filter output due to imperfect synchronization, whether carrier, subcarrier, or symbol. Ideally, $\phi_c = \phi_{sc} = \phi_{sy} = 0$, and Eq. (5.1-4) reduces to the ideal matched-filter output $v_k = \sqrt{P}d_k + n_k$, as expected. In deriving Eq. (5.1-4), it is assumed that the carrier, subcarrier, and symbol-loop bandwidths are much smaller than the symbol rate so that the phase errors ϕ_c, ϕ_{sc}, and ϕ_{sy} can be assumed to be constant over several symbols. Throughout this chapter, ϕ_c is assumed to be Tikhonov distributed [5]:

$$
p(\phi_c) = \frac{e^{\rho_c \cos\phi_c}}{2\pi I_0(\rho_c)}, \quad |\phi_c| \le \pi \tag{5.1-6}
$$

and ϕ_{sc} and ϕ_{sy} are assumed to be Gaussian distributed, i.e.,

$$
p(\phi_i) = \frac{e^{-\phi_i^2/2\sigma_i^2}}{\sqrt{2\pi\sigma_i^2}}, \qquad i = sc, sy \tag{5.1-7}
$$

where $\rho_i = 1/\sigma_i^2$ denotes the respective loop SNR and $p(\ )$ is a probability density function.

5.2 Degradation and Loss

A useful quantity needed to compute degradation and loss is the symbol SNR conditioned on ϕ_c, ϕ_{sc}, and ϕ_{sy}. The conditional symbol SNR, denoted SNR′, is defined as the square of the conditional mean computed with respect to the thermal noise of v_k divided by the conditional variance of v_k, i.e.,

$$
\text{SNR}' = \frac{\left[\overline{(v_k \mid \phi_c, \phi_{sc}, \phi_{sy})}\right]^2}{\sigma_n^2} = \frac{2P_d T_s}{N_0} C_c^2 C_{sc}^2 C_{sy}^2 \tag{5.2-1}
$$

where $\overline{(x \mid y)}$ denotes the statistical expectation of x conditioned on y, and v_k and σ_n^2 are as defined earlier.

The unconditional signal-to-noise ratio, denoted SNR, is found by averaging Eq. (5.2-1) over the carrier, subcarrier, and symbol phases. Letting $\bar{x}$ denote the average of x, the unconditional SNR is given as

$$\mathrm{SNR} = \frac{2P_d T_s}{N_0} \overline{C_c^2}\,\overline{C_{sc}^2}\,\overline{C_{sy}^2} \tag{5.2-2}$$

Ideally, when there are no phase errors (i.e., when $\phi_c = \phi_{sc} = \phi_{sy} = 0$), $C_c = C_{sc} = C_{sy} = 1$ and Eq. (5.2-2) reduces to $\mathrm{SNR}_{\mathrm{ideal}} = 2P_d T_s / N_0$, as expected. The symbol SNR degradation, D, is defined as the ratio of the unconditional SNR at the output of the matched filter in the presence of imperfect synchronization to the ideal matched-filter output SNR. The degradation, D, in dB for a single antenna thus is given by

$$D = 10\log_{10}\left[\frac{\mathrm{SNR}}{\mathrm{SNR}_{\mathrm{ideal}}}\right] = 10\log_{10}\left(\overline{C_c^2}\,\overline{C_{sc}^2}\,\overline{C_{sy}^2}\right) \tag{5.2-3}$$

Before proceeding, we need to understand and quantify the degradations due to the carrier, subcarrier, and symbol synchronization. Carrier tracking can be performed in two ways. The residual component of the signal can be tracked with a phase-locked loop or the suppressed component of the signal can be tracked with a Costas loop (see Sections 3.2 and 3.3 in [5]). With a PLL, the loop SNR is given by

$$\rho_{c,r} = \frac{1}{\sigma_{c,r}^2} = \frac{P_c}{N_0 B_c} \tag{5.2-4}$$

where B_c is the carrier-loop bandwidth and $\sigma_{c,r}^2$ is the phase jitter in the loop (the subscript "*c,r*" refers to the carrier residual component). On the other hand, with a Costas loop, we have

$$\rho_{c,s} = \frac{1}{\sigma_{c,s}^2} = \frac{P_d S_L}{N_0 B_c} \tag{5.2-5}$$

where S_L is the squaring loss given by $S_L^{-1} = 1 + \left(1 / \left[2E_s / N_0\right]\right)$, and $E_s / N_0 = P_d T_s / N_0$ is the symbol SNR (the subscript "*c,s*" refers to the carrier suppressed component). Note from Eq. (5.1-1) that, when $\Delta = 90$ deg, the residual component disappears, and the carrier is fully suppressed. On the other hand, when $\Delta = 0$ deg, the signal reduces to a pure sine wave. When Δ is not exactly 0 or 90 deg, both components of the carrier (residual and suppressed) can be tracked simultaneously, and the carrier phase estimates can be combined to provide an improved estimate. This is referred to as sideband aiding (SA),

and it results in an improved carrier-loop SNR given to a first-order approximation by

$$\rho_c = \rho_{c,r} + \rho_{c,s} \tag{5.2-6}$$

Whether sideband aiding is employed or not, the degradation due to imperfect carrier reference is given by $\overline{C_c^2}$.

The subcarrier-loop phase jitter, σ_{sc}^2, in a Costas loop is given by [4]

$$\sigma_{sc}^2 = \frac{1}{\rho_{sc}} = \left(\frac{\pi}{2}\right)^2 \frac{B_{sc} w_{sc}}{P_d / N_0}\left(1 + \frac{1}{2E_s / N_0}\right) \tag{5.2-7}$$

where w_{sc} denotes the subcarrier window. Similarly, the symbol-loop phase jitter, σ_{sy}^2, assuming a data-transition tracking loop (DTTL), is [5]

$$\sigma_{sy}^2 = \frac{1}{\rho_{sy}} = \frac{2\pi^2 B_{sy} w_{sy}}{\left(P_d / N_0\right) erf^2\left(\sqrt{E_s / N_0}\right)} \tag{5.2-8}$$

where w_{sy} is the symbol window and $erf(\cdot)$ denotes the error function. The probability density functions (pdfs) of ϕ_c and ϕ_{sy} can be assumed to be Gaussian or Tikhonov. Assigning a Tikhonov density for the carrier phase error and a Gaussian density for the other two, the first two moments of C_c, C_{sc}, and C_{sy} of Eq. (5.1-5) become, respectively,

$$\begin{aligned}
\overline{C_c} &= \overline{\cos\phi_c} = \frac{I_1(\rho_c)}{I_0(\rho_c)} \\
\overline{C_c^2} &= \overline{\cos^2\phi_c} = \frac{1}{2}\left[1 + \frac{I_2(\rho_c)}{I_0(\rho_c)}\right] \\
\overline{C_{sc}} &= 1 - \frac{2}{\pi}\overline{|\phi_{sc}|} = 1 - \left(\frac{2}{\pi}\right)^{3/2}\sigma_{sc} \\
\overline{C_{sc}^2} &= 1 - \frac{4}{\pi}\overline{|\phi_{sc}|} + \frac{4}{\pi^2}\overline{\phi_{sc}^2} = 1 - \sqrt{\frac{32}{\pi^3}}\sigma_{sc} + \left(\frac{2}{\pi}\right)^2\sigma_{sc}^2 \\
\overline{C_{sy}} &= 1 - \frac{1}{2\pi}\overline{|\phi_{sy}|} = 1 - \sqrt{\frac{1}{2\pi}}\frac{\sigma_{sy}}{\pi} \\
\overline{C_{sy}^2} &= 1 - \frac{1}{\pi}\overline{|\phi_{sy}|} + \frac{1}{4\pi^2}\overline{\phi_{sy}^2} = 1 - \sqrt{\frac{2}{\pi}}\frac{\sigma_{sy}}{\pi} + \frac{\sigma_{sy}^2}{4\pi^2}
\end{aligned} \tag{5.2-9}$$

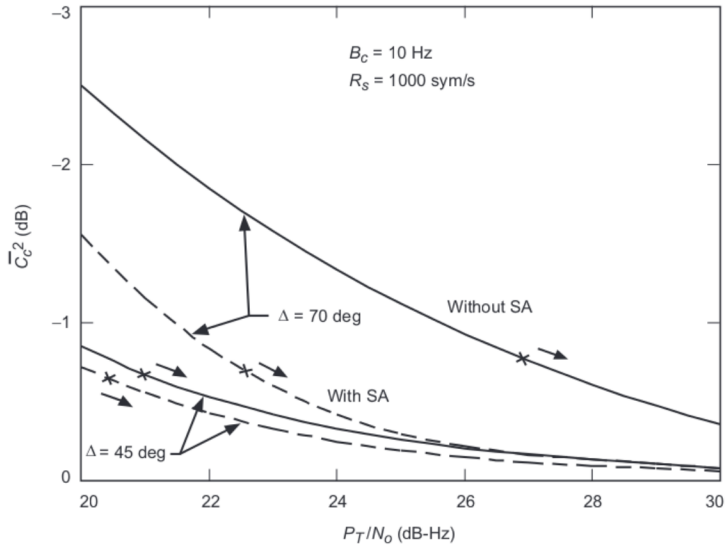

Fig. 5-2. Symbol SNR degradation due to imperfect carrier reference.

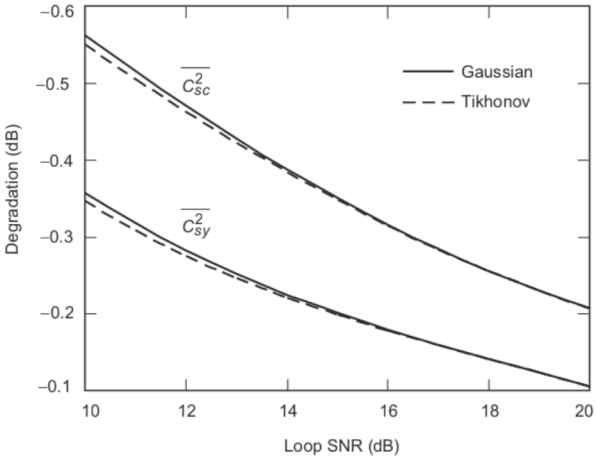

Fig. 5-3. Symbol SNR degradation in the presence of subcarrier and symbol phase jitter.

where $I_k(\cdot)$ denotes the modified Bessel function of order k and ρ_c is the carrier-loop SNR. The symbol degradations, $\overline{C_c^2}, \overline{C_{sc}^2}$, and $\overline{C_{sy}^2}$, versus the loop SNR are depicted in Figs. 5-2 and 5-3. Figure 5-3 also depicts the degradation, assuming ϕ_{sc} and ϕ_{sy} are either Gaussian or Tikhonov distributed. It is clear from this figure that both densities provide close results; therefore, the Gaussian assumption for the subcarrier and symbol phase errors will be utilized from here on.

The notion of loss is defined in terms of the desired bit- or symbol-error rate (SER). For the single receiver shown in Fig. 5-1, the symbol error rate, denoted $P_s(E)$, is defined as

$$P_s(E) = \iiint P_s\left(E \mid \frac{E_s}{N_0}, \phi_c, \phi_{sc}, \phi_{sy}\right) p_c(\phi_c) p_{sc}(\phi_{sc}) p_{sy}(\phi_{sy})\, d\phi_c d\phi_{sc} d\phi_{sy} \quad (5.2\text{-}10)$$

where $P_s\left(E \mid [E_s / N_0], \phi_c, \phi_{sc}, \phi_{sy}\right)$ is the symbol-error rate conditioned on the symbol SNR and on the phase errors in the tracking loops. For the uncoded channel,

$$P_s\left(E \mid \frac{E_s}{N_0}, \phi_c, \phi_{sc}, \phi_{sy}\right) = \frac{1}{2} erfc\left[\sqrt{\frac{E_s}{N_0} C_c^2 C_{sc}^2 C_{sy}^2}\right] \quad (5.2\text{-}11)$$

where $erfc(\cdot)$ is the complementary error function. Ideally, when there are no phase errors (i.e., when $\rho_c = \rho_{sc} = \rho_{sy} = \infty$, so that $C_c = C_{sc} = C_{sy} = 1$), Eq. (5.2-11) reduces to the well-known binary phase-shift keyed (BPSK) error rate,

$$P_s(E) = \frac{1}{2} erfc\left[\sqrt{\frac{E_S}{N_0}}\right] \quad (5.2\text{-}12)$$

Symbol SNR loss is defined as the additional symbol SNR needed in the presence of imperfect synchronization to achieve the same SER as in the presence of perfect synchronization. Mathematically, the SNR loss due to imperfect carrier-, subcarrier-, and symbol-timing references is given in dB as

$$L = 20\log_{10}\left[erfc^{-1}\left(2P_{s\ \text{ideal}}(E)\right)\right] - 20\log_{10}\left[erfc^{-1}\left(2P_{s\ \text{actual}}(E)\right)\right] \quad (5.2\text{-}13)$$

The first term in the above equation is the symbol SNR required for a given symbol-error rate in the presence of perfect synchronization, whereas the second term is the symbol SNR required with imperfect synchronization.

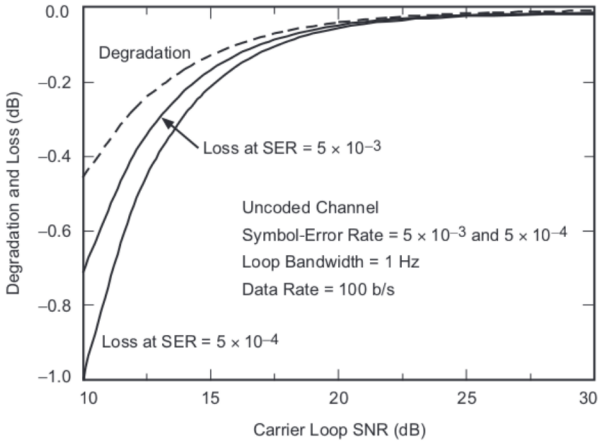

Fig. 5-4. Degradation and loss versus carrier-loop SNR.

Figure 5-4 depicts degradation and loss curves for the carrier loop. Note that loss is a function of $P_s(E)$, while degradation is not. Also, loss provides a more accurate performance prediction at the expense of added computational complexity and should be used when possible.

References

[1] M. M. Shihabi, T. Nguyen, and S. M. Hinedi, "A Comparison of Telemetry Signals in the Presence and Absence of Subcarrier," *IEEE Transactions on EMC*, vol. 76, no. 1, pp. 60–73, February 1994.

[2] W. J. Hurd and S. Aguirre, "A Method to Dramatically Improve Subcarrier Tracking," *The Telecommunications and Data Acquisition Progress Report 42-86, April–June 1986*, Jet Propulsion Laboratory, Pasadena, California, pp. 103–110, August 15, 1986. http://ipnpr.jpl.nasa.gov/progress_report/

[3] M. K. Simon, "Analysis of the Steady State Phase Noise Performance of a Digital Data-Transition Tracking Loop," *Space Programs Summary 37-55*, vol. 3, Jet Propulsion Laboratory, Pasadena, California, pp. 54–62, February 1969.

[4] R. Sfeir, S. Aguirre, and W. J. Hurd, "Coherent Digital Demodulation of a Residual Signal Using IF Sampling," *The Telecommunications and Data Acquisition Progress Report 42-78, April–June 1984*, Jet Propulsion Laboratory, Pasadena, California, pp. 135–142, August 15, 1984. http://ipnpr.jpl.nasa.gov/progress_report/

[5] J. Yuen, *Deep Space Telecommunications Systems Engineering*, New York: Plenum Press, 1983.

Chapter 6
Arraying Techniques

At least five different arraying schemes can be employed in designing an arraying system. In this discussion, they are referred to as full-spectrum combining (FSC), complex-symbol combining (CSC), symbol-stream combining (SSC), baseband combining (BC), and carrier arraying (CA). In addition, sideband aiding (SA) also can be employed, even though it is not strictly an arraying technique since it employs a single antenna (SA uses an estimate of the carrier phase derived from a Costas loop tracking the data sidebands to aid the carrier-tracking loop). In the next few sections, we will discuss how each of these schemes function and attempt to clarify their advantages and disadvantages. Furthermore, in Chapter 7, we will discuss combinations of these schemes, such as carrier arraying with sideband aiding and baseband combining (CA/SA/BC) or carrier arraying with symbol-stream combining (CA/SSC), to determine if such combinations provide any further advantage. The effective symbol SNR is derived for each arraying scheme, assuming L antennas and accounting for imperfect synchronization. In the cases where adjustments in both phase and delay are required to achieve synchronization, the delay component will be assumed as known. This is nominally true because the delay is largely determined by geometry and, therefore, can be accurately estimated. Also, since the signal bandwidths are narrow relative to their transmitted frequency, the delay accuracy is not as critical as is the phase. Complexity versus performance is traded off throughout the chapter, and benefits to the reception of existing spacecraft signals are discussed.

In what follows, the performances of different arraying schemes are compared on the basis of degradation only, since this parameter provides sufficient indication for relative comparison. For an exact performance

prediction, loss should be used in the region where loss and degradation do not agree.

6.1 Full-Spectrum Combining (FSC)

Full-spectrum combining is an arraying technique wherein the signals are combined at IF, as depicted in Figs. 6-1 and 6-2 [1]. One receiver chain—consisting of one carrier, one subcarrier, and one symbol-synchronization loop—then is used to demodulate the combined signal. The combining at IF is two-dimensional in the sense that both delay and phase alignment are required to coherently add the signals. Let the received signal at antenna 1 be denoted by $s_1(t)$. Then, from Eq. (5.1-1), we have

$$s_1(t) = \sqrt{2P_1}\sin\left[\omega_c t + \theta_1(t)\right] \tag{6.1-1}$$

where $\theta_1(t) = \theta_m(t) + \theta_c(t)$. The first term on the right-hand side is $\theta_m(t) = \Delta d(t) Sqr\left[\omega_{sc} t + \theta_{sc}\right]$ and represents the data modulation. The second term is $\theta_c(t) = \theta_d(t) + \theta_{osc}(t)$ and represents dynamics and phase noise, with $\theta_d(t)$ being the Doppler due to spacecraft motion and $\theta_{osc}(t)$ the oscillator phase noise. The received signals at the other antennas are delayed versions of $s_1(t)$ and are given by

$$s_i(t) = s(t-\tau_i) = \sqrt{2P_i}\sin\left[\omega_c(t-\tau_i) + \theta_i(t)\right] \tag{6.1-2}$$

for $i = 2,\ldots,L$, where τ_i denotes the delay in signal reception between the first and the ith antenna ($\tau_1 = 0$) and $\theta_i(t) = \theta_1(t-\tau_i) + \Delta\theta_i(t)$. Here, $\Delta\theta_i(t)$ accounts for differential Doppler and phase noises, which typically are "very small." Complex downconverting each $s_i(t)$ signal to IF, we obtain

$$\mathbf{x}_i(t) = \sqrt{P_i}\, e^{j\left[\omega_I t - \omega_c \tau_i + \theta_i(t)\right]} \tag{6.1-3}$$

where ω_I denotes the IF frequency. Delaying each $\mathbf{x}_i(t)$ signal by $-\tau_i$ (which is assumed to be known precisely), we have

$$\mathbf{y}_i(t) = \mathbf{x}_i(t+\tau_i) = \sqrt{P_i}\, e^{j\left[\omega_I t + (\omega_I - \omega_c)\tau_i + \theta_1(t) + \Delta\theta_i(t)\right]} \tag{6.1-4}$$

The signals $\mathbf{y}_i(t)$ cannot be added coherently because the phases are not aligned [due to the factor $(\omega_I - \omega_c)\tau_i$ and $\Delta\theta_i$], even though the data symbols are aligned [note that Doppler phase $\theta_d(t)$ is part of $\theta_1(t)$]. Therefore, an additional phase adjustment is necessary to add the signals coherently.

Let us consider an antenna interferometric pair as illustrated in Fig. 6-3. The signal at antenna i arrives τ_i seconds later than the signal at antenna 1,

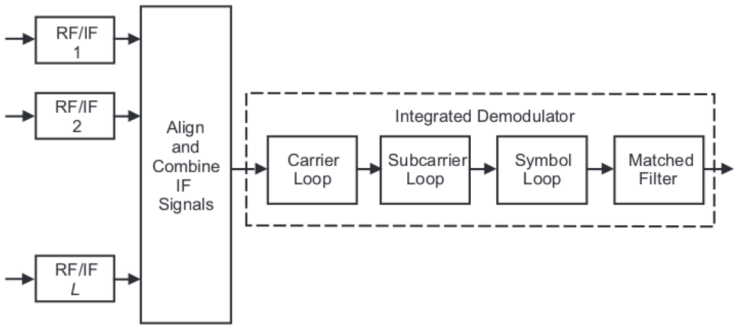

Fig. 6-1. Full-spectrum combining (FSC) for an *L*-antenna array.

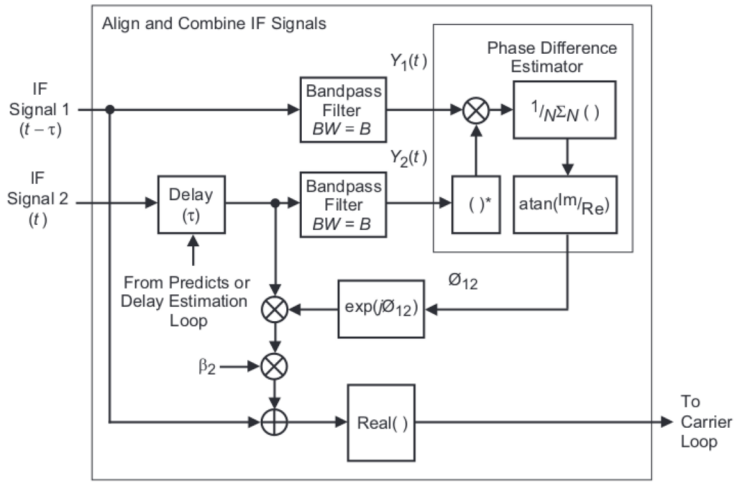

Fig. 6-2. FSC align and combine for a two-antenna array.

which will be used as a reference for mathematical convenience. After low-noise amplification, the signals are downconverted to IF, where the *i*th signal is delayed by $-\tau_i$ seconds. The latter delay consists of two components, a fixed component and a time-varying component. The fixed component compensates for unequal waveguide and cable lengths between the two antennas and the correlator. It is a known quantity that is determined by calibration. The time-

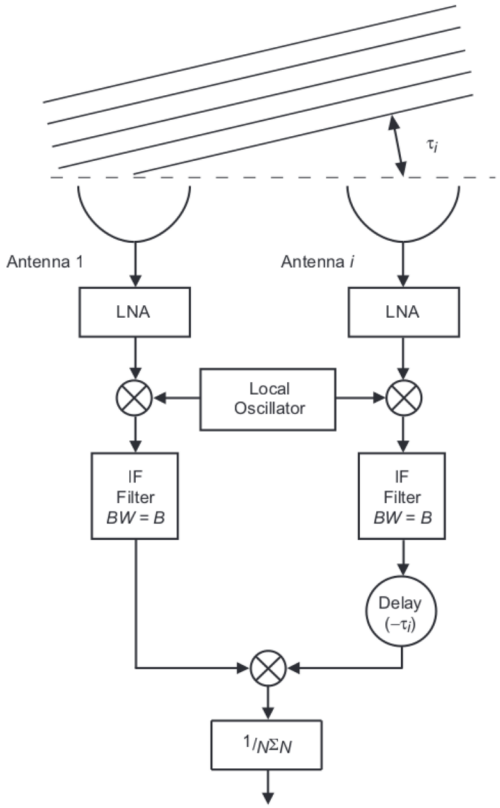

Fig. 6-3. An interferometric pair.

varying component compensates for unequal propagation lengths for the two received signals. This component typically is precomputed from the trajectory of the spacecraft and the physical location of the two antennas. The relative phase difference between the signals is estimated by performing a complex correlation on the resulting signals, which, for all practical purposes, have been aligned in time. At the input to the correlator, the two complex signals from the first and the ith antennas are passed through filters with bandwidth B Hz and subsequently sampled at the Nyquist rate of $2B$ samples per second. Mathematically, the complex sampled signals are given by

$$\mathbf{y}_1(t_k) = \sqrt{P_1}\, e^{j[\omega_I t_k + \theta_1(t_k)]} + \mathbf{n}_1(t_k)$$

and (6.1-5)

$$\mathbf{y}_i(t_k) = \sqrt{P_i}\, e^{j[\omega_I t_k + (\omega_I - \omega_c)\tau_i + \theta_i(t_k)]} + \mathbf{n}_i(t_k)$$

where $\mathbf{n}_1(t_k)$ and $\mathbf{n}_i(t_k)$ are independent complex Gaussian random variables with variances $\sigma_1^2 = N_{01}B$ and $\sigma_i^2 = N_{0i}B$. It will be shown later that the parameter B is essential in determining the averaging period and, thus, the combining loss. Correlating the signals (i.e., multiplying and low-pass filtering), we obtain

$$\mathbf{z}'_{i1}(t_k) = \sqrt{P_1 P_i}\, e^{j[\phi_{i1}(t_k)]} + \mathbf{n}_{i1}(t_k) \tag{6.1-6}$$

where $\phi_{i1} = (\omega_I - \omega_c)\tau_i + \Delta\theta_i(t_k)$ denotes the total phase difference between the signals, and $\mathbf{n}_{i1}$, the effective noise, is given by

$$\begin{aligned}\mathbf{n}_{i1} = {} & \sqrt{P_i}\, e^{j[\omega_I t_k + (\omega_I - \omega_c)\tau_i + \theta_i(t_k)]}\, \mathbf{n}_1(t_k) \\ & + \sqrt{P_1}\, e^{-j[\omega_I t_k + \theta_1(t_k)]}\, \mathbf{n}_i(t_k) + \mathbf{n}_1(t_k)\mathbf{n}_i(t_k)\end{aligned} \tag{6.1-7}$$

with effective variance

$$\sigma^2_{z'i} = \sigma_1^2 P_i + \sigma_i^2 P_1 + \sigma_1^2\sigma_i^2 = B(N_{01}P_i + N_{0i}P_1 + N_{01}N_{0i}B) \tag{6.1-8}$$

Following the correlation, an averaging operation over T seconds is performed to reduce the noise effect. In that period, N=2BT independent samples are used to reduce the variance of Eq. (6.1-8) by a factor of N. The SNR of $\mathbf{z}_{i1} = (1/N)\sum_{k=1}^{N} \mathbf{z}'_{i1}(t_k)$ at the output of the accumulator, SNR_{i1}, thus is given by

$$\mathrm{SNR}_{i1} = \frac{\mathrm{E}(\mathbf{z}_{i1})\mathrm{E}(\mathbf{z}_{i1}^*)}{Var(\mathbf{z}_{i1})} = \frac{N P_1 P_i}{\sigma^2_{zi}} = \frac{P_1}{N_{01}} \frac{2T}{[1 + (1/\gamma_i) + (B N_{0i}/P_i)]} \tag{6.1-9}$$

where γ_i is given by

$$\gamma_i = \frac{P_i}{P_1}\frac{N_{01}}{N_{0i}}\,, \qquad \sum_{i=1}^{L} \gamma_i = \Gamma \tag{6.1-10}$$

and is a function of the receiving antenna only. Appendix D provides these factors for the various DSN antennas at both 2.3 GHz (S-band) and X-band. (Note that, in radio metric applications [2], the SNR is defined as the ratio of

the standard deviation of the signal to that of the noise and is the square root of the SNR defined in the above equation.) When the correlation bandwidth B is very large (in the MHz range), the signal × noise term $(P_1\sigma_i^2 + P_i\sigma_1^2)$ can be ignored, and the effective noise variance is dominated by the noise × noise term $(\sigma_1^2\sigma_i^2)$, i.e.,

$$\sigma_{\mathbf{z}i}^2 \approx \sigma_1^2\sigma_i^2 \tag{6.1-11}$$

In this case, the SNR can be approximated by

$$\mathrm{SNR}_{i1} \approx \frac{P_1}{N_{01}}\frac{P_i}{N_{0i}}\frac{2T}{B} \tag{6.1-12}$$

An estimate of $\phi_{i1}, \hat{\phi}_{i1}$ is obtained by computing the inverse tangent of the real and imaginary parts of $\mathbf{z}_{i1}$, i.e.,

$$\hat{\phi}_{i1} = \tan^{-1}\left[\frac{\mathrm{Imag}[\mathbf{z}_{i1}]}{\mathrm{Real}[\mathbf{z}_{i1}]}\right] \tag{6.1-13}$$

The probability density function of the phase estimate is given in [2] as

$$p(\hat{\phi}_{i1}) = \frac{1}{2\pi}e^{-\mathrm{SNR}_{i1}/2}\left[1 + G\,e^{G^2}\sqrt{\pi}\,(1 + erf(G))\right] \tag{6.1-14}$$

where

$$G = \sqrt{\frac{\mathrm{SNR}_{i1}}{2}}\cos(\hat{\phi}_{i1} - \phi_{i1}) \tag{6.1-15}$$

The density in Eq. (6.1-14) is plotted in Fig. 6-4, and its derivation assumes that the noise $\mathbf{n}_{i1}$ is Gaussian (even though it is not Gaussian in the strict sense, a Gaussian approximation still is justified by invoking the central limit theorem due to the averaging over N samples). Figure 6-4 clearly indicates that a reasonably good phase estimate can be obtained for SNR_{i1} as low as 6 dB. At a moderately high SNR_{i1}, the distribution can be approximated by a Gaussian distribution with variance

$$\sigma_{\hat{\phi}_{i1}}^2 = \frac{1}{\mathrm{SNR}_{i1}} \tag{6.1-16}$$

In the simplest form of FSC, the signal from antenna 1 is correlated with all other signals and the phase errors estimated. An improvement in phase-error

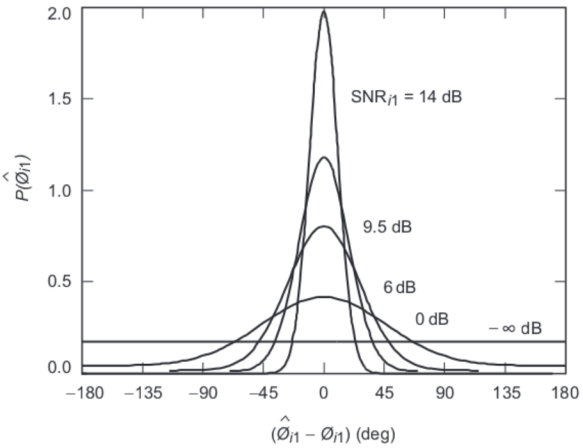

Fig. 6-4. The probability distribution of measured phase as a function of $(\hat{\phi}_{i1} - \phi_{i1})$ for a number of SNRs.

estimation can be obtained by performing global phasing between L antennas, which involves $L(L-1)/2$ complex correlations as the signal from each antenna is correlated with the signal from every other antenna [2]. In addition, closed-loop techniques can be utilized to reduce the phase error, as illustrated in Appendix E.

6.1.1 Telemetry Performance

In order to compute the degradation due to FSC, consider the IF signals after phase compensation, i.e.,

$$\mathbf{y}_i(t_k) = \sqrt{P_i}\, e^{j[\omega_I t_k + \theta_1(t_k) + \Delta\phi_{i1}(t_k)]} + \mathbf{n}_i(t_k) e^{j[\omega_I t_k + \theta_1(t_k) + \hat{\phi}_{i1}(t_k)]} \qquad (6.1\text{-}17)$$

where $\Delta\phi_{i1} = \hat{\phi}_{i1} - \phi_{i1}$ refers to the residual phase error between antenna 1 and the ith signal, and $\mathbf{n}_i(t_k)$ is the complex envelope of the thermal noise with two-sided noise spectral density N_{0i}. The signal combiner performs the weighted sum of $\mathbf{y}_i(t_k)$, namely

$$\begin{aligned} \mathbf{y}(t_k) &= \sum_{i=1}^{L} \beta_i \mathbf{y}_i(t_k) \\ &= \sum_{i=1}^{L} \beta_i \left[\sqrt{P_i}\, e^{j[\omega_I t_k + \theta_1(t_k) + \Delta\phi_{i1}(t_k)]} + \mathbf{n}_i(t_k) e^{j[\omega_I t_k + \theta_1(t_k) + \hat{\phi}_{i1}(t_k)]} \right] \end{aligned} \qquad (6.1\text{-}18)$$

Letting $\beta_1 = 1$ and optimizing $\beta_i, i = 2,..., L$, in order to maximize SNR′, we obtain

$$\beta_i = \sqrt{\frac{P_i}{P_1}} \frac{N_{01}}{N_{0i}} \tag{6.1-19}$$

Note that the variance of the combined complex signal $\mathbf{y}(t_k)$ is

$$\sigma_{\mathbf{y}}^2 = B \sum_{i=1}^{L} \beta_i^2 N_{0i} \tag{6.1-20}$$

The total signal power at the output of the combiner conditioned on residual phases, $\Delta\phi_{i1}(t_k)$, thus is given by

$$\begin{aligned} P'_{\mathbf{y}} &= \left[\overline{\left(\mathbf{y}(t_k) \mid \Delta\phi_{i1}(t_k) \right)} \right]^2 \\ &= \sum_{i=1}^{L} \sum_{j=1}^{L} \beta_i \beta_j \sqrt{P_i P_j}\, \mathbf{C}_{IF_i} \mathbf{C}^*_{IF_j} \\ &= \sum_{i=1}^{L} \beta_i^2 P_i + \sum_{i=1}^{L} \sum_{\substack{j=1 \\ i \neq j}}^{L} \beta_i \beta_j \sqrt{P_i P_j}\, \mathbf{C}_{IF_i} \mathbf{C}^*_{IF_j} \end{aligned} \tag{6.1-21}$$

where

$$\mathbf{C}_{IF_i} = e^{j\Delta\phi_{i1}(t_k)} \tag{6.1-22}$$

is the complex signal-reduction function due to phase misalignment between the ith and first signals. Assuming that the ensemble average of the phase difference between any two antennas is independent of which antenna pair is chosen and that the residual phase of each antenna pair is Gaussian distributed with variance $\sigma^2_{\Delta\phi_{i1}}$, then it can be shown that

$$\begin{aligned} \overline{\mathbf{C}_{IFi} \mathbf{C}^*_{IFj}} = C_{ij} &= \mathbf{E}\left\{ e^{j[\Delta\phi_{i1}(t_k) - \Delta\phi_{j1}(t_k)]} \right\} \\ &= \begin{cases} \{ e^{-(1/2)[\sigma^2_{\Delta\phi_{i1}} + \sigma^2_{\Delta\phi_{j1}}]}, & i \neq j, \sigma^2_{\Delta\phi_{11}} \equiv 0 \\ 1 & i = j \end{cases} \end{aligned} \tag{6.1-23}$$

Performing the above averaging operation over $P'_{\mathbf{y}}$, the total signal power is obtained, namely,

$$P_{\mathbf{y}} = P_1\left(\sum_{i=1}^{L}\gamma_i^2 + \sum_{i=1}^{L}\sum_{\substack{j=1\\ i\neq j}}^{L}\gamma_i\gamma_j C_{ij}\right) \tag{6.1-24}$$

Note that in an ideal scenario (i.e., no degradation) with L identical antennas, the signal-reduction functions approach 1 ($C_{ij}=1$ for all i,j) and Eq. (6.1-24) reduces to $P_{\mathbf{y}} = P_1 L^2$. Simultaneously, the noise variance of Eq. (6.1-20) becomes proportional to L and, hence, the SNR increases linearly with L, as expected.

With FSC, only one carrier, one subcarrier, and one symbol-tracking loop are required. The samples of the signal at the output of the integrate-and-dump filter can be expressed as

$$\begin{aligned} v_k &= d_k\sqrt{P_d}C_c C_{sc} C_{sy} + n_k' \\ \sigma_{n'}^2 &= \frac{1}{2T_s}\sum_{i=1}^{L}\beta_i^2 N_{0i} \end{aligned} \tag{6.1-25}$$

where P_d is the combined data power given by $P_{\mathbf{y}}\sin^2\Delta$ and n_k' is Gaussian with variance given by Eq. (6.1-25).

It can be shown that the symbol SNR in terms of $P_{d1} = P_1\sin^2\Delta$ is given by

$$\mathrm{SNR}_{fsc} = \frac{2P_{d1}T_s}{N_{01}}\overline{C_c^2}\,\overline{C_{sc}^2}\,\overline{C_{sy}^2}\left(\frac{\sum_{i=1}^{L}\gamma_i^2 + \sum_{i,j}\sum_{i\neq j}\gamma_i\gamma_j\overline{C}_{ij}}{\Gamma}\right) \tag{6.1-26}$$

where the loop losses are computed using the combined power, whether coming from the carrier or the data. Note that in the ideal case Eq. (6.1-26) reduces to $\mathrm{SNR}_{\mathrm{ideal}} = 2P_{d1}T_s\Gamma/N_{01}$, as expected. The degradation factor for FSC, D_{fsc}, is given as before [Eq. (5.2-3)] by the ratio (in decibels) of the combined symbol SNR to the ideal symbol SNR, i.e.,

$$\begin{aligned} D_{fsc} &= 10\log_{10}\left(\frac{\mathrm{SNR}_{fsc}}{\mathrm{SNR}_{\mathrm{ideal}}}\right) \\ &= 10\log_{10}\left(\overline{C_c^2}\,\overline{C_{sc}^2}\,\overline{C_{sy}^2}\left(\frac{\sum_{i=1}^{L}\gamma_i^2 + \sum_{i,j}\sum_{i\neq j}\gamma_i\gamma_j\overline{C}_{ij}}{\Gamma^2}\right)\right) \end{aligned} \tag{6.1-27}$$

As an example, let $P_i = P_1$, $N_{0i} = N_{01}$, and $\beta_i = 1$ for all antennas; then the signal and noise powers of the real process at the output of the combiner become, respectively,

$$\begin{aligned} P_y &= P_1\left[L + 2(L-1)e^{-\sigma_{\Delta\phi}^2/2} + (L-2)(L-1)e^{-\sigma_{\Delta\phi}^2}\right] \\ \sigma_y^2 &= B N_{01} L \end{aligned} \tag{6.1-28}$$

and the SNR at the combiner output becomes

$$\mathrm{SNR}_{fsc} = \frac{P_y}{\sigma_y^2} = \frac{P_1\left[L + 2(L-1)e^{-\sigma_{\Delta\phi}^2/2} + (L-2)(L-1)e^{-\sigma_{\Delta\phi}^2}\right]}{B N_{01} L} \tag{6.1-29}$$

With perfect alignment (i.e., $\sigma_{\Delta\phi}^2 \to 0$), the SNR_z reduces to

$$\mathrm{SNR}_{\mathrm{ideal}} = \frac{P_1 L}{N_{01} B} \tag{6.1-30}$$

as expected and, hence, the combining degradation for the FSC scheme is given by

$$D_{fsc} = 10\log_{10}\left[\frac{L + 2(L-1)e^{-\sigma_{\Delta\phi}^2/2} + (L-2)(L-1)e^{-\sigma_{\Delta\phi}^2}}{L^2}\right] \tag{6.1-31}$$

Note that D_{fsc} ideally approaches zero. For the case of a single antenna (i.e., no arraying), D_{fsc} measures the degradation due to imperfect synchronization. Figures 6-5 and 6-6 depict the degradation of FSC, D_{fsc}, for the array of two high-efficiency (HEF) antennas and one standard (STD) 34-m antenna as a function of P/N_0 of the master antenna (Fig. 6-5) and of modulation index Δ (Fig. 6-6). Also depicted is the degradation due to any single synchronization step (such as carrier, subcarrier, or symbol synchronization), obtained by setting the degradation due to the other steps to zero. An "x" has been placed in the figure to indicate the point at which carrier-loop SNR dips below 8 dB and significant cycle slipping occurs. Because with FSC the carrier loop tracks the combined signal, there is less degradation than when several carrier loops track individual signals, as in the case of symbol-stream combining or baseband combining (discussed in Sections 6.3 and 6.4).

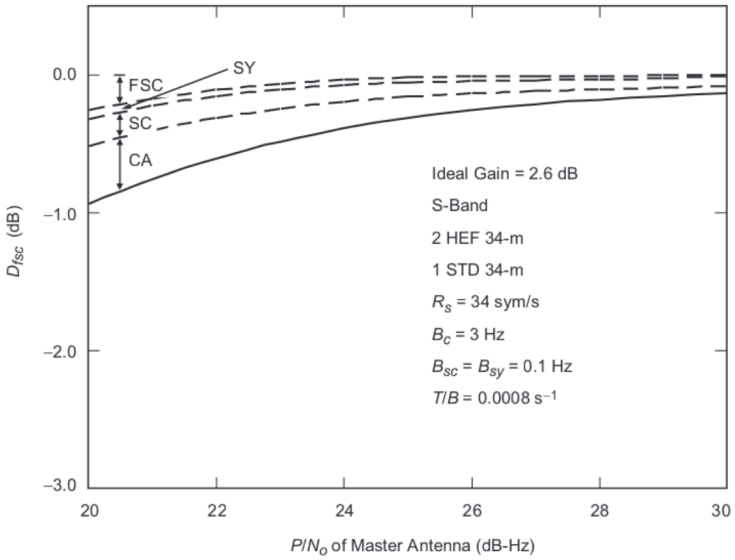

Fig. 6-5. The D_{fsc} versus P_1/N_{01} for a modulation index of 65.9 deg.

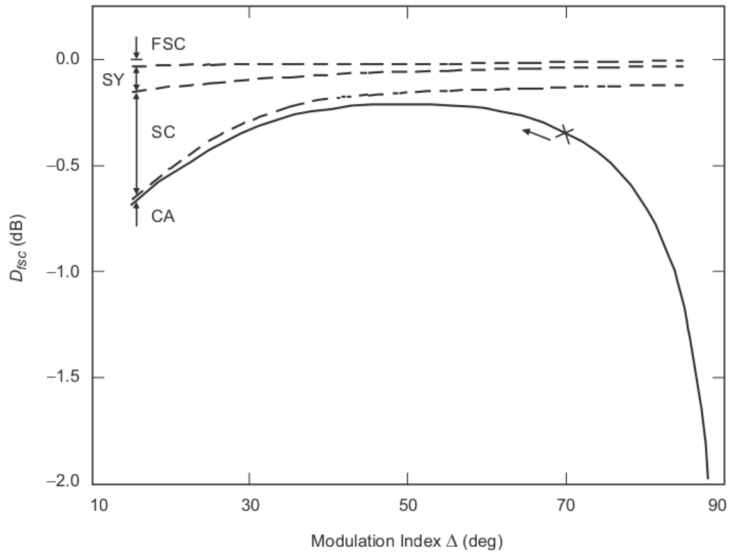

Fig. 6-6. The D_{fsc} versus modulation index for P_1/N_{01} = 25 dB-Hz.

6.2 Complex-Symbol Combining (CSC)

As depicted in Figs. 6-7 and 6-8, signals from multiple antennas in CSC are open-loop downconverted to baseband; partially demodulated using multiple subcarrier loops, multiple symbol loops, and multiple matched filters; and then combined and demodulated using a single baseband carrier loop. The advantage of CSC is that the symbol-combining loss is negligible and is performed in the data-rate bandwidth. Moreover, antennas that are continents apart can transmit their symbols in real or nonreal time to a central location, where the symbol-stream combiner outputs the final symbols. That, however, requires that each

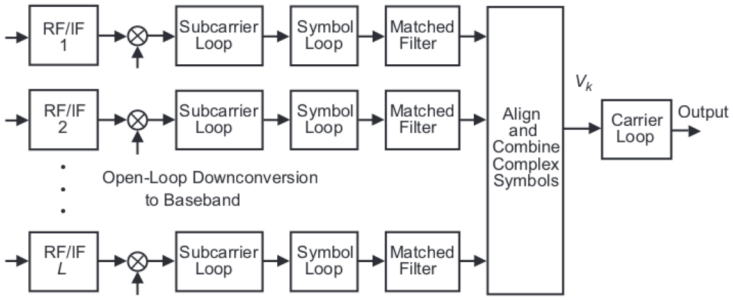

Fig. 6-7. The complex-symbol combining (CSC) algorithm for an *L*-antenna array.

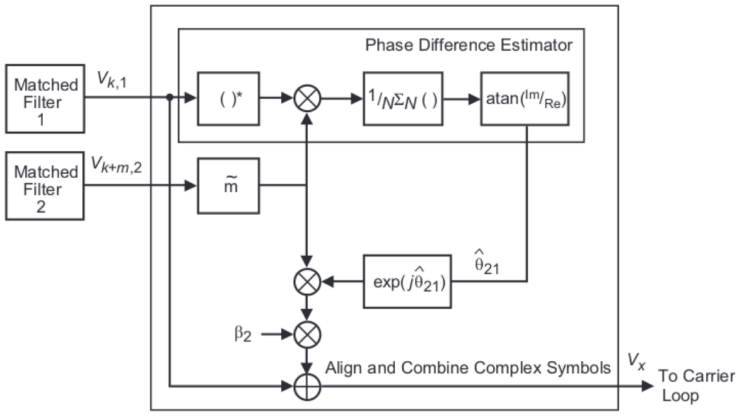

Fig. 6-8. CSC align and combine for a two-antenna array.

antenna is able to lock on the signal individually. The disadvantage of CSC is that L subcarrier and L symbol-tracking devices are needed, and each suffers some degradation.

The subcarrier and symbol loops used for CSC can be the same as those used in FSC or they can be slightly modified versions that take advantage of both the in-phase (I) and quadrature-phase (Q) components of the signal. CSC implementations with the same loops as in the FSC would use either the I- or Q-component of the baseband signal. In either case, the loop SNRs of the subcarrier and symbol loops need to be recomputed since the loop input can no longer be assumed to have carrier lock. Let ρ_{sci}^{I} denote the loop SNR of the ith subcarrier loop when either the I- or Q-arm is used (i.e., the unmodified loop), and let ρ_{sci}^{IQ} denote the subcarrier-loop SNR when both the I- and Q-arms are used (i.e., the modified loop). Similarly, define ρ_{syi}^{I} and ρ_{syi}^{IQ} for the ith symbol loop; then, from Appendix F, we have

$$\begin{aligned}
\rho_{sci}^{I} &= \left(\frac{2}{\pi}\right)^2 \frac{P_{di}/N_{0i}}{2B_{sci}w_{sci}}\left(1+\frac{1}{P_{di}T_s/N_{0i}}\right)^{-1} \\
\rho_{sci}^{IQ} &= \left(\frac{2}{\pi}\right)^2 \frac{P_{di}/N_{0i}}{B_{sci}w_{sci}}\left(1+\frac{1}{P_{di}T_s/N_{0i}}\right)^{-1} \\
\rho_{syi}^{I} &= \frac{1}{2\pi^2}\frac{P_{di}/N_{0i}}{B_{syi}w_{syi}}\mathrm{L}_I \\
\rho_{syi}^{IQ} &= \frac{1}{2\pi^2}\frac{P_{di}/N_{0i}}{B_{syi}w_{syi}}\mathrm{L}_{IQ}
\end{aligned} \tag{6.2-1}$$

where $B_{sci}w_{sci}$ and $B_{syi}w_{syi}$ are the window-loop bandwidth products of the ith subcarrier and symbol loops, respectively. Squaring losses L_I for the unmodified loop and L_{IQ} for the modified loop are defined in Appendix F. For the Galileo S-Band Mission (see parameters specified in the numerical examples of Chapter 7), it is shown in Appendix F that using the unmodified subcarrier and symbol loop reduces the loop SNR by 6 dB as compared with the carrier-locked case, and that utilizing both the I- and Q-arms recovers 3 of the 6 dB. Consequently, since the modified subcarrier and symbol loops result in an improved performance, they will be used in this section when comparing CSC with FSC. (The actual operating bandwidths for the modified and unmodified subcarrier and symbol loops also are investigated in Appendix F.)

Referring to Fig. 6-7, the combining gain is maximized by aligning the baseband signals in time and phase prior to combining. The alignment algorithm for an array of two antennas is shown in Fig. 6-8. Here signal 1 is

assumed to be delayed by m symbols with respect to signal 2. Therefore, the signals are time aligned by delaying signal 2 by $\tilde{m}$ symbols, where $\tilde{m}$ is an estimate of m. As in FSC, we assume perfect time alignment so that $\tilde{m} = m$. After time alignment, the phase of signal 2 with respect to signal 1 is assumed to be θ_{21} rad. Hence, the signals are phase aligned by rotating signal 2 by the phase estimator output $\hat{\theta}_{21}$.

The analysis of CSC degradation begins with the expression for the output of the matched filter in Fig. 6-7. Note that there are actually $2L$ matched filters per L antennas because, after subcarrier demodulation, a real symbol stream is modulated by I- and Q-baseband tones. Using complex notation, the matched-filter output stream corresponding to the kth symbol and the ith antenna, conditioned on ϕ_{sci} and ϕ_{syi}, can be written as

$$\mathbf{v}_{k\,i} = \sqrt{P_i} C_{sci} C_{syi} d_k e^{j[\Delta\omega_c t_k + \theta_{i1}]} + \mathbf{n}_{k\,i} \tag{6.2-2}$$

where the noise $\mathbf{n}_{k\,i}$ is a complex Gaussian random variable with variance N_{0i}/T_s. The subcarrier- and symbol-reduction functions, C_{sci} and C_{syi}, are given by Eq. (5.2-9) after replacing ϕ_{sc} by ϕ_{sci} and ϕ_{sy} by ϕ_{syi}. The baseband carrier frequency $\Delta\omega_c/(2\pi)$ is equal to the difference between the predicted and actual IF carrier frequencies and is assumed to be much less than the symbol rate, i.e., $\Delta f_c << 1/T_s$. The degradation at the output of the matched filter when the carrier is open-loop downconverted is approximately given as

$$D_{\Delta f_c} = \left(\frac{\sin(\Delta f_c T_s / 2)}{\Delta f_c T_s / 2} \right)^2 \tag{6.2-3}$$

Figure 6-9 illustrates the matched-filter degradation as a function of $\Delta f_c T_s$, and it is clear that the degradation is less than 0.0129 dB when $\Delta f_c T_s < 0.03$.

The combined signal after phase compensation, $\mathbf{v}_k$ in Fig. 6-7, is given as

$$\mathbf{v}_k = \sum_{i=1}^{L} \beta_i \mathbf{v}_{k\,i} e^{-j\hat{\theta}_{i1}} \tag{6.2-4}$$

where $\mathbf{v}_{k\,i}$ is given in Eq. (6.2-2) and $\hat{\theta}_{i1}$ is an estimate of θ_{i1}.

After substituting Eq. (6.2-2), the combined signal can be rewritten as follows (see Appendix G):

$$\mathbf{v}_k = \sqrt{P'} d_k e^{j[\Delta\omega_c t_k + \theta_v]} + \mathbf{n}_k \tag{6.2-5}$$

where the variance of the combined complex noise is given as [3]

$$\sigma_{\mathbf{n}_k}^2 = \frac{N_{01}}{T_s}\sum_{i=1}^{L}\gamma_i = \frac{N_{01}}{T_s}\Gamma \tag{6.2-6}$$

The conditional combined signal power, P', is given as

$$P' = P_1\sum_{i=1}^{L}\sum_{j=1}^{L}\gamma_i\gamma_j C_{sci}C_{scj}C_{syi}C_{syj}C_{ij} \tag{6.2-7}$$

where $C_{ij} = e^{j[\Delta\phi_{i1}-\Delta\phi_{j1}]}$ [as in Eq. (6.1-23)]. The signal $\mathbf{v}_k$ then is demodulated using a baseband Costas loop with output equal to $e^{-j(\Delta\omega_c t_k + \hat{\theta}_v)}$, where $\hat{\theta}_{\mathbf{v}}$ is an estimate of $\theta_{\mathbf{v}}$. The demodulator output is a real combined symbol stream and can be represented as

$$v_k = \sqrt{P'}C_c d_k + n_k \tag{6.2-8}$$

where C_c and P' are respectively given by Eqs. (5.2-9) and (6.2-7). The noise n_k is a real Gaussian random variable with variance $\sigma_n^2 = \sigma_{\mathbf{n}}^2/2$, where $\sigma_{\mathbf{n}}^2$ is given by Eq. (6.2-6). The SNR conditioned on $\phi_c, \phi_{sci}, \phi_{syi,}\ \Delta\phi_{i1}$, denoted SNR'_{csc}, is defined as the square of the conditional mean of v_k divided by the conditional variance of v_k, i.e.,

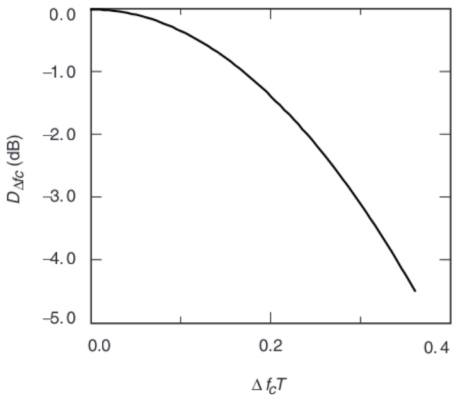

Fig. 6-9. Degradation at the matched-filter output versus the carrier frequency error–symbol time product.

$$\mathrm{SNR}'_{csc} = \frac{2P_1T_s}{N_{01}} C_c^2 \frac{\sum_{i=1}^{L}\sum_{j=1}^{L} \gamma_i\gamma_j C_{sci}C_{scj}C_{syi}C_{syj}C_{ij}}{\Gamma} \tag{6.2-9}$$

6.2.1 Telemetry Performance

The degradation is found, as before, by dividing the unconditional CSC SNR, which includes the effects of synchronization and alignment errors, by the ideal SNR. The unconditional SNR, denoted SNR_{csc}, is computed by taking the statistical expectation of SNR'_{csc} with respect to $\phi_c, \phi_{sci}, \phi_{syi}, \Delta\phi_{i1}$. The phase probability densities are assumed to be the same as before. In addition, ϕ_{sci} and ϕs_{scj} are assumed to be independent when $i \neq j$, and the same is true for ϕ_{syi} and ϕ_{syj}. Consequently,

$$\mathrm{SNR}_{csc} = \frac{2P_1T_s}{N_{01}} \overline{C_c^2} \frac{\sum_{i=1}^{L} \gamma_i^2 \overline{C_{sci}^2}\,\overline{C_{syi}^2} + \sum_{i=1}^{L}\sum_{j=1}^{L} \gamma_i\gamma_j \overline{C}_{sci}\overline{C}_{scj}\overline{C}_{syi}\overline{C}_{syj}\overline{C}_{ij}}{\Gamma} \tag{6.2-10}$$

where the average signal-reduction function due to phase misalignment between baseband signals *i* and *j*, denoted $\overline{C}_{ij}$, is given by Eq. (6.1-23) with $\sigma^2_{\Delta\phi i1} = 1/\mathrm{SNR}_{csci1}$. The CSC correlator SNR, or $\mathrm{SNR}_{\mathrm{csc}i1}$, is shown in Appendix G to be

$$\mathrm{SNR}_{csci1} = \frac{P_1}{N_{01}} \frac{T\,\overline{C_{sci}^2}\,\overline{C_{sc1}^2}\,\overline{C_{syi}^2}\,\overline{C_{sy1}^2}}{\overline{C_{sci}^2}\,\overline{C_{syi}^2} + \overline{C_{sc1}^2}\,\overline{C_{sy1}^2}\,\dfrac{1}{\gamma_i} + \dfrac{N_{0i}}{PT_s}} \tag{6.2-11}$$

where T is the averaging time of the correlator and T_s is the symbol period. The loop-reduction functions $\overline{C_{sci}}, \overline{C_{sci}^2}$, $\overline{C_{syi}}$, and $\overline{C_{syi}^2}$ for the *i*th subcarrier and symbol loops are given by Eq. (5.2-9), where the loop SNRs are given by Eqs. (E-7) and (E-14).

The carrier-loop loss $\overline{C_c^2}$ also is given by Eq. (5.2-9) with the loop SNR ρ_c in that equation computed using the average combined power $P'/N_{0\,eff}$, found by averaging Eq. (6.2-7) over all phases and dividing by the effective noise level, $N_{0\,eff} = T_s\sigma^2_{\mathbf{n}}$. Ideally, with no phase errors, $\overline{C_c^2} = \overline{C_{sc}^2} = \overline{C_{sy}^2} = \overline{C_{sc}} = \overline{C_{sy}} = \overline{C_{ij}} = 1$ and Eq. (6.2-10) reduces to $2P_1T_s\Gamma/N_{01}$, as expected. The degradation will be

$$D_{\text{csc}} = 10\log\left[\overline{C_c^2}\,\frac{\sum_{i=1}^{L}\gamma_i^2\overline{C_{sc\,i}^2}\,\overline{C_{sy\,i}^2} + \sum_{i=1}^{L}\sum_{\substack{j=1\\ i\neq j}}^{L}\gamma_i\gamma_j\overline{C}_{sc\,i}\overline{C}_{sc\,j}\overline{C}_{sy\,i}\overline{C}_{sy\,j}\overline{C}_{ij}}{\Gamma^2}\right] \quad (6.2\text{-}12)$$

Several examples of this scheme for the Galileo Mission are given in the numerical examples of Chapter 7.

6.3 Symbol-Stream Combining (SSC)

SSC involves the arraying of real symbols, as opposed to complex symbols. As with CSC, the advantage of SSC is that the combining loss is negligible [4] and is performed in the data-rate bandwidth. Moreover, antennas that are continents apart can transmit their symbols in real or nonreal time to a central location, where the symbol-stream combiner outputs the final symbols. However, that requires each antenna to be able to lock on the signal individually. The disadvantage of SSC is that L carrier, L subcarrier, and L symbol-tracking devices are needed, and each suffers some degradation. For moderate-to-high modulation indices, the carrier degradation can be reduced by employing sideband aiding at each antenna.

As depicted in Fig. 6-10, each antenna tracks the carrier and the subcarrier and performs symbol synchronization individually. The symbols at the output of each receiver then are combined with the appropriate weights to form the final detected symbols. The samples of the signal at the output of the symbol-stream combiner are

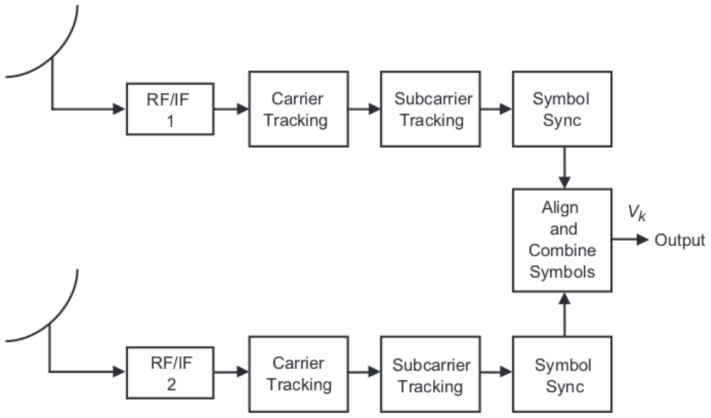

Fig. 6-10. Symbol-stream combining (SSC).

$$v_k = d_k \sum_{i=1}^{L} \beta_i \sqrt{P_{di}} C_{ci} C_{sci} C_{syi} + n'_k \tag{6.3-1}$$

where the β_i are weighing factors given by Eq. (6.1-19), $P_{di} = P_i \sin^2 \Delta$ is the received data power at antenna i (P_i is the total received power), and C_{ci}, C_{sci}, and C_{syi} are the degradation functions at the ith antenna, as defined in Eq. (5.2-9). There is negligible loss when combining the symbols (<0.05 dB), and, assuming that each receiver chain has a one-sided noise power spectral density level N_{0i}, it is straightforward to show [5] that the variance of n'_k is given by

$$\sigma^2_{n'_k} = \frac{1}{2T_s} \sum_{i=1}^{L} \beta_i^2 N_{0i} \tag{6.3-2}$$

The conditional symbol SNR (assuming that the various phase errors are known) at the output of the combiner is

$$\mathrm{SNR}'_{ssc} = \frac{\left[\overline{v_k}\right]^2}{\sigma^2_{n'}} \tag{6.3-3}$$

where $\overline{v}_k$ is the mean of v_k conditioned on $\phi_{ci}, \phi_{sci}, \phi_{syi}$ for i=1,...,L. Using Eqs. (6.1-10), (6.3-1), and (6.3-2) in Eq. (6.3-3), we get

$$\mathrm{SNR}'_{ssc} = \frac{2P_{d1}T_s}{N_{01}} \frac{\left(\sum_{i=1}^{L} \gamma_i C_{ci} C_{sci} C_{syi} \right)^2}{\Gamma} \tag{6.3-4}$$

Note that, in the absence of any degradation, the conditional SNR simplifies to

$$\mathrm{SNR}_{\mathrm{ideal}} = \frac{2P_{d1}T_s}{N_{01}} \sum_{i=1}^{L} \gamma_i = \frac{2P_{d1}T_s}{N_{01}} \Gamma \tag{6.3-5}$$

with Γ being the ideal gain factor obtained at antenna 1, which again for convenience is denoted as the master antenna. For L identical antennas with equal noise temperatures, we have $\gamma_i = \gamma_1 = 1$ for i = 2...L, and the ideal SNR reduces to $2LP_{d1}T_s / N_{01}$, as expected. The actual SNR at the output of the symbol combiner is obtained by averaging the conditional SNR over the unknown phase errors, which are embedded in the constants $C_{ci}C_{sci}C_{syi}$ defined in Eq. (5.1-5), i.e.,

$$\mathrm{SNR}_{ssc} = \frac{2P_{d1}T_s}{N_{01}}\left(\frac{\sum_{i=1}^{L}\gamma_i^2\overline{C_{ci}^2}\,\overline{C_{sci}^2}\,\overline{C_{syi}^2} + \sum_{i=1}^{L}\sum_{\substack{j=1\\ i\neq j}}^{L}\gamma_i\gamma_j\,\overline{C}_{ci}\overline{C}_{sci}\overline{C}_{syi}\,\overline{C}_{cj}\overline{C}_{scj}\overline{C}_{syj}}{\Gamma}\right) \tag{6.3-6}$$

Because the noise processes make all the phase errors mutually independent, the computation of the unconditional SNR in Eq. (6.3-6) reduces to the computation of the first two moments of the various C_{ci}, C_{sci}, and C_{syi} given in Eq. (5.2-9). Finally, we define the SNR degradation factor D_{ssc} (in decibels) for symbol-stream combining as

$$\begin{aligned} D_{ssc} &= 10\log_{10}\left(\frac{\mathrm{SNR}_{ssc}}{\mathrm{SNR}_{ideal}}\right) \\ &= 10\log_{10}\left(\frac{\sum_{i=1}^{L}\gamma_i^2\overline{C_{ci}^2}\,\overline{C_{sci}^2}\,\overline{C_{syi}^2} + \sum_{i=1}^{L}\sum_{\substack{j=1\\ i\neq j}}^{L}\gamma_i\gamma_j\,\overline{C}_{ci}\overline{C}_{sci}\overline{C}_{syi}\,\overline{C}_{cj}\overline{C}_{scj}\overline{C}_{syj}}{\Gamma^2}\right) \end{aligned} \tag{6.3-7}$$

Figures 6-11 and 6-12 depict D_{ssc} for an array of the same three antennas as were used in the FSC example as a function of P/N_0 of the master antenna (Fig. 6-11) and of the modulation index (Fig. 6-12). Also depicted is the degradation due to any single synchronization step (such as carrier, subcarrier, or symbol) obtained by setting the contribution due to the other steps to zero.

6.4 Baseband Combining (BC)

In baseband combining, each antenna locks on the carrier signal, as depicted in Fig. 6-13. The baseband signals, consisting of data on a subcarrier, are digitized, aligned in time, and combined, and the symbols are demodulated. The combined digital symbols can be modeled as

$$v_k = d_k C_{sc} C_{sy} \sum_{i=1}^{L} \beta_i \sqrt{P_{di}}\, C_{ci} C_{bbi} + n_k' \tag{6.4-1}$$

where $C_{bbi} = (1 - 2m|\tau_i|)$ is the signal-reduction function for the baseband combiner, m is the ratio of the subcarrier frequency over the symbol rate, and τ_i is the delay error of the ith telemetry time-aligning loop ($\tau_1 = 0$) [6]. For the combined signal, only one subcarrier and one symbol-tracking loop are

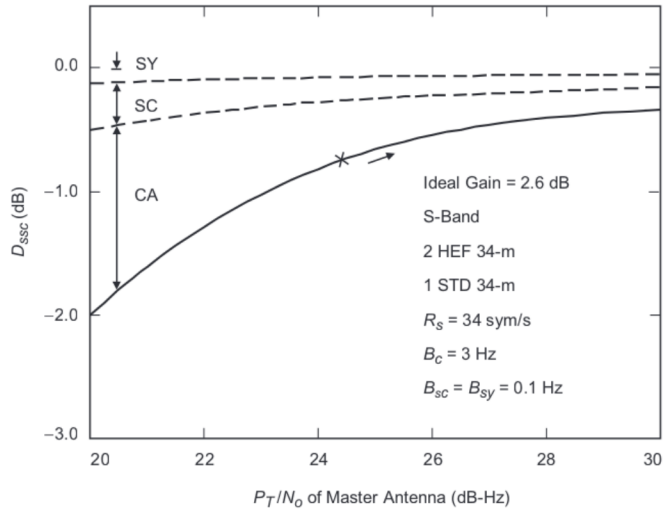

Fig. 6-11. The degradation of SSC versus P_1/N_{01} for a modulation index of 65.9 deg.

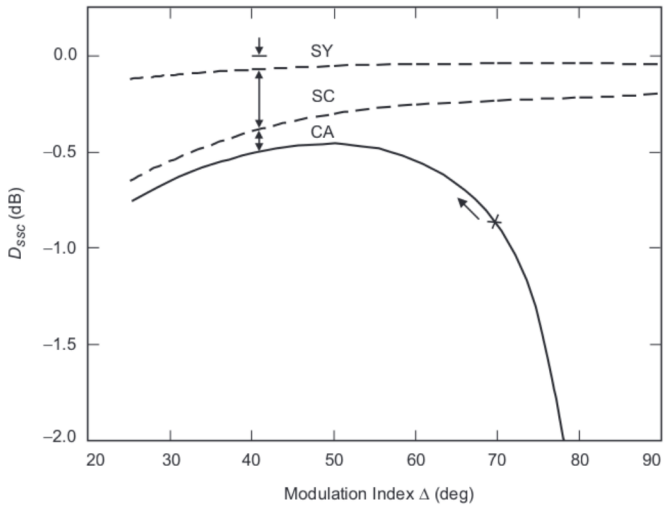

Fig. 6-12. The degradation of SSC versus modulation index for a P_1/N_{01} of 25 dB-Hz.

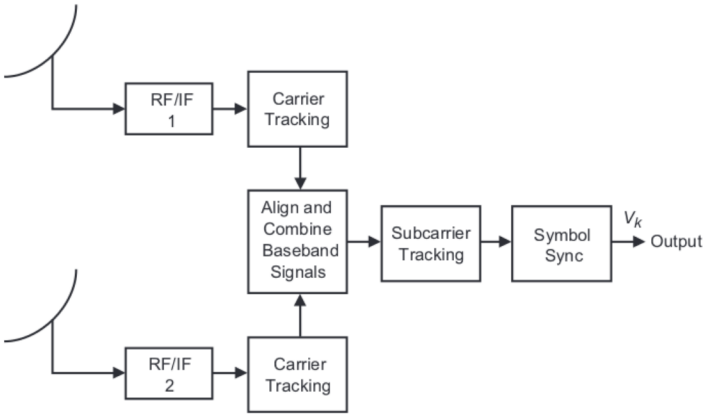

Fig. 6-13. Baseband combining (BC).

employed and, hence, no subscripts are needed for the random variables ϕ_{sc} and ϕ_{sy}. The variance of v_k due to thermal noise still is given by Eq. (6.3-2). Again, as with the SSC scheme, the conditional SNR at the output of the matched filter is given by

$$\mathrm{SNR}'_{bc} = \frac{\left(\overline{v_k \mid \phi_c, \phi_{sc}, \phi_{sy}, \tau_i}\right)^2}{N_{01}} = \frac{2P_{d1}T_s}{N_{01}} C_{sc}^2 C_{sy}^2 \frac{\left(\sum_{i=1}^{L} \gamma_i C_{c\,i} C_{bb\,i}\right)^2}{\Gamma} \tag{6.4-2}$$

In order to compute the unconditional SNR, we have to average Eq. (6.4-2) over all the phase- and delay-error processes in the corresponding tracking loops, resulting in

$$\mathrm{SNR}_{bc} = \frac{2P_{d1}T_s}{N_{01}} \overline{C_{sc}^2}\,\overline{C_{sy}^2} \left(\frac{\sum_{i=1}^{L} \gamma_i^2 \overline{C_{c\,i}^2}\,\overline{C_{bb\,i}^2} + \sum_{i,j} \sum_{i \neq j} \gamma_i \gamma_j \overline{C}_{c\,i} \overline{C}_{c\,j} \overline{C}_{bb\,i} \overline{C}_{bb\,j}}{\Gamma} \right) \tag{6.4-3}$$

The signal-reduction function for the time alignment of baseband signals, $C_{bb\,i}$, has the following first two moments:

$$\overline{C}_{bbi} = \left(1 - 2m\sqrt{\frac{2}{\pi}}\sigma_{\tau i}\right)$$
$$\overline{C_{bbi}^2} = \left(1 - 4m\sqrt{\frac{2}{\pi}}\sigma_{\tau i} + 4m^2\sigma_{\tau i}^2\right) \tag{6.4-4}$$

where $\sigma_{\tau i}^2$ denotes the variance of the ith time-aligning loop and is computed to be [6]

$$\sigma_{\tau i}^2 = \frac{B_{\tau i}}{B_n 32 m^2}\left(\frac{1}{\left[erf\left(\sqrt{P_{d1}\sigma_1^2}\right)erf\left(\sqrt{P_{di}\sigma_i^2}\right)\right]^2} - 1\right), \quad i = 2,...,L \tag{6.4-5}$$

In the above equation, $B_{\tau i}$ denotes the bandwidth of the time-aligning loops, B_n the noise bandwidth at the input to the digitizer (assumed to be the same in all channels), and $\sigma_i^2 = N_{0i}B_n$ (note that $\overline{C}_{bbi} = 1$ and $\overline{C_{bbi}^2} = 1$). The equations for the moments of C_{sc} and C_{sy} are those given by Eq. (5.2-9) with the variances computed using the combined P_d / N_0. Note that under ideal conditions (i.e., no phase or delay errors in the tracking loops), all C's are 1, and the SNR reduces to

$$\mathrm{SNR}_{\mathrm{ideal}} = \frac{2P_{d1}T_s}{N_{01}}\Gamma \tag{6.4-6}$$

as in the symbol-stream combining case [Eq. (6.3-5)]. As expected, BC has the same SNR performance as other schemes under ideal conditions. Once the unconditional SNR is computed for the BC scheme using Eq. (6.4-3), the degradation factor is obtained as before, namely,

$$D_{bc} = 10\log_{10}\left(\frac{\mathrm{SNR}_{\mathrm{bc}}}{\mathrm{SNR}_{\mathrm{ideal}}}\right)$$
$$= 10\log_{10}\left(\frac{\overline{C_{sc}^2}\,\overline{C_{sy}^2}\sum_{i=1}^{L}\gamma_i^2\overline{C_{ci}^2}\,\overline{C_{bbi}^2} + \sum_{i,j}\sum_{i\neq j}\gamma_i\gamma_j\overline{C}_{ci}\overline{C}_{cj}\overline{C}_{bbi}\overline{C}_{bbj}}{\Gamma^2}\right) \tag{6.4-7}$$

Figures 6-14 and 6-15 depict the degradation due to baseband combining, D_{bc}, as a function of both P_1 / N_{01} (Fig. 6-14) and Δ (Fig. 6-15), assuming the same array as in the FSC case. Note from Fig. 6-14 that the subcarrier and

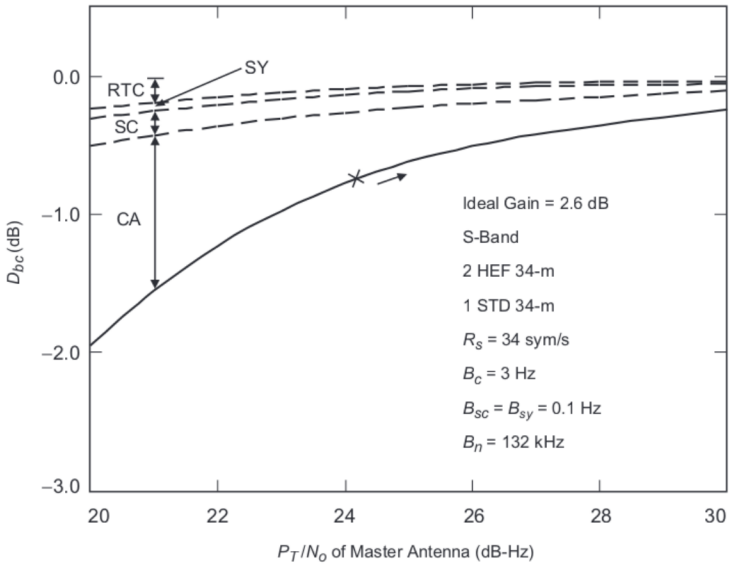

Fig. 6-14. The degradation of BC versus P_1/N_{01} for a modulation index of 65.9 deg.

symbol degradations are less than their counterparts in SSC (Fig. 6-11) because these loops track the combined signal.

6.5 Carrier Arraying (CA)

In carrier arraying, several carrier-tracking loops are coupled in order to enhance the received carrier signal-to-noise ratio and, hence, decrease the telemetry (radio) loss due to imperfect carrier synchronization. The coupling can be performed using phase-locked loops (PLLs) for residual carriers or Costas loops for suppressed BPSK carriers. Only the PLL case is considered here to illustrate the idea of carrier arraying. A general block diagram is shown in Fig. 6-16, where two carrier loops share information to jointly improve their performance, as opposed to tracking individually. Carrier arraying by itself does not combine the data and thus needs to operate with baseband combining or symbol-stream combining to array the telemetry. This is shown in Fig. 6-16, where baseband combining is employed to array the data spectrums.

There are basically two scenarios in which one would employ carrier arraying. In the first scenario, a large antenna locks on the signal by itself and

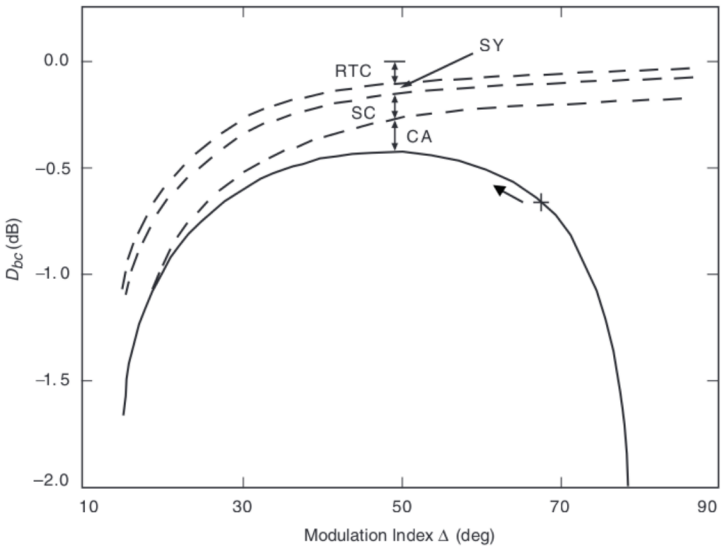

Fig. 6-15. The degradation of BC versus modulation index for a P_1/N_{01} of 25 dB-Hz.

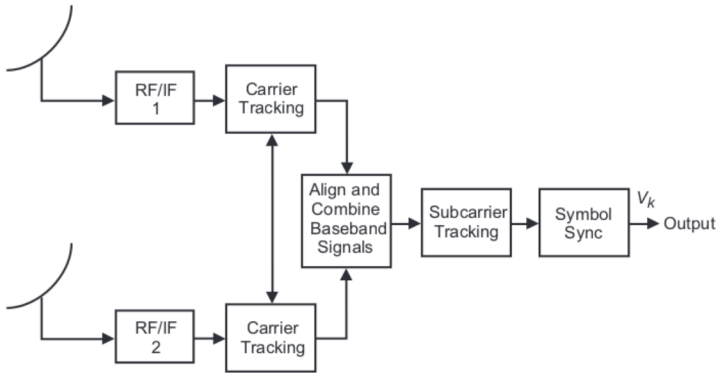

Fig. 6-16. Carrier arraying with baseband combining (CA/BC).

then helps a smaller antenna track. In this case, the signal might experience dynamics requiring a large loop bandwidth and, hence, the signal would have to be strong enough to enable the carrier loop to operate with the large bandwidth. A large antenna with a strong signal first is used to track the signal and then the dynamics of the signal are estimated and removed from the weaker signal to enable the other carrier loop to operate with a smaller bandwidth and, hence, a higher loop SNR. In the second scenario, the signal is too weak to be tracked by any single antenna but can be tracked jointly by two or more antennas. The combining methods used in the latter case are similar to those employed in FSC when aligning the phases of pure tones (hence, requiring a smaller correlator bandwidth). In either scenario, carrier arraying can be implemented in one of two ways—at baseband or at an intermediate frequency (IF).

6.5.1 Baseband Carrier-Arraying Scheme

Baseband carrier arraying is illustrated in Fig. 6-17, where the error signals at the output of the phase detectors are combined at baseband. This scheme is analyzed in [7], where it is shown that the variance of the phase-jitter process in the master PLL is given by

$$\sigma_{c1}^2 = \frac{1}{2\pi j}\oint\left[\frac{H_1(z)}{1+\sum_{i=2}^{L}\gamma_i H_1(z)[1-H_i(z)]}\right]^2 \frac{dz}{z}\frac{N_{01}}{2T_{c1}P_{c1}} + \sum_{i=2}^{L}\gamma_i^2\frac{1}{2\pi j}\oint\left[\frac{H_1(z)[1-H_i(z)]}{1+\sum_{i=2}^{L}\gamma_i H_1(z)[1-H_i(z)]}\right]^2 \frac{dz}{z}\frac{N_{0i}}{2T_{ci}P_{ci}} \tag{6.5-1}$$

where $H_i(z)$ is the closed-loop transfer function of the ith loop and T_{ci} is the loop update time. The above integral is difficult to evaluate in general. However, when $B_{ci} \ll B_{c1}$ for $i = 2,...,L$, which is the preferred mode of operation, the above integral can be approximated by

$$\sigma_{c1}^2 = \frac{B_{ci}\sum_{i=1}^{L}\beta_i^2 N_{0i}}{P_{c1}\Gamma^2} \tag{6.5-2}$$

which assumes ideal performance. In this case, the master-loop SNR becomes

$$\rho_{c1} = \frac{P_{c1}}{B_{c1}N_{01}}\Gamma \tag{6.5-3}$$

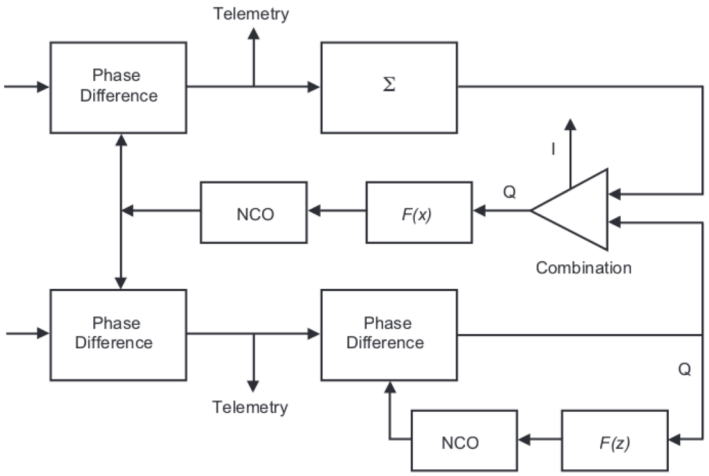

Fig. 6-17. A baseband implementation of carrier arraying.

assuming identical noise spectral densities. The actual variance typically will be larger and requires the evaluation of Eq. (6.5-1), which depends on the actual loop filters implemented.

6.5.2 IF Carrier-Arraying Scheme

One form of IF carrier arraying is depicted in Fig. 6-18 and is conceptually the same as full-spectrum combining. In this case, the carrier power, P_{ci}, is substituted for the total power, P_i. So, all equations and results derived for the FSC scheme regarding the combining loss can be automatically applied to the IF carrier-arraying scheme. Phase estimation in this case can be performed by downconverting the received IFs to baseband using a precomputed model of the received Doppler and Doppler rate. The correlation can be computed at baseband using very small bandwidths B and, hence, requiring short integration times T. From Eq. (6.1-8), the variance of the ith carrier correlator is

$$\sigma_{ci}^2 = B(N_{01}P_{ci} + N_{0i}P_{c1} + N_{01}N_{0i}B) \approx N_{01}N_{0i}B^2 \tag{6.5-4}$$

while the correlator's SNR is

$$\mathrm{SNR}_c \cong \frac{P_{c1}}{N_{01}} \frac{P_{ci}}{N_{0i}} \frac{2T}{B} \tag{6.5-5}$$

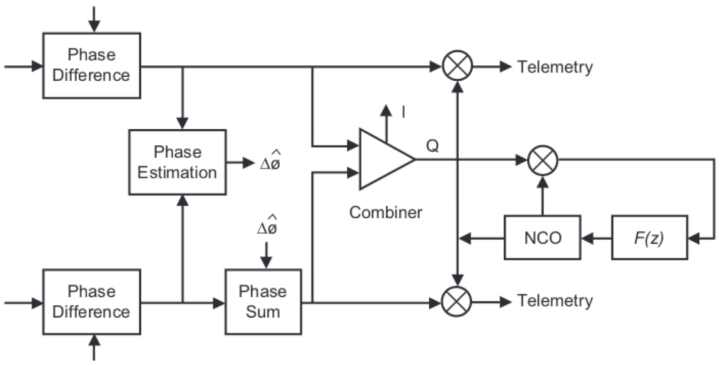

Fig. 6-18. An IF implementation of carrier arraying.

Note that, for IF carrier arraying, the bandwidth B is much narrower than that used in FSC since the data spectrum is not employed. The signal combiner performs the weighted sum of carrier signals $\mathbf{c}_i(t)$, giving the complex combined carrier signal

$$\mathbf{c}(t) = \sum_{i=1}^{L} \beta_i \left[\sqrt{P_{ci}}\, e^{j[\omega_{Ii} t + \theta_1(t) + \Delta\phi_{c\,i}(t)]} \right] + \mathbf{n}_i(t)\, e^{j[\omega_{Ii} t + \theta_1(t) + \Delta\phi_{ci}(t)]} \tag{6.5-6}$$

Following Eqs. (6.1-21) through (6.1-24), the average carrier power and the variance of the combined complex carrier signal $\mathbf{c}(t)$ are, respectively,

$$\begin{aligned} P_{\mathbf{c}} &= \sum_{i=1}^{L} \beta_i^2 P_{ci} + \sum_{i=1}^{L} \sum_{\substack{j=1 \\ i \neq j}}^{L} \beta_i \beta_j \sqrt{P_{ci} P_{cj}}\, C_{c\,ij} \\ &= P_{c1} \left(\sum_{i=1}^{L} \gamma_i^2 + \sum_{i=1}^{L} \sum_{\substack{j=1 \\ i \neq j}}^{L} \gamma_i \gamma_j C_{c\,ij} \right) \end{aligned} \tag{6.5-7}$$

and

$$\sigma_c^2 = B \sum_{i=1}^{L} \beta_i^2 N_{0i} \tag{6.5-8}$$

where

$$C_{c\,ij} = \mathbf{E}\left\{e^{j[\Delta\phi_{c,i1}(t_k)-\Delta\phi_{c\,j1}(t_k)]}\right\}$$
$$= \begin{cases} \{e^{-(1/2)[\sigma^2_{\Delta\phi_{c\,i1}}+\sigma^2_{\Delta\phi_{c\,j1}}]}, & i \neq j, \sigma^2_{\Delta\phi_{c\,11}} \equiv 0 \\ 1, & i = j \end{cases} \quad (6.5\text{-}9)$$

and

$$\sigma^2_{\Delta\phi_{cij}} = \frac{1}{\mathrm{SNR}_{cij}} \quad (6.5\text{-}10)$$

To illustrate the results with a simple example, let $P_{ci} = P_{c1}$, $N_{0i} = N_{01}$, and $\beta_i = 1$ for all antennas; then the signal and noise powers of the real process at the output of the carrier combiner become, respectively,

$$P_c = P_{c1}\left[L + 2(L-1)e^{-\sigma^2_{\Delta\phi,c}/2} + (L-2)(L-1)e^{-\sigma^2_{\Delta\phi,c}}\right] \quad (6.5\text{-}11)$$

$$\sigma^2_{\Delta\phi,c} = BLN_{01}$$

resulting in a correlator SNR:

$$\mathrm{SNR}_c = \frac{P_c}{\sigma^2_{\Delta\phi,c}}$$
$$= \frac{P_{c1}\left[L + 2(L-1)e^{-\sigma^2_{\Delta\phi,c}/2} + (L-2)(L-1)e^{-\sigma^2_{\Delta\phi,c}}\right]}{BLN_{01}} \quad (6.5\text{-}12)$$

In an ideal scenario, $\sigma^2_{\Delta\phi,c} \to 0$ and

$$\mathrm{SNR}_{c,\mathrm{ideal}} = \frac{P_{c1}L}{N_{01}B} \quad (6.5\text{-}13)$$

as expected. The combining degradation in dB for IF carrier arraying becomes

$$D_{ifc} = 10\log_{10}\left[\frac{\left[L + 2(L-1)e^{-\sigma^2_{\Delta\phi,c}/2} + (L-2)(L-1)e^{-\sigma^2_{\Delta\phi,c}}\right]}{L^2}\right] \quad (6.5\text{-}14)$$

References

[1] D. H. Rogstad, "Suppressed Carrier Full-Spectrum Combining," *The Telecommunications and Data Acquisition Progress Report 42-107, July–September 1991*, Jet Propulsion Laboratory, Pasadena, California, pp. 12–20, November 15, 1991. http://ipnpr.jpl.nasa.gov/progress_report/

[2] R. M. Hjellming, ed., *An Introduction to the NRAO Very Large Array*, National Radio Astronomy Observatory, Socorro, New Mexico, April 1993.

[3] D. Divsalar, "Symbol Stream Combining Versus Baseband Combining for Telemetry Arraying," *The Telecommunications and Data Acquisition Progress Report 42-74, April–June 1983*, Jet Propulsion Laboratory, Pasadena, California, pp. 13–28, August 15, 1983.

http://ipnpr.jpl.nasa.gov/progress_report/

[4] W. Hurd, J. Rabkin, M. D. Russell, B. Siev, H. W. Cooper, T. O. Anderson, and P. U. Winter, "Antenna Arraying of Voyager Telemetry Signals by Symbol Stream Combining," *The Telecommunications and Data Acquisition Progress Report 42-86, April–June 1986*, Jet Propulsion Laboratory, Pasadena, California, pp. 132–142, August 15, 1986.

http://ipnpr.jpl.nasa.gov/progress_report/

[5] D. Divsalar, "Symbol Stream Combining Versus Baseband Combining for Telemetry Arraying," *The Telecommunications and Data Acquisition Progress Report 42-74, April–June 1983*, Jet Propulsion Laboratory, Pasadena, California, pp. 13–28, August 15, 1983.

http://ipnpr.jpl.nasa.gov/progress_report/

[6] M. K. Simon and A. Mileant, *Performance Analysis of the DSN Baseband Assembly Real-Time Combiner*, JPL Publication 84-94, Rev. 1, May 1, 1985.

[7] D. Divsalar and J. H. Yuen, "Improved Carrier Tracking Performance with Coupled Phase-Locked Loops," *The Telecommunications and Data Acquisition Progress Report 42-66, September and October 1981*, Jet Propulsion Laboratory, Pasadena, California, pp. 148–171, December 15, 1981. http://ipnpr.jpl.nasa.gov/progress_report/

Chapter 7
Arraying Combinations and Comparisons

7.1 Arraying Combinations

Besides the individual arraying schemes described in the previous chapters, combinations of schemes can be implemented. In particular, SSC can be enhanced with SA and with CA. Similarly, BC can be enhanced with SA and with CA. FSC uses only one set of receiver, subcarrier, and symbol-tracking loops, but, again, the performance of the receiver can be improved with SA.

A comparison of all schemes and arraying combinations is depicted in Figs. 7-1 and 7-2, where the degradations of BC, SSC, FSC, SSC/SA/CA, FSC/SA, BC/SA/CA, FSC/SA, SSC/CA, BC/SA, SSC/SA, and BC/CA are all computed versus P/N_0 for a fixed Δ = 65.9 deg. These curves were computed assuming B_τ = 0.1 mHz and B_n = 135 kHz for the telemetry time-aligning loop, T/B = 0.0008 s^2 for FSC, T/B = 0.075 s^2 for CA (assumed at IF), and a symbol rate of 34 symbols per second (s/s). From Fig. 7-1, it seems that the three schemes with the least degradation at 20 dB-Hz are FSC/SA, BC/SA/CA, and SSC/SA/CA. As mentioned before, the "x" denotes the point where carrier-loop SNR has reached 8 dB and below which significant cycle slipping might occur. Most schemes seem to maintain an 8-dB minimum carrier-loop SNR for P/N_0 as low as 20 dB-Hz, except for SSC and BC, which lose lock at roughly 24 dB-Hz, and BC/CA and SSC/CA, which require a $P/N_0 \geq 21$ dB-Hz. Recall that the delay adjustment in FSC and FSC/SA was assumed to be perfect, resulting in no degradation. More realistically, a 0.1-dB degradation should be added and, hence, FSC/SA and BC/SA/CA seem to provide very similar degradations.

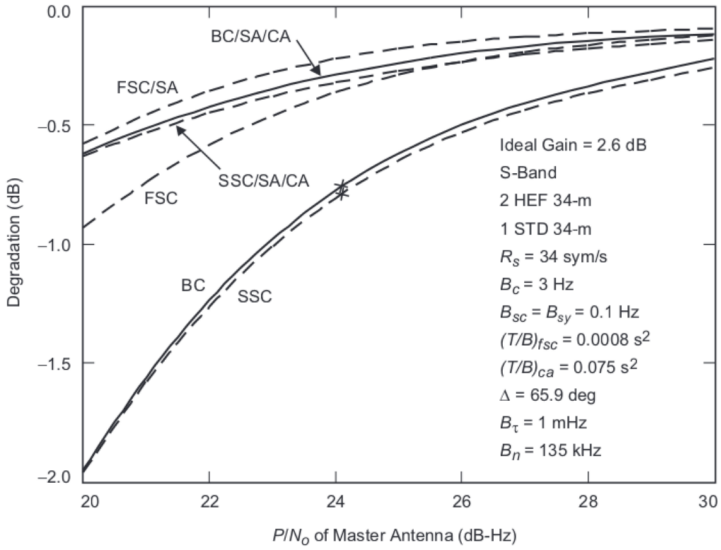

Fig. 7-1. Comparison of SSC, FSC, and FSC/SA with BC, SSC/SA, CA, and BC/SA/CA.

For this particular case, FSC requires 216 seconds of integration time (for T/B = 0.0008 and B = 2 times 135 kHz), a rather unrealistic parameter. For a shorter integration time (on the order of a few seconds), the correlator SNR degrades significantly, and the differential phase cannot be estimated. The bandwidth B can be reduced to pass only the first harmonic of the subcarrier, but that still results in unrealistic integration times. The signal can be passed through a matched filter that passes the subcarrier harmonics and the data modulation but rejects the spectrum in between the harmonics. The effective bandwidth of such a filter would be of the order of the symbol rate and, hence, would result in shorter integration times as long as the subcarrier frequency is a large multiple of the symbol rate [$m >> 1$ in Eq. (6.4-1)]. The drawback of such a filter is that it is too specific to the signal of interest and needs to be modified for each mission. Moreover, it might require frequency tuning to center the signal in the band of interest. Another technique to reduce the bandwidth is to correlate only the residual-carrier components in order to further shorten the integration time. This is precisely the technique employed in carrier arraying, when implemented at IF. It should be pointed out that even though the phase is adjusted at IF, it can and should be estimated at baseband by mixing the received IF from each antenna with a Doppler and a Doppler rate predict of the

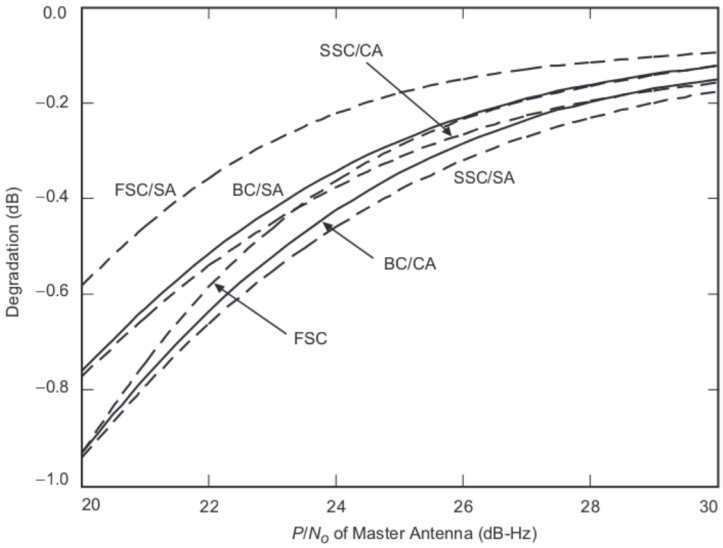

Fig. 7-2. Comparison of SSC, FSC, and FSC/SA with BC/CA, BC/SA, and SSC/CA.

signal. The outputs of the mixers consist of a tone with a very low frequency component that requires a very small bandwidth B prior to the correlation. With $T/B = 0.075$ and $T = 3$ s, $B = 40$ Hz, which requires the frequency predicts to be correct to within ± 20 Hz. Even if the error is larger than ± 20 Hz, a fast Fourier transform (FFT) can be used to reduce the frequency error at the output of the mixers such that it lies well within $B/2$ Hz.

As seen from the above example, FSC/SA and BC/SA/CA provide the least degradation and hence the best performance overall, but BC/SA/CA accomplishes that with reasonable integration times. SA enhances the performance in both cases because the carrier component is so weak due to the high modulation index and relatively low received power. For signals with stronger carriers, FSC and FSC/SA would provide similar degradations for all practical purposes, as would BC/CA and BC/SA/CA. It is worth noting at this point that FSC, as presented in this discussion, compensated for the signal delays up front and then adjusted for the phases. This is the classical arraying performed in radiometry. However, in BC/CA, CA is first employed to lock on the signal (hence, a phase adjustment) and later delay compensation is performed in the baseband assembly (BBA) to coherently add the data. The latter, which is equivalent in performance to FSC (but with shorter integration times), seems to be favored more by communication engineers, whereas FSC

seems to be favored more by astronomers. The major difference between FSC and BC/CA is the integration length required to estimate the differential phase. BC/CA offers a significant advantage by requiring much shorter integration times for spacecraft with very weak signals and a large subcarrier-to-data-rate ratio.

In either FSC or BC/CA, atmospheric effects can be significant, especially at higher frequencies and in the presence of thunderstorms. Figure 7-3 depicts the relative phase along baseline "1–3" in the Very Large Array (VLA) on a clear night and in the presence of thunderstorms. In the latter case, the integration time T needs to be short to track the phase variation. The resulting combining degradation can be 0.2 dB or even more depending on the scenario.

7.2 Numerical Examples

The results derived in Chapter 6 were applied to several existing deep-space missions managed by the DSN in order to illustrate the differences in combined symbol SNR performance. The missions considered were Pioneer 10, Voyager II, and Magellan, reflecting weak, medium, and strong signals. As expected, the weaker the signal, the harder it is to array the antennas. The Galileo Mission is treated at greater length in Section 7.2.4, reflecting a weak signal.

7.2.1 Pioneer 10

The signal received from Pioneer 10 represents the weakest signal. It is an S-band signal with the following characteristic as of May 1990: symbol rate R_s = 32 sym/s, subcarrier frequency f_s = 32768 Hz, and modulation index Δ =

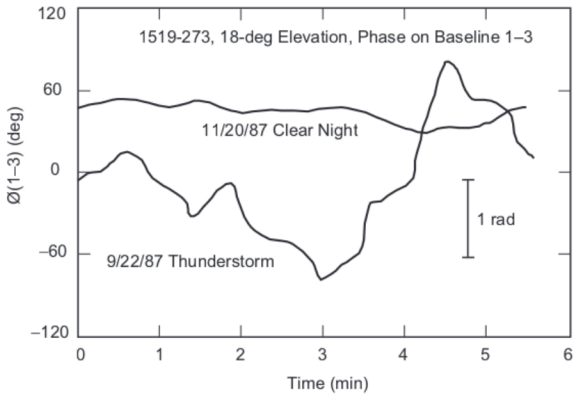

Fig. 7-3. VLA thunderstorm data at 8.4 GHz.

65.9 deg. The receiver is assumed to operate with the following parameters: carrier bandwidth B_c= 1.5 Hz (Block IV Receiver), $B_{sc} = B_{sy}$= 0.1 Hz for the subcarrier- and symbol-tracking loops, B_τ= 0.1 mHz and B_n= 135 kHz for the telemetry time-aligning loop, T/B = 0.075 for carrier arraying (B = 40 Hz and T = 3 s), and T/B = 0.0008. For FSC, two cases are considered: a regular IF filter (B = 2(135) kHz and T = 216 s!) and a matched IF filter (B = 500 Hz and T = 0.4 s). Two array configurations are considered: a 70-m and a 34-m STD antenna array, which can provide 0.68-dB gain (over the 70-m antenna) in the ideal case, and a two-70-m-antenna array (providing an ideal 3-dB gain). The degradations for both arrays are shown in Tables 7-1(a) and 7-1(b), respectively. The 20-dB-Hz signal represents the approximate level at the master antenna—in this case, the 70-m antenna.

In the first array (70 m + STD 34 m), BC and SSC cannot operate due to the inability of the STD 34-m antenna to maintain carrier lock. However, BC/SA and SSC/SA can operate with an 8-dB loop SNR, which is the minimum required to avoid cycle slipping. FSC/SA achieves the highest loop SNR at 18.2 dB, followed by BC/SA/CA and SSC/SA/CA at 17.7 dB, and followed finally by BC/SA, SSC/SA, and FSC at 11 dB. The smallest degradations are obtained with FSC/SA and BC/SA/CA at about 0.53 dB. Note that the combining loss of FSC at 0.19 dB can be reduced by integrating over longer periods. In the two-70-m-antenna array, all schemes maintain lock as expected, with the smallest degradation achieved by FSC/SA at 0.34 dB and the largest achieved by BC at 0.81 dB. FSC/SA seems to be the "best" arraying scheme for Pioneer 10, and the sideband aiding is essential in reducing the degradation. Recall that the long integration time required in FSC/SA renders the scheme impractical and, hence, BC/SA/CA is really the "best" scheme for Pioneer 10.

7.2.2 Voyager II

Unlike Pioneer 10, Voyager II can be tracked by all 34-m antennas. It represents a medium signal in both received power and data rate. The X-band signal processes the following characteristics: symbol rate = 43.2 s/s, subcarrier frequency = 360 kHz, and Δ = 77 deg. The receivers are assumed to operate with the following parameters: B_c = 10 Hz for the carrier tracking, $B_{sc} = B_{sy}$= 1.0 Hz for the subcarrier- and symbol-tracking loops, B_τ= 1 mHz and B_n= 3.2 MHz for the telemetry time-aligning loop, T/B = 0.075 for carrier arraying, and $T/B = 2.0 \times 10^{-7}$ for FSC (B = 3.2 MHz and T = 1.3 s).

Table 7-2(a) provides the degradations for all arraying schemes for a three-element array of one HEF 34-m and two STD 34-m antennas. This array can provide an ideal 3-dB gain over the HEF 34-m master antenna, with

Table 7-1(a). Pioneer 10: one 70-m and one 34-m STD antenna array.

Arraying Scheme	P_T/N_o (dB-Hz)	Total Degradation (dB)	Carrier Degradation (dB)	Subcarrier Degradation (dB)	Symbol Degradation (dB)	RTC or IF* Degradation (dB)
BC	20	No	Carrier	Lock	—	—
BC+SA	20	–0.614	–0.17	–0.25	–0.07	–0.12
BC+CA	20	–0.792	–0.34	–0.26	–0.08	–0.12
BC+SA+CA	20	–0.526	–0.07	–0.26	–0.08	–0.12
SSC	20	No	Carrier	Lock	—	—
SSC+SA	20	–0.670	–0.17	–0.39	–0.11	0.00
SSC+CA	20	–0.849	–0.34	–0.40	–0.11	0.00
SSC+SA_CA	20	–0.583	–0.07	–0.40	–0.11	0.00
FSC	20	–0.874	–0.35	–0.26	–0.08	–0.19
FSC+SA	20	–0.593	–0.07	–0.26	–0.08	–0.19
FSC (Matched filter)	20	–0.874	–0.35	–0.26	–0.08	–0.19
FSC+SA (Matched filter)	20	–0.593	–0.07	–0.26	–0.08	–0.19

* Degradation at the real-time-combiner output (RTC) in the BC cases or the intermediate-frequency output (IF) in the non-BC cases.

Table 7-1(b). Pioneer 10: two 70-m antennas array.

Arraying Scheme	P_T/N_o (dB-Hz)	Total Degradation (dB)	Carrier Degradation (dB)	Subcarrier Degradation (dB)	Symbol Degradation (dB)	RTC or IF* Degradation (dB)
BC	20	–0.812	–0.40	–0.19	–0.06	–0.17
BC+SA	20	–0.487	–0.08	–0.19	–0.06	–0.17
BC+CA	20	–0.608	–0.20	–0.19	–0.06	–0.17
BC+SA+CA	20	–0.475	–0.06	–0.19	–0.06	–0.17
SSC	20	–0.768	–0.40	–0.29	–0.08	0.00
SSC+SA	20	–0.444	–0.08	–0.29	–0.08	0.00
SSC+CA	20	–0.565	–0.20	–0.29	–0.08	0.00
SSC+SA_CA	20	–0.432	–0.06	–0.29	–0.08	0.00
FSC	20	–0.509	–0.20	–0.19	–0.06	–0.07
FSC+SA	20	–0.347	–0.04	–0.19	–0.06	–0.07
FSC (Matched filter)	20	–0.509	–0.20	–0.19	–0.06	–0.07
FSC+SA (Matched filter)	20	–0.347	–0.04	–0.19	–0.06	–0.07

* Degradation at the real-time-combiner output (RTC) in the BC cases or the intermediate-frequency output (IF) in the non-BC cases.

Table 7-2(a). Voyager 2: one master 34-m HEF and two 34-m STD antennas array.

Arraying Scheme	P_T/N_o (dB-Hz)	Total Degradation (dB)	Carrier Degradation (dB)	Subcarrier Degradation (dB)	Symbol Degradation (dB)	RTC or IF* Degradation (dB)
BC	39	–0.346	–0.16	–0.11	–0.03	–0.04
BC+SA	39	–0.219	–0.04	–0.11	–0.03	–0.04
BC+CA	39	–0.236	–0.05	–0.11	–0.03	–0.04
BC+SA+CA	39	–0.197	–0.02	–0.11	–0.03	–0.04
SSC	39	–0.548	–0.16	–0.31	–0.08	0.00
SSC+SA	39	–0.422	–0.04	–0.31	–0.08	0.00
SSC+CA	39	–0.439	–0.05	–0.31	–0.08	0.00
SSC+SA_CA	39	–0.400	–0.02	–0.31	–0.08	0.00
FSC	39	–0.284	–0.06	–0.11	–0.03	0.09
FSC+SA	39	–0.235	–0.01	–0.11	–0.03	0.09

* Degradation at the real-time-combiner output (RTC) in the BC cases or the intermediate-frequency output (IF) in the non-BC cases.

P/N_0 =39 dB-Hz. The second array also consists of three elements: one 70-m antenna, one STD 34-m antenna, and one HEF 34-m antenna. Its performance is shown in Table 7-2(b). The master in this case is the 70-m antenna with P_t/N_0 = 45 dB-Hz. This array can provide a maximum gain of 1.43 dB. BC/SA, BC/CA, and BC/SA/CA can provide the least degradations if the combining loss is maintained below 0.01 dB. On the other hand, FSC/SA provides a better performance for a more realistic 0.07-dB IF degradation. For all practical purposes, both FSC and BC/CA perform equally with realistic integration times.

7.2.3 Magellan

The highest data rate signal is transmitted by Magellan at X-band with 537.6 ks/s, a 960-kHz subcarrier frequency, and a 78-deg modulation index. Tables 7-3(a) and 7-3(b) provide the degradations for an array of one HEF 34-m antenna and one STD 34-m antenna (providing a 1.76-dB ideal gain over the HEF 34-m master antenna) and another array of one 70-m antenna, one HEF 34-m antenna, and one STD 34-m antenna (providing a 1.43-dB ideal gain over the 70-m master antenna). The receivers are assumed to operate with B_c= 30 Hz for the carrier tracking, $B_{sc} = B_{sy}$ = 3.0 Hz for the subcarrier- and symbol-tracking loops, B_τ= 10 mHz and B_n= 4.5 MHz for the telemetry time-aligning loop, T/B = 0.075 for carrier arraying, and T/B = 10^{-10} for FSC. In this case, all combining methods provide near-optimum performances for both arrays.

7.2.4 Galileo

The FSC and CSC performance for different combinations of 70-m and 34-m antennas is compared here for the Galileo Mission. The IF signals in FSC typically are transmitted to a central location before being combined and demodulated using a single receiver. However, since the retransmission channel is bandlimited, the most significant harmonics are brought to near baseband before transmission and combining. Million et al. discuss this variation of the FSC scheme in [1]. When the number of subcarrier harmonics present at the combiner input is four, the energy lost is 0.22 dB. The retransmission of CSC signals to a central location, on the other hand, does not result in an energy loss because the symbol rates for Galileo (less than 640 sym/s) can be easily supported by the retransmission channel. The following cases are considered: two 70-m antennas, and one 70-m antenna plus from one to four 34-m STD antennas.

Table 7-2(b). Voyager 2: one 70-m, one 34-m HEF, and one 34-m STD antenna array.

Arraying Scheme	P_T/N_o (dB-Hz)	Total Degradation (dB)	Carrier Degradation (dB)	Subcarrier Degradation (dB)	Symbol Degradation (dB)	RTC or IF* Degradation (dB)
BC	45	–0.130	–0.06	–0.05	–0.01	–0.01
BC+SA	45	–0.084	–0.01	–0.05	–0.01	–0.01
BC+CA	45	–0.091	–0.02	–0.05	–0.01	–0.01
BC+SA+CA	45	–0.077	–0.01	–0.05	–0.01	–0.01
SSC	45	–0.208	–0.06	–0.12	–0.03	0.00
SSC+SA	45	–0.163	–0.01	–0.12	–0.03	0.00
SSC+CA	45	–0.170	–0.02	–0.12	–0.03	0.00
SSC+SA_CA	45	–0.156	–0.01	–0.12	–0.03	0.00
FSC	45	–0.148	–0.02	–0.05	–0.01	–0.07
FSC+SA	45	–0.134	–0.01	–0.05	–0.01	–0.07

* Degradation at the real-time-combiner output (RTC) in the BC cases or the intermediate-frequency output (IF) in the non-BC cases.

Table 7-3(a). Magellan: one master 34-m HEF and one 34-m STD antenna array.

Arraying Scheme	P_T/N_o (dB-Hz)	Total Degradation (dB)	Carrier Degradation (dB)	Subcarrier Degradation (dB)	Symbol Degradation (dB)	RTC or IF* Degradation (dB)
BC	59	–0.022	–0.01	–0.01	0.00	0.00
BC+SA	59	–0.022	–0.01	–0.01	0.00	0.00
BC+CA	59	–0.022	–0.01	–0.01	0.00	0.00
BC+SA+CA	59	–0.022	–0.01	–0.01	0.00	0.00
SSC	59	–0.027	–0.01	–0.02	0.00	0.00
SSC+SA	59	–0.027	–0.01	–0.02	0.00	0.00
SSC+CA	59	–0.027	–0.01	–0.02	0.00	0.00
SSC+SA_CA	59	–0.027	–0.01	–0.02	0.00	0.00
FSC	59	–0.036	–0.01	–0.01	0.00	–0.02
FSC+SA	59	–0.036	–0.01	–0.01	0.00	–0.02

* Degradation at the real-time-combiner output (RTC) in the BC cases or the intermediate-frequency output (IF) in the non-BC cases.

Table 7-3(b). Magellan: one 70-m, one 34-m HEF, and one 34-m STD antenna array.

Arraying Scheme	P_T/N_o (dB-Hz)	Total Degradation (dB)	Carrier Degradation (dB)	Subcarrier Degradation (dB)	Symbol Degradation (dB)	RTC or IF* Degradation (dB)
BC	65	–0.015	–0.01	–0.01	0.00	0.00
BC+SA	65	–0.015	–0.01	–0.01	0.00	0.00
BC+CA	65	–0.015	–0.01	–0.01	0.00	0.00
BC+SA+CA	65	–0.015	–0.01	–0.01	0.00	0.00
SSC	65	–0.021	–0.01	–0.01	0.00	0.00
SSC+SA	65	–0.021	–0.01	–0.01	0.00	0.00
SSC+CA	65	–0.021	–0.01	–0.01	0.00	0.00
SSC+SA_CA	65	–0.021	–0.01	–0.01	0.00	0.00
FSC	65	–0.031	–0.01	–0.01	0.00	–0.02
FSC+SA	65	–0.031	–0.01	–0.01	0.00	–0.02

* Degradation at the real-time-combiner output (RTC) in the BC cases or the intermediate-frequency output (IF) in the non-BC cases.

7.2.4.1 Array of Two 70-Meter Antennas. The signal characteristics and receiver parameters are those given in Fig. 7-4, with a symbol rate of 400 sym/s. FSC performance for the Galileo scenario is obtained by adding 0.22 dB to the FSC degradation in Fig. 7-4. The shifted FSC curve along with the CSC degradation (which is the same as in Fig. 7-4, since no energy is lost in CSC) is plotted in Fig. 7-5. Notice that both techniques have equal performances when $B_{sc}w_{sc} = B_{sy}w_{sy} = 1.2$ mHz. In addition, Fig. 7-5 shows results using the same parameters as in Fig. 7-4, but now with a symbol rate of 200 sym/s (combined $E_s / N_0 = -5.0$ dB). In this case, FSC and CSC have equal performances when $B_{sc}w_{sc} = B_{sy}w_{sy} = 3.0$ mHz. The degradations due to individual components (carrier, subcarrier, symbol, and correlator) are discussed in the following paragraph to show the relative contribution of each to the total degradation shown in Fig. 7-5 for a symbol rate of 400 sym/s.

The degradation due to any single synchronization step is defined as the degradation that would be observed when all other synchronization steps are operating ideally. For example, in FSC, the degradation due to the carrier loop is given as $D_{fsc} = 10 \log_{10} \overline{C_c^2}$, which is derived by setting the combiner SNR, the subcarrier loop SNR, and the symbol-loop SNR to infinity in Eq. (6.1-47). The degradations due to individual components are shown in Figs. 7-6 through 7-9. The combiner degradation for both schemes is negligible. Also, the carrier degradation is the same for FSC and CSC since the carrier-loop SNR for both schemes is the same. The subcarrier degradation and symbol

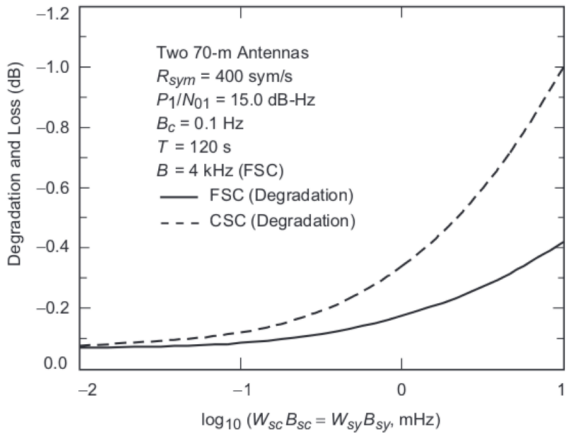

Fig. 7-4. Degradation versus subcarrier and symbol window-loop bandwidth.

degradation, however, are significantly different for FSC and CSC, the degradation from the latter being greater than FSC due to the carrier not being tracked and the signal not being combined until after the subcarrier and symbol loops.

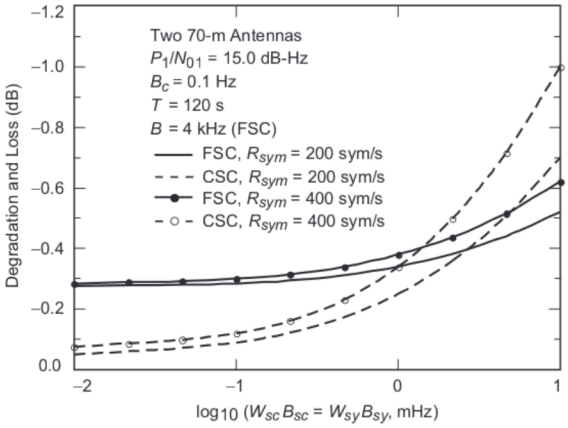

Fig. 7-5. Practical FSC and CSC degradation versus subcarrier and symbol window-loop bandwidth.

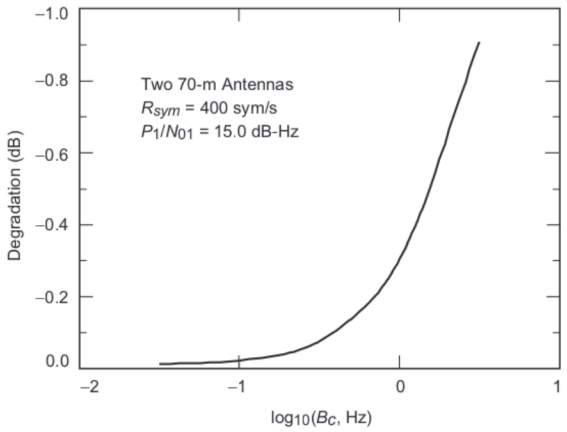

Fig. 7-6. Comparison of degradation due to individual components: carrier degradation versus carrier bandwidth.

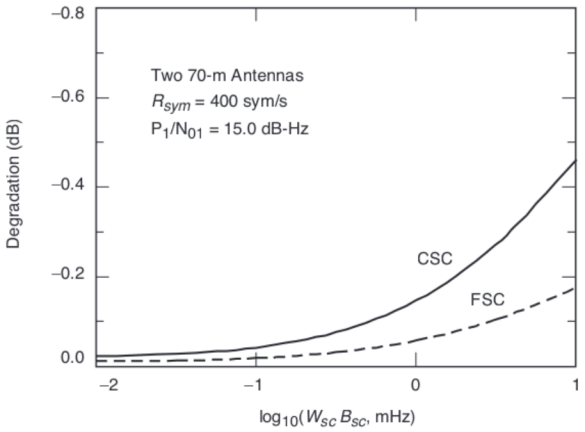

Fig. 7-7. Comparison of degradation due to individual components: subcarrier degradation versus subcarrier window-loop bandwidth.

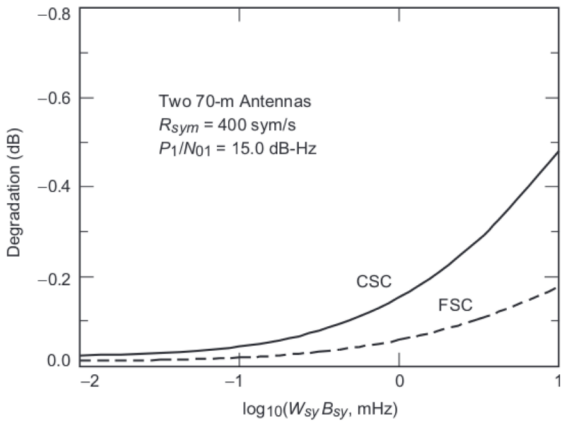

Fig. 7-8. Comparison of degradation due to individual components: symbol degradation versus symbol window-loop bandwidth.

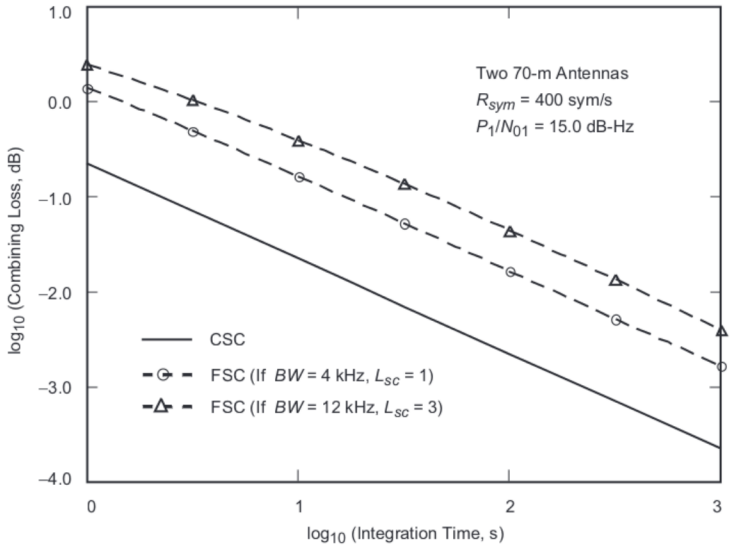

Fig. 7-9. Comparison of degradation due to individual components: combining loss versus integration time.

7.2.4.2 Array of One 70-Meter Antenna and One 34-Meter STD Antenna. The performance of one 70-m antenna and one 34-m STD antenna array is shown in Fig. 7-10, with P_1 / N_{01}= 15 dB-Hz and P_2 / N_{02}= 7.3 dB-Hz, i.e., $\gamma_1 = 1$ and $\gamma_2 = 0.17$. Figure 7-10 also shows the results when the symbol rate is 200 sym/s. At these signal levels, the 34-m antenna is not expected to achieve subcarrier and symbol lock without being aided by the 70-m antenna. Consequently, the CSC arraying scheme is implemented by passing frequency and phase information from the 70-m antenna to the 34-m antenna. As a result, the effective subcarrier- and symbol-loop SNRs of the 34-m antenna are identical to those of the 70-m antenna. The modified CSC is called complex-symbol combining with aiding (CSCA). In this scenario, the practical FSC outperforms CSCA when $B_{sc}w_{sc} = B_{sy}w_{sy}$ is greater than 4.5 mHz at a symbol rate of 400 sym/s and 10.0 mHz at a symbol rate of 200 sym/s.

7.2.4.3 Array of One 70-Meter Antenna and Two 34-Meter STD Antennas. The result for an array of one 70-m antenna and two 34-m antennas is shown in Fig. 7-11. For this case, FSC outperforms CSCA when $B_{sc}w_{sc} = B_{sy}w_{sy}$ is greater than 4.0 mHz at a symbol rate of 400 sym/s and 8.5 mHz at a symbol rate of 200 sym/s.

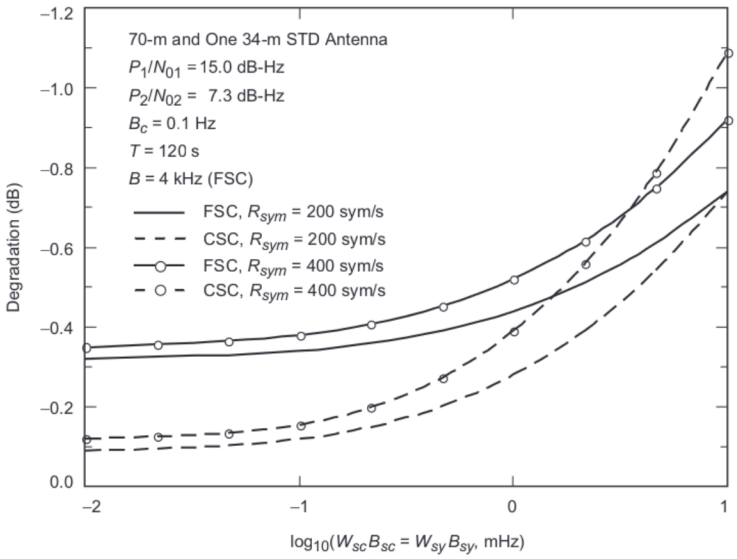

Fig. 7-10. Comparison of degradation for various array configurations: one 70-m antenna and one 34-m STD antenna.

7.2.4.4 Array of One 70-Meter Antenna and Three 34-Meter STD Antennas. The result for an array of one 70-m antenna and three 34-m antennas is shown in Fig. 7-12. FSC outperforms CSCA when $B_{sc}w_{sc} = B_{sy}w_{sy}$ is greater than 3.5 mHz at a symbol rate of 400 sym/s and 8.2 mHz at a symbol rate of 200 sym/s.

7.2.4.5 Array of Four 34-Meter STD Antennas. The result for an array of four 34-m antennas is shown in Fig. 7-13 for a symbol rate of 50 sym/s with a correlator bandwidth of 400 Hz. For this array, FSC has less degradation than does CSC when $B_{sc}w_{sc} = B_{sy}w_{sy}$ is above 0.32 mHz. Practical FSC is able to operate for the given $B_{sc}w_{sc} = B_{sy}w_{sy}$ without losing lock (assume the loops are able to lock to the signal if their respective loop SNRs are greater than 12 dB). For CSC, however, the maximum $B_{sc}w_{sc} = B_{sy}w_{sy}$ that can be supported without losing lock is about 0.9 mHz.

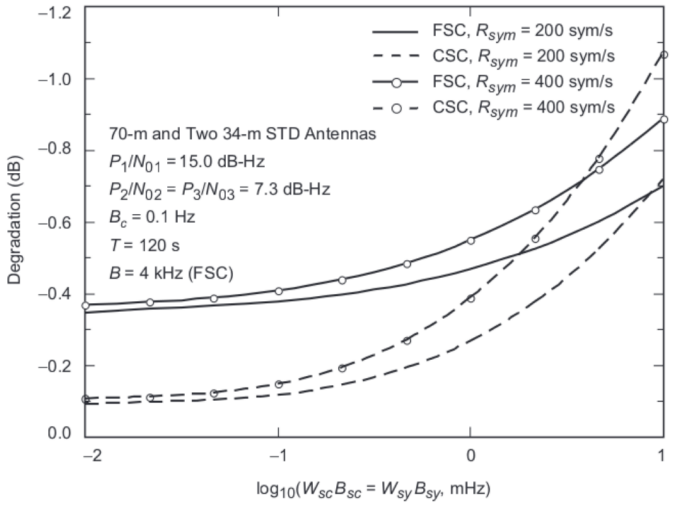

Fig. 7-11. Comparison of degradation for various array configurations: one 70-m and two 34-m STD antennas.

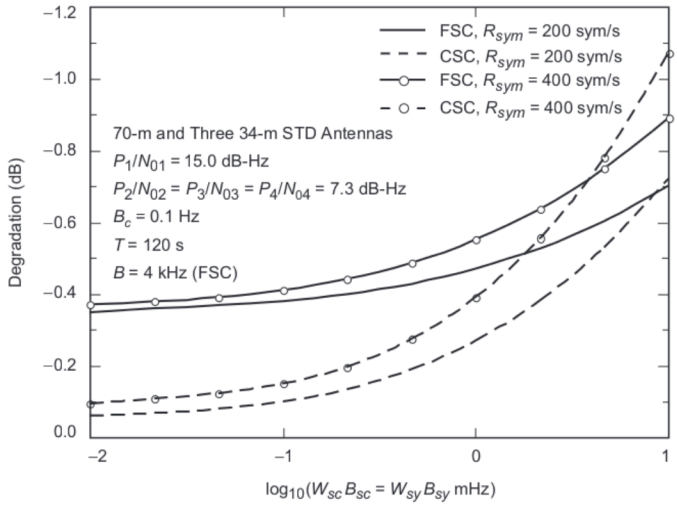

Fig. 7-12. Comparison of degradation for various array configurations: one 70-m and three 34-m STD antennas.

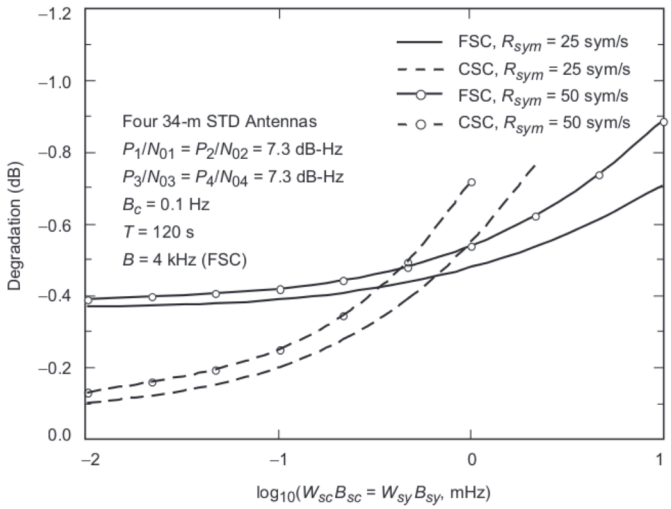

Fig. 7-13. Comparison of degradation for various array configurations: four 34-m STD antennas.

7.3 Conclusions

Five arraying schemes have been investigated—full-spectrum combining, complex-symbol combining, symbol-stream combining, baseband combining, and carrier arraying. For maximum telemetry performance, the best scheme is full-spectrum combining, which performs correlation at IF. After the signal combiner, it requires just one carrier, one subcarrier, and one symbol loop. The next in performance is the complex-symbol combining scheme, which requires L subcarrier and L symbol loops implemented as IQ-loops for maximum performance and just one carrier loop operating at baseband. About the same performance can be obtained with baseband combining augmented by carrier arraying. The simplest scheme to implement is symbol-stream combining, which requires L carrier, L subcarrier, and L symbol loops, but has poorer performance when compared with the previous schemes. It also has a drawback in that, at a low signal level, the carrier loops might not be able to lock on the signal. Of course, with sideband aiding, all these schemes receive an additional boost in performance.

Reference

[1] S. Million, B. Shah, and S. Hinedi, "A Comparison of Full-Spectrum and Complex-Symbol Combining Techniques for the Galileo S-Band Mission," *The Telecommunications and Data Acquisition Progress Report 42-116, October–December 1993*, Jet Propulsion Laboratory, Pasadena, California, pp. 128–162, February 15, 1994. http://ipnpr.jpl.nasa.gov/progress_report/

Chapter 8
Correlation Algorithms

There are several algorithms that possibly can be employed in those circumstances when correlation of signals is the method used to determine the phase and delay offsets between the array antennas (FSC, CSC, BA). If the SNR of the signal from each antenna is high enough to obtain a strong correlation for all the antenna pairs, then no special processing is necessary, and the phase and delay offsets derived from the correlation can be used directly to align the signals. However, when the signal SNR from each antenna is low, usually some other approach is necessary to take advantage of all possible antenna pairs. In this chapter, we discuss several approaches that have been analyzed and implemented with the arrays used in the DSN, including some discussion of their relative merits.

8.1 General

The output of an array is a weighted sum of the input signals applied to the combiner, where each of these input signals comes from the various antennas in the array. Here we assume that the input signals to the combiner have been corrected using predicts so that the residual delay and phase between the signals are slowly varying. The complex weights, providing corrections for both the amplitude and phase of the signals, can be derived in a number of ways from the cross-correlation matrices of the signal plus noise and of the noise itself. These matrices are derived by summing each combiner input over a symbol length, multiplying the sums from each pair of antennas, and accumulating long enough to obtain an adequately high signal-to-noise ratio. An array of L antennas will yield an $L \times L$ hermitian matrix of correlation components. The length of time over which the elements of the matrices can be accumulated is limited mostly by phase variations in the input signals caused by the

troposphere (instrumental phase variations usually are much smaller). A noise cross-correlation matrix can be obtained by moving off the signal source either spatially (for broadband sources) or spectrally (for narrowband sources such as spacecraft). In general, the amplitude of the weights is proportional to the input signal voltage divided by its variance, which takes into account both the signal-to-noise ratio and gain of the signals [1].

In an actual implementation, the delay and phase corrections are applied to the antenna signals before correlation in the form of a locking loop for each of these parameters. The purpose of the loops is to drive the delay and phase residuals to zero. Since delay is expected to vary much more slowly compared to phase, the order of the delay loop is smaller and its bandwidth is narrower. The phase-locked loop is second order and typically uses a 0.1-Hz bandwidth (10-s integration). The delay-locked loop is first order and typically uses a 0.01-Hz bandwidth (100-s integration). In addition, a history of the delay residuals is accumulated and used in such a way as to allow even narrower effective bandwidths (longer integrations) for this loop, permitting the delay residuals to be even more well-determined.

8.2 Simple

The Simple algorithm is diagramed in Fig. 8-1. One of the antennas in an array of L elements is designated as the reference antenna. This usually is the antenna with the largest G/T, although this is not an absolute requirement. Since the reference antenna becomes the phase center for the array, one may have reason to choose another antenna for this role. The signal from each of the remaining $(L - 1)$ antennas is then correlated with the signal from this reference antenna to yield $(L - 1)$ complex correlation amplitudes. This corresponds to one row of the correlation matrix mentioned above and is simple to implement since the amount of processing needed is proportional to the number of antennas. These complex amplitudes are used to correct the individual antenna signals to bring them into phase and delay coherence with the reference antenna signal. The resulting L signals then can be added to give an improvement in SNR. The improvement will depend on how well the corrected signals line up in phase. Limitation on the accuracy of the correction phases is determined by the averaging time that can be used in obtaining the correlation amplitudes. As mentioned above, this averaging time is largely restricted by phase variations in the antenna signals due to their passing through the troposphere

8.3 Sumple

The Sumple method is diagramed in Fig. 8-2. It can be described as the cross-correlation of each antenna with a reference antenna composed of the weighted sum of all the other antennas. It is an iterative method and can be used

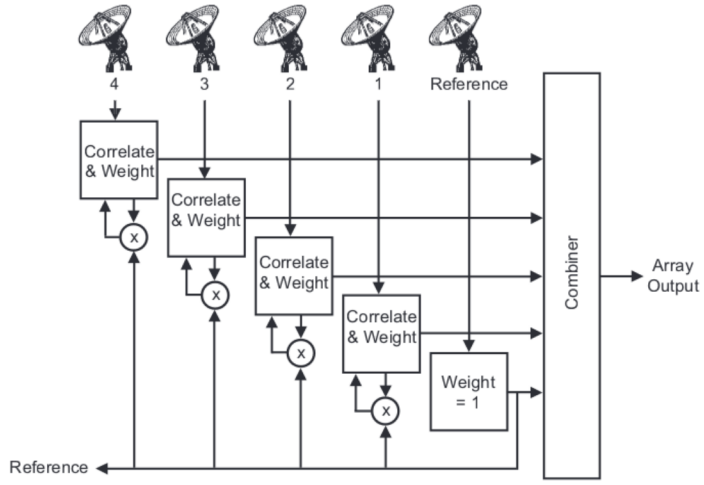

Fig. 8-1. Diagram for the Simple method of combining.

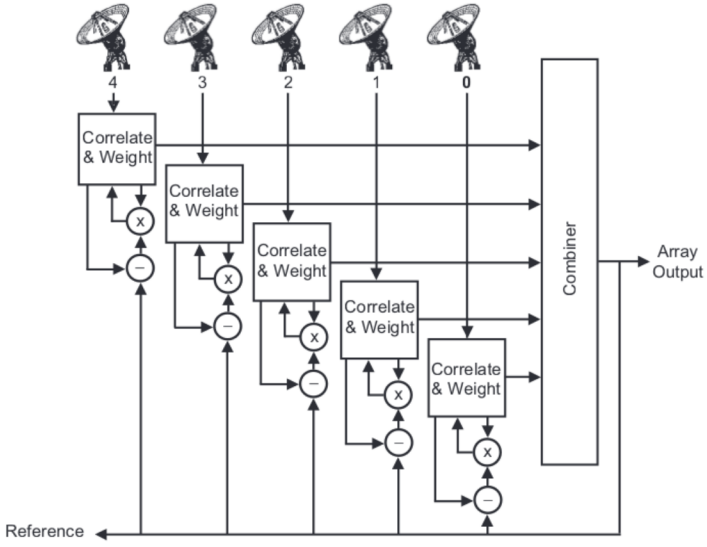

Fig. 8-2. Diagram for the Sumple method of combining.

for weaker signals than can the Simple method. The processing required is more complicated than the Simple method, but it is still proportional to the number of antennas. A single iteration is accomplished by rotating through each of the L antennas, correlating it with the complex weighted sum of the remaining antennas. The weights begin as unit vectors of zero phase. After each iteration, the previous weights are replaced with the new weights, and the process is repeated. The method appears to always converge from a random state in a few iterations (between 4 and 8), primarily because the weighted sum of all the antennas (minus one) is nearly a constant vector (albeit initially of small amplitude for a large numbers of antennas). Unlike the Simple method, the various antennas are not brought into alignment with a single reference antenna, but instead line up to a kind of floating reference. Simulations suggest the phase wandering of this reference is larger at lower SNR, but never becomes much more than a fraction of a cycle per hour, somewhat smaller than other sources of phase instability.

8.4 Eigen

The Eigen method of deriving the complex weights is given in [2] and uses both the signal matrix and the noise matrix mentioned above. It appears to be very general. The amount of processing required is proportional to the number of antennas squared, but the method does take into account off-diagonal noise coming from, for example, a background planet. In this case, the complex weights will maximize the SNR of the combined signal by a blend of aligning the phases of the desired signals and de-aligning the phases of the interfering signal (the planet).

8.5 Least-Squares

The Least-Squares method takes advantage of the fact that for an array of N antennas there are only $N - 1$ unknown relative phases and $N\,(N - 1)/2$ independent measurements in the correlation matix. The $N - 1$ phases are adjusted using an iterative procedure to minimize the difference between the predicted and measured cross-correlation matrices. Like the Eigen method, the processing is proportional to the square of the number of antennas.

8.6 Simulations

While only the Simple and Sumple algorithms were actually implemented in the 34-m arraying system, all four methods were simulated in a general-purpose computer. Of greatest interest is their performance at low SNR with various numbers of antennas. Figure 8-3 gives some of the results. As can be seen from the diagram, all give similar losses when the loop integration time is long. For short integration times, the Sumple algorithm performs best, but is

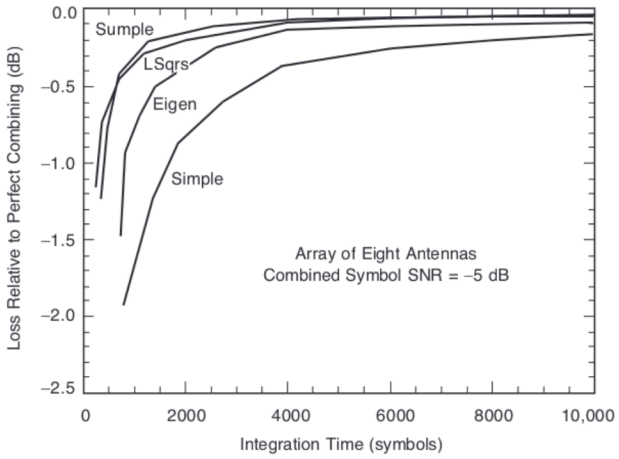

Fig. 8-3. Simulation of combining loss verses loop integration time.

very similar to the Least-Squares method. What is surprising is that Sumple is better than Eigen, even though it also uses all of the correlation pairs. One guess as to the reason for this difference in performance is that Eigen, being more general, is less constrained and therefore more sensitive to noise.

References

[1] V. Vilnrotter and E. R. Rodemich, "Real-Time Combining of Residual Carrier Array Signals Using ML Weight Estimates," *IEEE Trans. Comm.*, vol. COM-40, no. 3, pp. 604–615, March 1992.

[2] K .-M. Cheung, "Eigen Theory for Optimal Signal Combining: A Unified Approach," *The Telecommunications and Data Acquisition Progress Report 42-126, April–June 1996*, Jet Propulsion Laboratory, Pasadena, California, pp. 1–9, August 15, 1996.

http://ipnpr.jpl.nasa.gov/progress_report/

Chapter 9
Current Arraying Capabilities

Arraying has been utilized in the DSN a number of times over the past several years. The Voyager Mission relied on arraying to increase its data return during Uranus encounter in 1986 and Neptune encounter in 1989 [1,2]. More recently, the Galileo Mission also benefited from arraying to significantly increase the science data return in the face of the failure of the spacecraft's main communications antenna. Galileo arraying employed up to five antennas, located at three different tracking facilities and spread over the two continents of North America and Australia. Arraying alone resulted in a factor of 3 improvement in data return. [3– 5]

While baseband arraying was used in the earlier missions, full-spectrum arraying was employed for the first time in the DSN during the Galileo Mission. The Galileo arraying equipment, however, was tailored to low data rates (below 1 ksym/s). More recently, a new capability has been implemented that extends the supported data rate for full-spectrum arraying to 6 Msym/s. Unfortunately, because of the high transmission bandwidth between the antennas required to sustain these high data rates, the array is limited to those antennas within a tracking complex, i.e., no intercomplex arraying across two continents is supported. It is this implementation of arraying in the DSN, referred to as the array portion of the Full Spectrum Processing Subsystem (FSPS)—or the Full Spectrum Processing Array (FSPA)—that is described below. This subsystem is expected to provide arraying capability for the DSN in the future. While the FSPA is nominally intended for 34-m antennas, it is capable of arraying any size of antenna, including combinations of 70-m and 34-m antennas, up to 6 antennas (expandable up to a maximum of 8 antennas). The original subsystem was implemented only at the Goldstone Complex. It will be available for arraying up to 4 antennas (again, expandable up to

8 antennas) at the end of 2003 at the overseas complexes (Madrid, Spain, and Canberra, Australia).

9.1 Equipment Description

Signal processing for full-spectrum arraying is accomplished in two main assemblies—the Full Spectrum Receiver (FSR) and the Full Spectrum Combiner (FSC; this acronym has previously been used to mean full-spectrum combining, but here is used to mean a particular piece of equipment, the Full Spectrum Combiner), pictured as two equipment racks in Fig. 9-1. The FSR inputs are individual 300-MHz intermediate frequency (IF) analog signals derived from the radio frequency (RF) signals that have been received by the antenna, amplified by low-noise front-end microwave equipment, and downconverted in frequency by an RF-to-IF downconverter. The FSR outputs are digitally sampled bands of 16-Msamples/s data. Once digitally combined by the FSC, the signal is converted back to analog form and upconverted to an intermediate frequency near to the original 300-MHz IF. Except for having an improved SNR, the signal is, in principle, identical to the signal that arrives at the particular array antenna designated as the reference. Downstream processing, such as demodulation, decoding, and range detection, then can be accomplished on this combined output to yield final science and engineering data products.

Fig. 9-1. FSPA signal processing equipment: the FSR on the left, and the FSC on the right.

Major components of the FSR are illustrated in Fig. 9-2. The analog-to-digital converter (A/D) and the digital downconverter capture a relevant portion of the 300-MHz IF analog signal in a 16-MHz band that is preserved as 8-bit sampled, in-phase (I) and quadrature-phase (Q) digital data streams. The delay line and phase rotator modules correct signal delay and phase using information from predicts together with feedback from the FSC-derived residuals. The signal monitor module samples the digital data streams and transforms them into measurements of carrier- and telemetry-signal SNRs. These values are transmitted to the operators for monitoring. They also are relayed to the FSC for proper setting of the combining coefficients. Measurement of the carrier-signal SNR is obtainable directly from the square of the standard Fourier transform of this signal. Measurement of the telemetry-signal SNR, however, requires some manipulation involving the correlation of the upper and lower harmonics of the telemetry subcarrier signals. The real-time and data processors handle high-level monitor and control in the FSR.

Figure 9-3 presents the major components of the FSC. The cross-correlation of upper and lower sideband signals of different antennas is used to derive differential phase and delay values for feedback to the FSRs. At the same time, the weight and sum module combines the weighted FSC input signals to produce optimal output. The digital-to-analog converter (D/A) and upconverter module performs the conversion of the digital baseband stream back to an analog 300-MHz IF. The signal monitor module as well as the real-time and data processors carry out functions similar to those in the FSR.

9.2 Signal Processing

This section will highlight some aspects of the signal processing used in the FSPA. The main focus is on correlation, delay compensation, and combining.

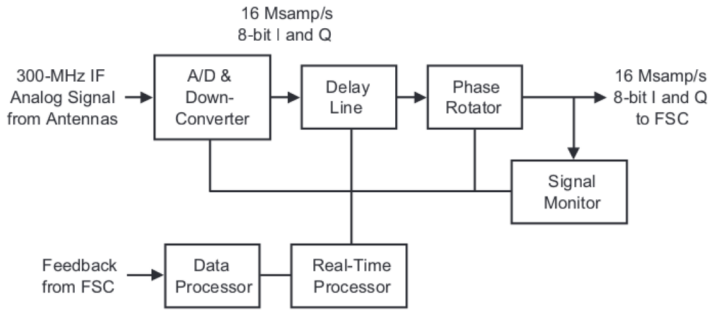

Fig. 9-2. Processing components in the FSR.

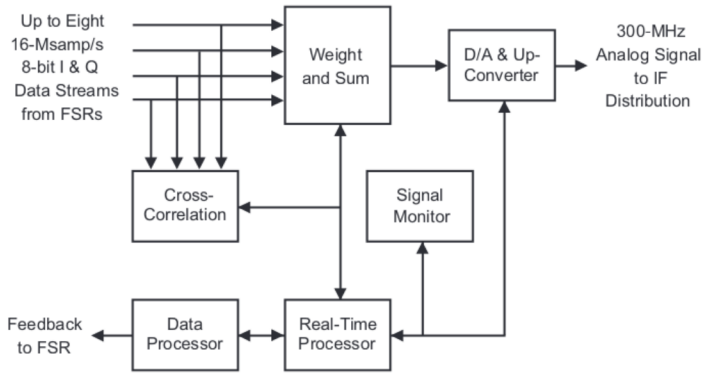

Fig. 9-3. Processing components in the FSC.

9.2.1 Correlation

The success of combining depends on good correlation results. Correlation is an essential process without which proper combining cannot be done. Figure 9-4 shows the accepted placement of filters relative to the type of signal received in order to extract the best phase and delay information. In the broadband case, it is possible to place the filters further apart if better delay precision is desired, provided that phase ambiguity is not a problem.

Figure 9-5 shows the details of the correlation processing [6]. With the aid of Doppler predicts, the upper and lower sidebands of the telemetry signal received at each antenna are captured in the FSR digital data streams. The upper sideband from one antenna then is correlated with the same component of the telemetry in the array reference antenna, from which the phase difference at the upper sideband is measured. The same process is performed simultaneously on the lower sideband signal component. As diagrammed in Fig. 9-6, an average of these two phase measurements then yields the phase offset, while the ratio of their difference to twice the sideband frequency provides the time delay.

As described in Chapter 8, there are different ways of implementing the correlation process. The FSPA equipment supports two approaches, both successfully tested. The simpler scheme (not surprisingly called Simple) involves choosing the antenna having the highest SNR as the reference, against which all other antenna signals are correlated. This scheme has been shown to work well when one element of the array has a significantly higher SNR than the others, as in the case of arraying the 70-m with one or more 34-m antennas.

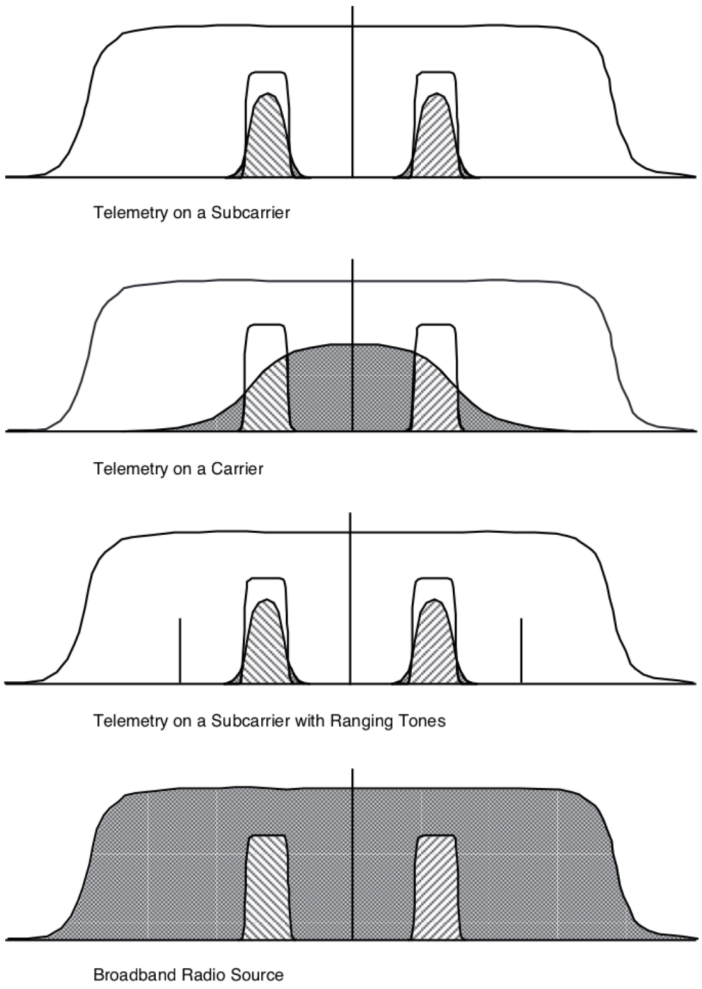

Fig. 9-4. Placement of filters for correlation of different signals.

The second method (called Sumple) treats as the reference a rotating sum of all antenna signals except the one under consideration. In other words, one antenna signal will be correlated against the sum of all the others. Simulation results presented in Chapter 8 indicate that the rotating sum method performs better

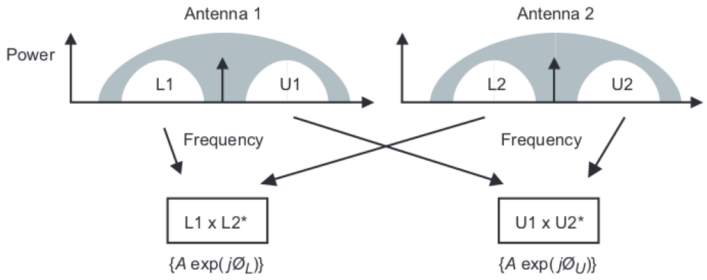

Fig. 9-5. Correlation processing.

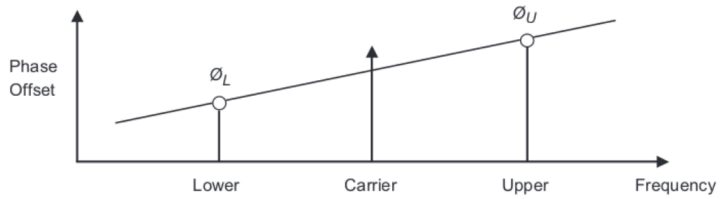

Phase Error = $(Ø_U + Ø_L) / 2$

Delay Error ~= $(Ø_U - Ø_L) / (2 \times \text{Sideband Frequency})$

Fig. 9-6. Derivation of phase and delay errors.

than the fixed-reference method at a low SNR, and that the final solution emerges within a few iterations (see Fig. 8-3) [7]. The simulations also included a third approach using the Eigen value method [8] and a fourth approach, referred to as the Root-Mean-Square method. However, neither of these two algorithms was implemented in the FSC.

Consideration must be given to setting the optimum integration or averaging time in the correlation process. Based on thermal noise considerations, a long integration period is preferred since it would yield a phase estimate with small error. Obviously, the lower the signal level, the longer the integration time must be to achieve a given phase error. The problem, however, is that signals received at different antennas travel through different portions of the Earth's troposphere and, consequently, are subjected to varying delay. These tropospheric delays vary on a relatively short timescale, resulting in a deterioration of correlation for long integrations. An illustration is provided in Fig. 9-7 for a fixed combined symbol SNR at –5 dB/Hz, with equal aperture antennas separated by a baseline of 1 to 10 km [9,10]. At X-band, the

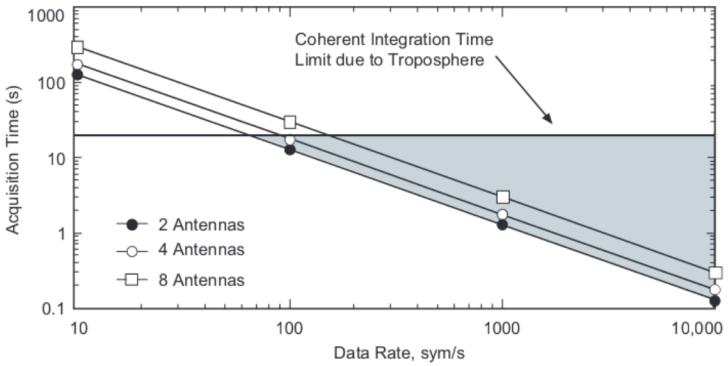

Fig. 9-7. Limits of correlation integration time.

tropospheric limit for a 20-deg phase-correlation error is about 20 seconds. The shaded triangular area is the operating region bounded by two constraints—thermal and tropospheric noise. Note also that the graph is expressed in terms of symbol rate, rather than in received SNR. Given a fixed symbol SNR, these two quantities are equivalent.

Care also must be taken in the use of correlation measurements to drive a feedback system. Invalid correlation results arise when one or both signals encounter problems. For example, one antenna could be mispointed or the spacecraft might go behind a planet. As in any control feedback system, it must deal with error signals that might drive the system away from a stable condition. Prevention of these types of problems can be achieved with appropriate filters on the FSC correlation estimates.

9.2.2 Delay Compensation

The delay compensation process is accomplished in two steps. In the first step, each FSR is provided with two sets of delay predicts—one for the various antennas being processed, the other for the reference antenna. These predicts have been computed (off-line, prior to the pass) from the spacecraft trajectory and the location of the tracking antennas. Using a model based on these predicts, the FSR removes a majority of the differential delay between any particular antenna and the reference antenna so that its signal can be aligned with the reference.

Over the course of an observing pass, the relative positions of different antennas in the array change with respect to the spacecraft. The delay of the non-reference signal varies relative to that of the reference. The relative delay is corrected by adjusting the physical delay line in the non-reference FSRs. Since such an adjustment is possible only with positive values, a delay bias is

introduced into all antennas. The bias typically is set at a value at least equal to the maximum delay among the arrayed antennas. Later it is compensated for in the follow-on telemetry and radio metric processing by making proper adjustment of the Earth-received time tags of telemetry, Doppler, and ranging data.

In order to arrive at the correct determination of relative delay between two antennas, both sideband and carrier information are important. The reason is due to the 2π ambiguity in the phase difference from upper and lower sidebands. The sideband measurement alone can only point to a set of possible delays of modulo $1/(2*f_{sb})$, where f_{sb} is the sideband frequency. Among these values, only the true delay yields a stable correlation phase at the carrier frequency. All others will result in the carrier phase being monotonically increased or decreased, in modulo of 2π. Unfortunately, since the FSC does not perform carrier correlation, it relies on having delay residuals that fall within the 2π ambiguity error. The gross relative delays of the antennas in the system must be measured beforehand and stored in a table to serve as the beginning point for any observing pass. This table must be updated when any system configuration change is made that would affect these delays.

9.2.3 Combining

Combining is done in a straightforward way. The 16-MHz samples from different FSRs are weighted according to their relative SNRs. These weights can be determined by measurement of the SNRs derived at each antenna or by an analysis of the actual correlation results. The FSC presently uses the first method. The system allows for disabling certain inputs when a signal is not detected, so that the noncontributing elements will not degrade the gain performance.

9.3 Results

Results of field demonstrations at Goldstone with missions currently in flight are discussed in this section. Emphasis is placed on the array gain for telemetry and radio metric data.

9.3.1 Telemetry Array Gain

Figure 9-8 shows the measurements of individual data SNRs (P_d/N_o) at each of the two Goldstone 34-m antennas and at the combined signal during one of the 1998 Mars Climate Orbiter cruise tracks in July 1999. The profiles vary as a function of time because of the changing elevation. An average array gain of 2.9 ± 0.2 dB was observed, as compared to a 3.0-dB theoretical improvement. The 0.1-dB difference is attributed to error in the correlation in the presence of noise as well as to signal-processing loss in the hardware.

Laboratory measurement with calibrated test signals puts an upper limit of SNR degradation, as caused by hardware, within 0.2 dB.

Figure 9-9 presents results from an array of maximum configuration. It employs all operational antennas available for X-band deep-space support at Goldstone. The track was conducted with the Saturn-bound Cassini spacecraft in August 1999. Relative to the performance of the 70-m antenna, the array yielded a gain of 1.8 ± 0.6 dB. Theoretical improvement would have been 2.0 dB.

An additional test experiment was conducted in February 2002 using three 34-m antennas at Goldstone, also observing the Cassini spacecraft at X-band. Figure 9-10 presents the results of this array. Relative to the performance of Deep Space Station (DSS) 24, which was used as the reference, the array yielded a gain of 6.0 ± 0.3 dB. Theoretical improvement would have been 5.9 dB. Figure 9-11 shows the phase corrections that were applied during this experiment to DSS 15 and DSS 25 to bring them into alignment with DSS 24. The remarkably low level of variation of this phase correction is undoubtedly due to the very good weather conditions that prevailed on this day. Typical phase variation is as much as 20 times what is seen here.

9.3.2 Radio Metric Array Gain

Ranging measurements also were obtained in July 1999, on a different track with Cassini using an array of two 34-m antennas. Surprisingly, the realized gain for ranging was not the same as for telemetry. A 1.6 ± 0.3 dB gain was

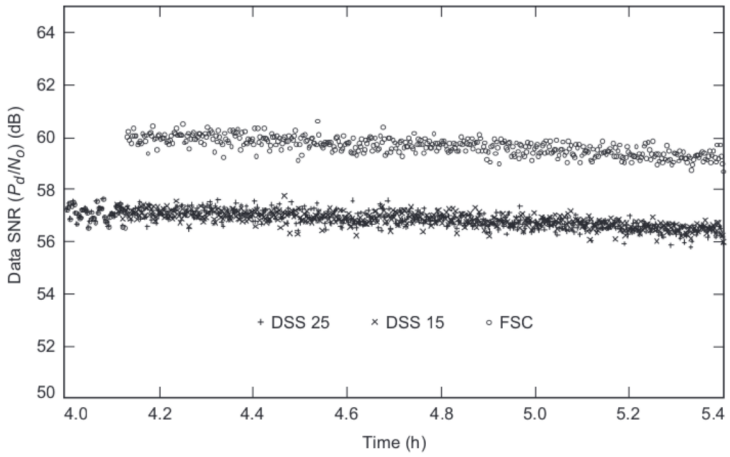

Fig. 9-8. Two-antenna arraying with 1998 Mars Climate Orbiter.

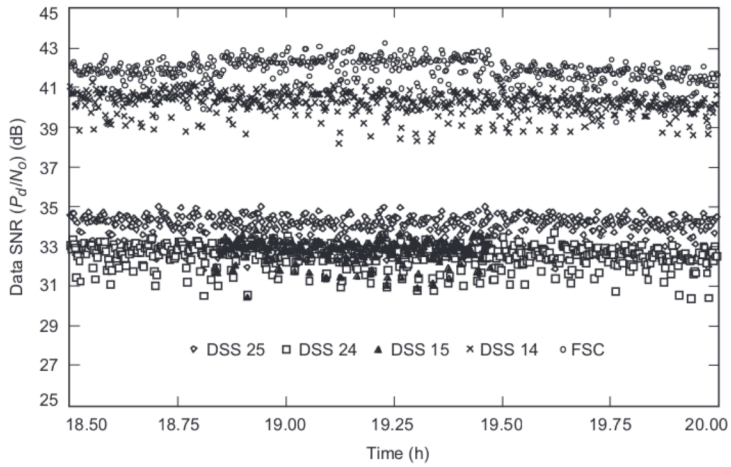

Fig. 9-9. Four-antenna arraying with Cassini.

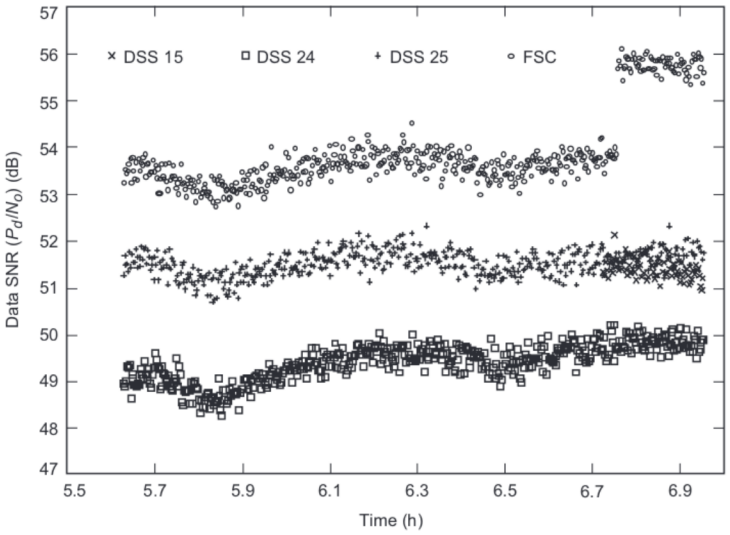

Fig. 9-10. Three-antenna arraying with Cassini.

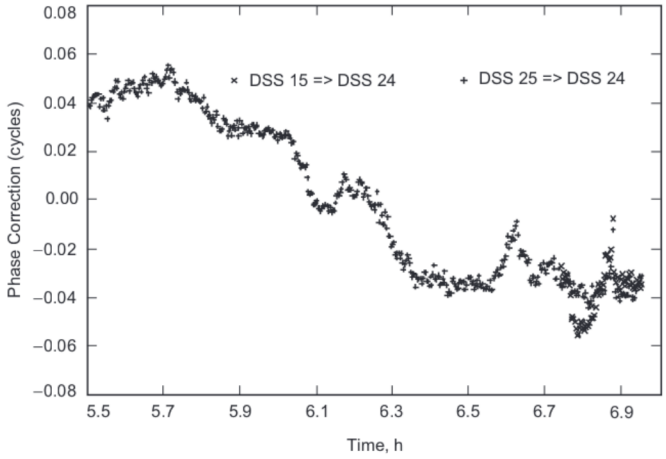

Fig. 9-11. Phase corrections for three-antenna arraying with Cassini.

measured relative to 2.4 dB predicted, which was confirmed by a measured 2.3-dB gain on telemetry. The most likely cause is the fact that the ranging component lies much further away in frequency from the carrier, as compared to the sideband component. In the presence of noise and ever-changing Doppler frequency, the error in the phase and delay estimation at the position of the 22-kHz sideband is magnified when extrapolated to the position of the 1-MHz ranging signal.

References

[1] D. W. Brown, H. W. Cooper, J. W. Armstrong, and S. S. Kent, "Parkes-CDSCC Telemetry Array: Equipment Design," *The Telecommunications and Data Acquisition Progress Report 42-85, January–March 1986*, Jet Propulsion Laboratory, Pasadena, California, pp. 85–110, May 15, 1986. http://ipnpr.jpl.nasa.gov/progress_report/

[2] D. W. Brown, W. D. Brundage, J. S. Ulvestad, S. S. Kent, and K. P. Bartos, "Interagency Telemetry Arraying for Voyager–Neptune Encounter," *The Telecommunications and Data Acquisition Progress Report 42-102, April–June 1990*, Jet Propulsion Laboratory, Pasadena, California, pp. 91–118, August 15, 1990.

http://ipnpr.jpl.nasa.gov/progress_report/

[3] J. W. Layland, F. D. McLaughlin, P. E. Beyer, D. J. Mudgway, D. W. Brown, R. W. Burt, R. J. Wallace, J. M. Ludwindki, B. D. Madsen, J. C. McKinney, N. Renzetti, and J. S. Ulvestad, "Galileo Array Study Team Report," *The Telecommunications and Data Acquisition Progress Report 42-103, July–September 1990*, Jet Propulsion Laboratory, Pasadena, California, pp. 161–169, November 15, 1990.
http://ipnpr.jpl.nasa.gov/progress_report/

[4] J. I. Statman, "Optimizing the Galileo Space Communication Link," *The Telecommunications and Data Acquisition Progress Report 42-116, October–December 1993*, Jet Propulsion Laboratory, Pasadena, California, pp. 114–120, February 15, 1994.
http://ipnpr.jpl.nasa.gov/progress_report/

[5] T. T. Pham, S. Shambayati, D. E. Hardi, and S. G. Finley, "Tracking the Galileo Spacecraft With the DSCC Galileo Telemetry Prototype," *The Telecommunications and Data Acquisition Progress Report 42-119, July–September 1994*, Jet Propulsion Laboratory, Pasadena, California, pp. 221–235, November 15, 1994.
http://ipnpr.jpl.nasa.gov/progress_report/

[6] Rogstad, D. H., "Suppressed Carrier Full-Spectrum Combining," *The Telecommunications and Data Acquisition Progress Report 42-107, July–September 1991*, Jet Propulsion Laboratory, Pasadena, California, pp. 12–20, November 15, 1991.
http://ipnpr.jpl.nasa.gov/progress_report/

[7] D. Fort, *Array Preliminary Design Review* (internal document), Jet Propulsion Laboratory, Pasadena, California, January 1998.

[8] K.-M. Cheung, "Eigen Theory for Optimal Signal Combining: A Unified Approach," *The Telecommunications and Data Acquisition Progress Report 42-126, April–June 1996*, Jet Propulsion Laboratory, Pasadena, California, pp. 1–9, August 15, 1996.
http://ipnpr.jpl.nasa.gov/progress_report/

[9] R. Kahn, *Array Preliminary Design Review* (internal document), Jet Propulsion Laboratory, Pasadena, California, January 1998.

[10] R. J. Dewey, "The Effects of Correlated Noise in Intra-Complex DSN Arrays for S-Band Galileo Telemetry Reception," *The Telecommunications and Data Acquisition Progress Report 42-111, July–September 1992*, Jet Propulsion Laboratory, Pasadena, California, pp. 129–152 November 15, 1992.
http://ipnpr.jpl.nasa.gov/progress_report/

Chapter 10
Future Development

This chapter provides a glimpse into the future development of array systems at JPL. Of particular interest is the ongoing effort within the DSN to build a prototype array having performance equivalent to several times that of a 70-m antenna. With proper funding, a system could be designed to expand and have an equivalent gain-to-noise-temperature ratio (G/T) of two orders of magnitude beyond the present 70-m antennas. Using such an aperture, data-intensive flight missions can achieve a significant increase in data return. Similar effort is being made by radio astronomers in building a Square Kilometer Array (SKA). Because of the synergy between this array and the DSN work, a description of the SKA development is provided below. Also discussed is possible development of an arrayed uplink capability that would increase the bandwidth in the forward link to the spacecraft. Such a capability is helpful in several scenarios: (1) establishing an uplink with a spacecraft that is in an emergency situation, (2) enabling a quick upload of special activities to a spacecraft when time is of the essence, and (3) supporting high-bandwidth communications with future astronauts. In addition, there is a potential need for the development of a software-based array system. Such a system offers unique advantages for mission scenarios in which it is important to extract, possibly post-pass, as much information as possible from a recorded signal.

The DSN is now at the crossroad of development. The systems in operation today trace their development back to the 1960s. The network started out with 26-m antennas, first operational in 1958. Over the course of time, antennas with increased aperture were added. The 34-m antenna subnet came, followed by the 64-m subnet in the early 1970s. In the late 1980s, the 64-m antennas were enlarged to 70-m. In the 1990s and early 2000s, additional 34-m antennas of beam-waveguide design were added to the network in response to an ever increasing demand for tracking resources. Along with the growth in aggregate

aperture, the DSN also achieved improved performance via a steady reduction in the operating system noise temperature, realized by better design of the low-noise amplifiers and antenna feeds. The improvement in G/T relative to the cost of development, however, has now reached a plateau. Although aggregate aperture can be increased by building more and more 34-m and 70-m antennas, the cost of antenna construction remains high. In the early 2000s, the nominal cost of bringing a new 34-m antenna into operation—including antenna construction, uplink/downlink electronics, and integration testing—runs close to U.S. $30M. Because the individual antenna aperture is ultimately limited, there is strong motivation to maximize the performance capabilities of each antenna, e.g., by furnishing it with an amplifier of the lowest possible noise temperature. This drive for the best performance contributes to an overall increase in development and operations cost.

To significantly improve the G/T performance, a paradigm shift is necessary. Two possible paths of growth have been identified in the DSN strategy planning. One is to migrate to optical communications systems. The performance advantage is realized through higher operating frequency. The second approach is to stay in the radio frequency (RF) domain and achieve greater gain by arraying a large number of small antennas. The small aperture of each array element promises a low development cost. The savings come from the maturity of commercial technology in manufacturing small, low-cost antennas. Also leveraged are recent advances in monolithic microwave integrated circuit (MMIC) technology used in building low-noise amplifiers, downconverters, and other electronic components. With the economy of scale in manufacturing, the overall electronic cost, despite the greater number of elements deployed, is expected to be small compared to the cost of building monolithic large-aperture antennas. It is this type of large-scale RF array that is explored in more detail below.

10.1 The Square Kilometer Array

Over the past few years, radio astronomers have developed several system concepts for a Square Kilometer Array (SKA). The SKA implementation is an international collaborative effort, with team membership including the United States, Canada, several European Union countries, Australia, China, and India.

As the name implies, SKA is a system with a front-end that will have an effective aperture of a million square meters. With such an aperture, the system will enable astronomical and astrophysical research with two orders of magnitude improvement over current capability. Among the study interests, as defined by the SKA Science Working Group, are

1) The structure and evolution of galaxies
2) The evolution of large-scale structure in the universe

3) The life cycle of stars, from formation through death
4) The formation and evolution of planetary systems
5) The formation of life

To enable such studies, the SKA system requires a high detection sensitivity (a G/T of 20,000 m^2K^{-1}), a wide frequency coverage (150 MHz to 20 GHz), a large field of view (1 deg^2 at 1.4 GHz), and high resolution (0.1 arcseconds). The detection sensitivity enables the capturing of extremely faint signals. The low-end frequency coverage helps the detection of HI in the high red-shift region, corresponding to the epoch of re-ionization. The high-end frequency coverage permits the study of thermal sources, like dust in a proto-planetary disk or CO emission from high red-shift galaxies. The large instantaneous field of view allows for an efficient survey of both HI line and broadband continuum emission. Table 10-1 lists preliminary specifications for the SKA system [1].

Various systems utilizing different technologies are being proposed by different members of the SKA consortium. Some designs rely on parabolic antennas whose size varies from 10 m (as in the U.S. and Indian proposals)

Table 10-1. Specifications of the SKA system.

Parameter	Design Goal
Aperture-to-noise temperature ratio, A_{eff}/T_{sys}	20,000 m^2/K
Total frequency range	0.3–20 GHz
Imaging field of view	1 sq. degree at 1.4 GHz
Number of instantaneous pencil beams	100
Maximum primary beam separation	
Low frequency	100 deg
High frequency	1 deg at 1.4 GHz
Number of spatial pixels	10^8
Angular resolution	0.1 arcsec at 1.4 GHz
Surface brightness sensitivity	1 K at 0.1 arcsec (continuum)
Instantaneous bandwidth	0.5 + ν/5 GHz
Number of spectral channels	10^4
Number of simultaneous frequency bands	2
Clean beam dynamic range	10^6
Polarization purity	–40 dB

to 200 m (as in the Canadian and Chinese proposals). The European proposal relies on phased array technology. The Australian team, on the other hand, is pushing the Luneburg lens concept. Detailed descriptions of each system are documented in [2]. Several prototype efforts at a smaller scale are under way to demonstrate the feasibility of each concept, e.g., the Allen Telescope Array (ATA) using parabolic antennas, and the Low Frequency Array (LOFAR) using phased array stations. Selection of the baseline SKA system is planned to occur in 2005.

10.2 The Allen Telescope Array

Among the many SKA prototype systems, the Allen Telescope Array (ATA), being built in Northern California by the University of California at Berkeley, is closest to the system being considered at JPL for the DSN. The ATA project aims at achieving an aggregate aperture of 100-m diameter from arraying 350 elements of 6.1-m dishes. The system is designed to operate over a frequency range of 500 MHz to 11.2 GHz. Figure 10-1 illustrates the main components in the ATA system [3].

Each antenna is equipped with offset-Gregorian optics and offers 56 percent antenna efficiency at 1 GHz. The feed is of log-periodic design, enabling a wide-bandwidth reception. The low-noise amplifier is cryogenically cooled to 60–80 K. The cooling system uses a Sterling cycle design, contains no contacting moving parts, and has an expected mean time between failures of one million hours! In the interest of minimizing the cost of development, operation, and maintenance, the antenna instrumentation is simplified as much

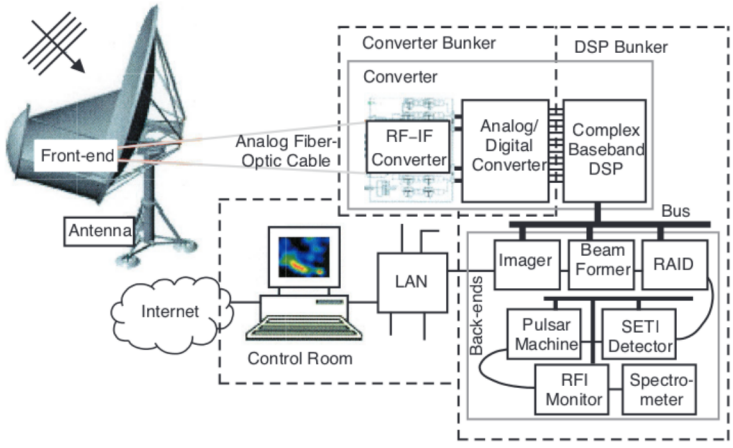

Fig. 10-1. Block diagram of the ATA system.

as possible. The received signals, after amplification, are routed to a central processing facility via analog fiber-optic links. All local oscillators and RF downconverters are housed in the central facility. This approach eliminates the need to distribute frequency and timing references of extreme stability to the antennas. For a system with many antenna elements, such a design can translate into significant cost savings. This scheme, however, relies on having high stability in the transporting fiber-optic network. Within the central processing facility, correlation is computed for all possible pairs of array elements. The ATA produces four simultaneous correlated beams, each with an instantaneous bandwidth of 100 MHz.

Since the overall frequency range of interest spans 11 GHz, and there are many commercial satellites currently operating within this band, radio frequency interference (RFI) demands special attention. The ATA design counteracts this problem by keeping track of the trajectories of these high-power satellites and adjusting the pointing of synthesized beams so that their nulls are in the direction of the interfering signals.

10.3 The DSN Large Array

A study is being conducted at JPL on the feasibility of deploying an array configuration consisting of hundreds of small antenna elements with sizes in the range of 6 m to 15 m in diameter. This configuration is similar to the SKA system proposed by the United States team. Justification for such a large aperture is based on the many different options that can be exercised by a planetary mission if such capacity exists. Figure 10-2 shows the data rate associated with many different options [4]. Data rates necessary to obtain images from planetary missions fall in the range of up to a few hundred kilobits per second (kb/s). For example, the current Mars Global Surveyor (MGS) mission uses approximately 30 kb/s. Scientific high-resolution synthetic radar and multi-spectral imaging data demand a much higher rate, typically in the 1–100 megabits per second (Mb/s) range. Such data cover many physical aspects of the object under study. Sampled data rates from deep-space probes (e.g., Magellan, Cassini) to near-Earth satellites (e.g., Terra with its onboard Advanced Spaceborne Thermal Emission and Reflection Radiometer (ASTER), Shuttle Radar Topography Mission (SRTM), and Spaceborne Imaging Radar at C-band (SIR-C)) are shown in the figure. Ultimately, streaming video or high-definition television (HDTV) data at 1–100 Mb/s would promote a sense of tele-presence for mission operations. Such capability would also increase the level of public engagement in space exploration.

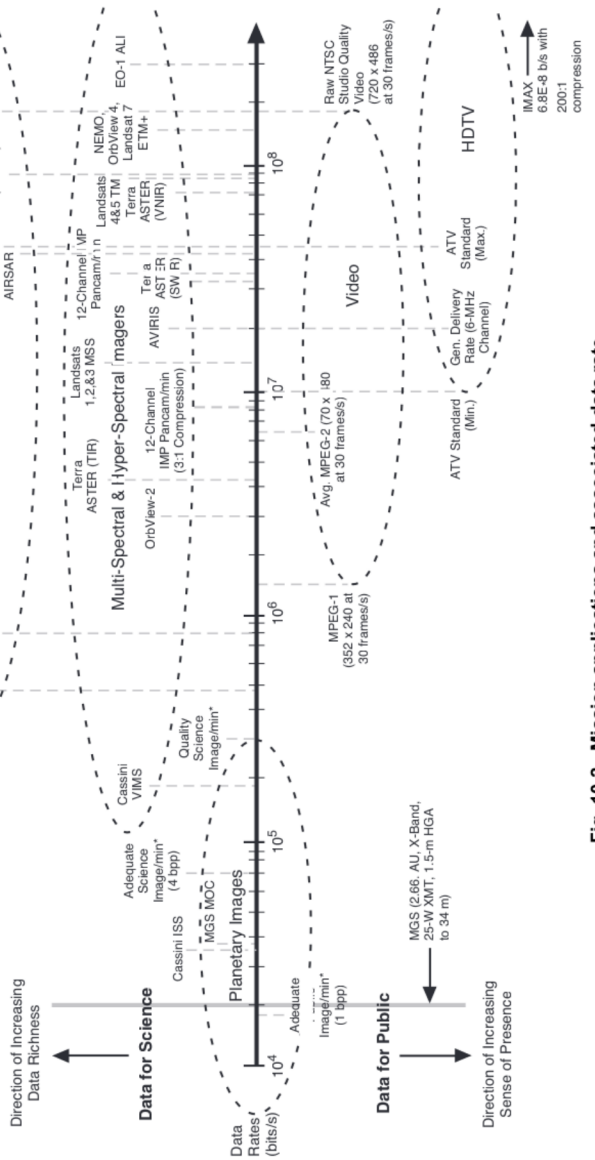

Fig. 10-2. Mission applications and associated data rate.

The DSN large array effort will begin with a prototype system that has an aggregate aperture of twice the 70-m antenna. The envisioned final system, to be completed over the next 10 to 15 years, may be 100 times as large, subject to funding availability. Despite the promise of low cost, there is still a high degree of uncertainty in such an implementation. Accordingly, the current prototype effort will help establish feasibility. From that experience, it is hoped the uncertainties in the life-cycle cost, from development to operation, can be narrowed. A better understanding of system performance, relative to flight mission support, will also be gained. DSN personnel will obtain the necessary experience with operation and maintenance of such a system. Preceding the prototype system will be the development of breadboard versions of a two- or three-element array using antennas similar to those of the ATA. The breadboard is intended for testing hardware and software components, developing integration and test procedures, and assessing signal processing and various monitor and control schemes.

The array is likely to be installed at multiple sites, probably in the Southwestern United States and at other overseas facilities. Such a deployment allows for a spatial diversity to counteract the impact of weather sensitivity at Ka-band (32 GHz). Large physical separation also allows for high-precision radio metric measurements using VLBI techniques such as delta differential one-way-ranging (delta DOR). Within a site, multiple sub-array configurations are possible. The system is being designed for operation at X-band (8.4 GHz) and Ka-band. Operation at the 37- to 38-GHz band, which is reserved for supporting future human deep-space exploration, is anticipated in the system design; however, equipment supporting such functions will not be implemented at this time due to the trade-off between implementation cost and need. Table 10-2 captures the essence of the current system specifications [5].

It is important to recognize that while there are synergy and commonality between systems that support radio-astronomy observations and those that support spacecraft communications, there are also significant differences. The differences translate to divergent design specifications for the two applications. One example is frequency coverage. Radio astronomy systems typically operate over a very wide spectrum to enable the study of different radio astronomical phenomena. In the case of the SKA project, this frequency coverage extends from 300 kHz to 20 GHz. In contrast, the signals from spacecraft are narrow-band sinusoidal, and they cluster within a narrow allocated frequency band of a few hundred MHz. Another difference is the layout of array elements. For imaging of a radio source, the log spiral configuration is deemed best in providing complete coverage in the spatial frequency plane. In spacecraft communications, it is more desirable for the site layout to produce a high-gain, narrow beam with small side lobes. Also, because of the importance of timely support to certain critical events in a mission's lifetime, getting important data at the right time is urgently important so that mission objectives are not

compromised. To support such operation, the system design must provide sufficient operational details to enable quick troubleshooting and replacement. This may imply a greater complexity in monitor and control design, and the operations facility may require higher levels of staffing. This translates to a preference for a more centrally located facility rather than dispersed remote facilities.

Figure 10-3 shows a conceptual design of such a system [6]. Received signals are captured at X-band and Ka-band, selectable for right- and left-circular polarization. The low-noise amplifiers are enclosed in a dewar to maximize the low-noise performance. The LNA expected performance, when cooled to 80 K, is about 15 K at X-band and 30 K at Ka-band. The

Table 10-2. Specifications of the DSN prototype system.

Parameter	Specifications
Processing function	Downlink only
Operating frequency range	8400–8620 MHz, S-band 31,800–32,300 MHz, Ka-band 37,000–38,000 MHz (goal, for future human exploration support)
Signal-processing channel bandwidth	>100 MHz
G/T_{sys}	>58.6 dB for all elevations, X-band >65.5 dB for all elevations, Ka-band
Tracking coverage	6–90 deg, elevation 0–360 deg, azimuth
Spectral purity	–65.7 dBc at 1 Hz offset from carrier –75.2 dBc at >100 Hz offset from carrier
Frequency stability	4.5×10^{-15} at 1000 s, X-band 1.4×10^{-15} at 1000 s, Ka-band
Gain stability	<0.2 dB variation across operating bandwidth
Polarization	Selectable TCP or LCP Simultaneous RCP and LCP (goal)
RCP/LCP isolation	>30 dB
Dynamic range	>55 dB
Number of synthesized beams	>2
Operability	Remotely operated from central control center Operable by a single operator Within 5%–7% of capital cost, per year

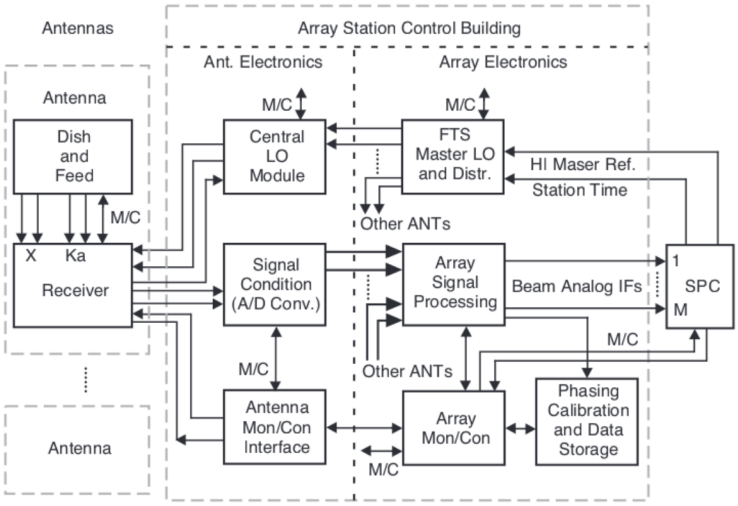

Fig. 10-3. Functional diagram of the DSN Large Array initiative.

RF signals are downconverted to the 0.5- to 1-GHz range and sent across the fiber-optic link to a central processing area. They are then digitized, filtered, and appropriately delayed to account for the difference in path delays. The signals then pass through a set of 1:16 beam splitters. A copy of each array element signal is correlated and then combined by one of the 16 beam formers that is part of the "backend" processing. Including 16 beam formers allows for expanded applications, more than enough to support the system requirements of 2 beams plus concurrent spacecraft tracking and quasar calibration. The beam splitter and beam former functions are implemented with FPGA chips. Figure 10-4 illustrates the proposed signal processing for arraying [7]. Once combined, the signal is routed to the existing DSN receiver and telemetry processor. The current DSN receiver was designed and built in the early 1990s. It supports a maximum data rate of 26 megasymbols per second (Msym/s). With the arrayed aperture, however, it is expected that higher data rates will be required in the support of future mission. Any such upgrade would have little impact on the array front-end because the interface between the two portions of the system is well defined and has minimum coupling

In addition to technical performance, the array design must also achieve maximum operability and minimum life-cycle cost. To optimize the solution against these constraints, careful consideration must be given to the overall system design. A few design aspects of interest are highlighted below.

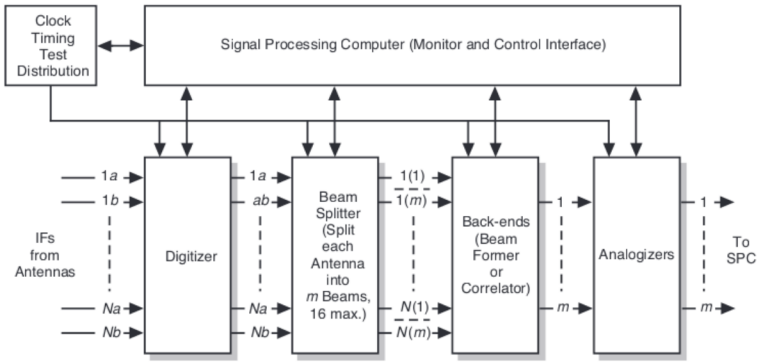

Fig. 10-4. Proposed scheme for signal processing for the DSN Large Array.

10.3.1 Correlation

The challenge is in performing the correlation on very faint received signals. In the interest of low electronic cost, it is expected that the system noise temperature at each array element will be higher than that achieved at the current 34-m and 70-m antennas. Coupled with the smaller aperture, the resulting SNR at each array element may be quite low. For example, to synthesize an equivalent 70-m aperture from a set of 12-m array elements, the signal received at each array element is at least 15 dB lower than at the combined aperture. Assuming a combined symbol SNR of –5 dB-Hz, the signal level at each array element would be less than –20 dB-Hz. For an array configuration to synthesize an aperture greater than a 70-m antenna, the input SNR at each array element becomes progressively smaller. Since the atmospheric fluctuation places a constraint on how long the signal can be coherently integrated, the task of correlating many inputs at an extremely low SNR is challenging. It is likely that techniques such as “Sumple,” described in Chapter 8, will be needed.

For a spacecraft signal that is too weak for correlation, a calibration method using other targets, such as natural radio sources, will be required. A fraction of the array elements can be devoted to tracking the calibration source. The relative delays among different signal paths caused by the Earth atmosphere then can be transferred to those antennas that are concurrently tracking the spacecraft.

10.3.2 Monitor and Control

As the array size grows, the number of elements to be monitored and controlled increases accordingly. The ability to detect a problem, to properly identify the element causing the problem, and to carry out corrective action is essential to making the array operational complexity transparent to operators. Another consideration is the amount of information to be monitored. Finding the right level of monitoring to enable the maintenance personnel to promptly restore system service is essential. The larger the size of the least replaceable elements, the simpler is the structure of the equipment monitor. However, the cost for replaceable hardware would be higher, as well as the time for repair of the replaceable element because of its increased complexity. Clearly, an optimal structure depends on the way a logical function is mapped onto hardware and the cost of a replacement element. If a logical function is distributed over several components, individual monitoring will be needed. If the hardware cost is low, a monitor on go/no-go status and an order of replacement is all that is needed, rather than having to monitor individual components within a replaceable element.

10.3.3 Signal Distribution

Within an array site, one has to be concerned with preserving the integrity of the frequency and timing references distributed to different array elements. The design choice can be modeled after the ATA by keeping the local oscillators at a central location, rather than at individual array antennas. The constraint is that the fiber-optic system that routes the RF signal to the central facility must operate at Ka-band. Today commercial fiber-optic transmission systems are not readily available at such frequencies. Thus, a trade has to be made concerning whether to push for a technology advance in a few years or to rely on the distribution of local oscillators to the antennas.

Synchronization of the timing reference between two array sites is also required to enable inter-site arraying. While various technical solutions exist for small-scale distribution networks, a design choice that minimizes the near-term implementation cost while offering maximum future scalability requires careful attention.

10.3.4 Maintenance

A large array involves a very large amount of electronics. This equipment, due to its heavy capital investment, is expected to operate over 20-plus years. Over this period, many electronic components will become obsolete, making it hard to build replacement units in later years. It is critical to maintain a sufficient amount of spares for hardware replacement throughout the system

operating life cycle. The hardware design, with its choice of parts, technology, etc., has to account for this maintenance consideration from the very beginning.

10.3.5 Data Routing

Today, the bandwidth of wide-area networks connecting the project users to DSN tracking stations is restricted to a few Mb/s. The connection relies on dedicated leased lines from telecommunication vendors. While such lines offer dedicated bandwidth and relatively high security, they are expensive. Also, such an approach will need a major upgrade for support of future array operations. Subscribing to more leased lines for the required high-rate interconnections among many array sites is not likely to be a cost-effective solution. The new design will need to consider other bandwidth-sharing infrastructure, such as the internet. Of course, desired features in data security and latency will have to be addressed as well.

10.4 The Uplink Array

In the current plan, the DSN array design effort only targets downlink processing. Support for uplink functions is being left to the existing 34-m and 70-m antennas. The lack of uplink capability within the array system poses several disadvantages, namely:

1) Dependency on the 34-m and 70-m antenna operation continues into the foreseeable future.
2) Spatial diversity against Ka-band weather is compromised. It is expected that, not too far into the future, deep-space mission operations will be moving toward full Ka-band uplink and downlink. Given that possibility, having command functionality at each array site is important to mitigate the weather impact. (Note that most present missions operate at X-band. New missions, such as Kepler, are beginning to include Ka-band downlink. However, X-band uplink and X-band downlink in an emergency situation are still expected in the near future.)
3) Two-way ranging measurements, wherein the transmitting and receiving stations are co-located, cannot be conducted, either at X-band or Ka-band. Two-way configuration offers better measurement accuracy than does three-way.
4) There is no extension to the equivalent isotrophic radiative power (EIRP) beyond the current capability. Such an extended capability is highly desirable in certain special operations, such as searching for a missing spacecraft. Even with regular tracking of a faraway spacecraft, such as Pioneer, a high-power uplink (100 kW at a 70-m antenna) is typically required.

It is clearly desirable that the uplink function be incorporated into the array system. However, if only one array element were to serve as the transmitting antenna for the entire array, its small aperture would require a high transmitting power to achieve the required EIRP received at the spacecraft. The required power increase is proportional to the ratio of the effective arrayed aperture and the physical aperture of a single element. For example, to maintain an equivalent radiating power of 20 kW on the 70-m antenna, 680 kW is needed on the 12-m antenna. Such a high-power transmitter poses a problem. Not only would it be more complex to build, it also would be more costly to operate. In addition, there is also the radiation safety issue. The radiating power in the near field would far exceed the 10 mW/cm^2 recommended safety level for radiation exposure at microwave frequencies for the operations crew on the ground and for any aircraft that might travel inside the air corridor of the beam.

Given these considerations, an arrayed uplink is deemed necessary in any final system. However, before the design can be accomplished, a solution must be obtained to the transmitter alignment problem. Since a spacecraft does not have the means to align the signals received from different transmitting antennas, the phasing for uplink signals must be done on the ground. Such alignment needs to account for instabilities caused by the uplink electronics as well as that caused by tropospheric variation, as described below.

10.4.1 Electronic Stability

The integration time required for a ranging measurement in a deep-space environment can be as long as 1000 seconds. The uplink electronics must be sufficiently stable over this time frame. This stability can be achieved with proper design of the electronic components or with proper compensation for the measured drift.

10.4.2 Tropospheric Variation

Two approaches can be used to compensate for tropospheric variation. The first is to use the measured variation obtained from downlink processing. Since it is the Earth's tropospheric effect that needs to be removed, as long as the latency in data processing is smaller than a typical 20-second time constant of tropospheric variation, the transfer of the correction factor from downlink to uplink is valid. Obviously, this option is constrained by the availability of a downlink signal. It also introduces an acquisition delay on the uplink path.

Another approach is to bounce a radar signal to a near-Earth orbital target and determine the tropospheric variation from the received echo. Such a scheme is described in [8] for two 34-meter antennas operated at 5-kW peak power. The drawback of this scheme, compared to the use of downlink information, is the requirement for additional radar signal processing

equipment. It also requires the calibration target to be in the proximity of the spacecraft.

10.5 Software Combiner

A case can also be made for developing a software combiner to be part of the array. Such a system was developed for the Galileo Mission; however, its capability was limited to low data rate, up to 1 ksym/s [9]. A high-rate software combiner, in the Mars range, would be desirable. Despite the support data rate being lower than the hardware-based real-time array system discussed earlier, the software combiner can offer certain advantages. For example,

1) Being software based, it can be modified to include new capability and new algorithms rather quickly.
2) In the context of special planetary events, e.g., encounter, entry/descent/ landing, wherein signal level is often a limiting factor, a software combiner can boost the chance of recovering precious information from recorded data at a later time. As an example, for the upcoming 2004 landing of the Mars Exploration Rovers (MERs), data recording at all 70-m and 34-m antennas within a tracking complex is being planned with the intention that they can be combined in post-pass to enhance signal detection.
3) In the context of the DSN large array effort, it can be used to combine signals from various array sites. Since the data can be transmitted via internet-type packets, it can relieve the need for having a point-to-point fiber-optic link between sites that would be required by a hardware-based system.

10.6 Final Remarks

In summary, there is clearly much activity with significant promise in the area of array development, both within the DSN and internationally under the SKA charter. Ongoing effort is being put into building prototype systems. Their presence will eventually lead to a larger version of a telemetry array with two orders of magnitude improvement over currently available aperture. The higher communication bandwidth offered by such a system will significantly increase tele-science and tele-presence in space exploration.

References

[1] U.S. Square Kilometer Array Consortium, The Square Kilometer Array, Preliminary Strawman Design Large N–Small D, July 2002.

[2] ASTRON, SKA Development, Technical Case, Dwingeloo, Netherlands, June 2002.

[3] D. DeBoer and J. Dreher, "A System Level Description of the ATA," ATA Memorandum no. 23, Radio Astronomy Laboratory, University of California, Berkeley, April 6, 2001.

[4] D. S, Abraham, "Identifying Future Mission Drivers on the Deep Space Network," SpaceOps 2002, October 9–12, 2002.

[5] M. Connally, "Prototype Array System Requirements," DSMS 828-042, D-24531, Jet Propulsion Laboratory, Pasadena, California, August 2002.

[6] D. S. Bagri, "Prototype Array System," *Array Technology—FY02 Progress Report*, Jet Propulsion Laboratory, Pasadena, California, September 17, 2002

[7] R. Navarro and D. Fort, "Signal Processing," *Array Technology—FY02 Progress Report*, Jet Propulsion Laboratory, Pasadena, California, September 17, 2002

[8] R. M. Dickinson, D. L. Losh, R. D. Barber, and J. K. Dempsey, "A Phase-Control Approach for a Large-Element Coherent Microwave Power Uplink System," *IEEE Transactions on Antennas and Propagation*, vol. 47, no. 3, 1999.

[9] T. T. Pham, S. Shambayati, D. E. Hardi, and S. G. Finley, "Tracking the Galileo Spacecraft with the DSCC Galileo Telemetry Prototype," *The Telecommunications and Data Acquisition Progress Report 42-119, July–September 1994*, Jet Propulsion Laboratory, Pasadena, California, pp. 221–235, November 15, 1994. http://ipnpr.jpl.nasa.gov/progress_report/

Appendix A
Antenna Location

One of the practical problems faced when trying to array antennas is that of providing good a priori information to the combiner. The definition of "good" depends on the technique, and, as was pointed out in Chapter 3, full-spectrum combining in general requires higher-accuracy a priori information.

A particularly important piece of information is the location of the antenna intersection of axes for each element of the array, expressed in a common coordinate system. This is required in order to calculate the difference in phase delay between all elements of the array. It can be a difficult quantity to determine because, in many parabolic antennas designs, the intersection of axes is buried in the middle of a steel shaft or casing, and its location can only be inferred. If the antenna is located inside of a radome, the problem may be even more complicated. In this appendix, a concept is outlined by which the location of the axes could be inferred with high accuracy.

Consider Fig. A-1, which shows a parabolic antenna located somewhere on the face of the Earth. It is assumed that a Global Positioning System (GPS)

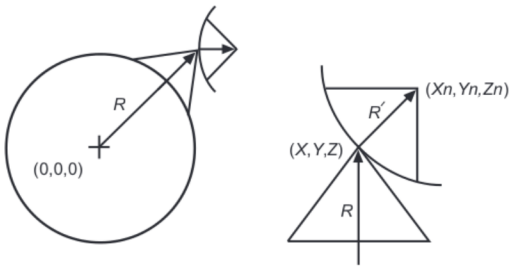

Fig. A-1. Diagram for visualizing the determination of the intersection of axes.

receiver can be placed on the backside of the antenna subreflector (if it is a Cassegrain feed) or the backside of the feed package (if it is a prime-focus feed). Measurement is desired of the quantity R, the vector from the center of the geocentric coordinate system, defined by the dynamics of the GPS constellation, to the intersection of axes of our antenna. The GPS antenna is offset from the intersection of axes by the vector R', and, at any given instant of time, the GPS receiver will measure the vector sum $R + R'$. Thus, the problem is reduced to the determination of R'.

In order to simplify the concept, first it is assumed that the antenna in question has already been aligned in a local coordinate system. The angular readouts have been adjusted to know precisely the direction of true north, i.e., the offsets in azimuth and elevation are known. If a measurement M_1 is made with the antenna pointed so that azimuth = A_1 and elevation = E_1, then three pieces of data are obtained: the $X1$, $Y1$, and $Z1$ coordinates of the GPS antenna relative to the center of the Earth. These are related to the three coordinates of the intersection of axes X, Y, and Z together with the magnitude of the offset vector $|R'|$. This results in three equations with six unknowns. Next, the antenna is pointed to another position, so that azimuth = A_2 and elevation = E_2, and another GPS measurement is made. Denote this measurement as M_2, providing $X2$, $Y2$, and $Z2$. This results in six pieces of data with six unknowns and allows a solution for the unknowns.

In practice, the azimuth and elevation offsets for the antenna may not be known beforehand. It is a relatively simple matter to include this in the vector formulation and, when this is done, eight quantities must be estimated. This will require the antenna to be moved to a third position, M_3, to obtain three additional pieces of data from which it is possible to solve for the eight unknowns, etc. The essence of this concept is the employment of the mathematics of multiparameter estimation to solve for something that cannot be measured directly. Critical to this approach is a model (i.e., a set of equations) that relates exactly how the quantity that can be measured relates to what can be inferred.

Real antennas are hardly ever as simple as has been assumed. Their axes never can be made to be exactly orthogonal, the offsets never determined exactly, one or both axes may wobble, etc. Real antennas sag and bend due to thermal effects. In principle, however, all of these effects can be modeled mathematically as rotation matrices and the parameters in the model determined by a sufficient number of measurements, as outlined above.

Obtaining an estimate of the intersection of axes is, of course, only the first part of the problem. It is necessary to understand the accuracy of that estimate, and that requires an error analysis. Measurement errors must be estimated and propagated through the estimation process in order to determine the error on the estimated quantity.

Measurement errors often can be reduced by using appropriate techniques. For instance, raw GPS measurements from a single-frequency receiver have a quoted accuracy of 30 m—hardly adequate for the problem previously described. However, understanding that propagation errors (troposphere and ionosphere) comprise the bulk of the error budget for a GPS measurement allows a considerable reduction of this error. For instance, location of a second GPS receiver somewhere in the vicinity of the GPS receiver on the antenna permits the use of differential measurements. While the individual GPS measurements might be accurate to 30 m, the differential measurements taken at the same time have a potential accuracy of a few mm and can be exploited to determine very precisely the model for the antenna.

Appendix B
Array Availability

Consider an array of n elements of equal G/T, where $n-m$ is required for successful operation, as discussed by Barlow et al. [1] and Jamnejad et al. [2]. The availability for each element is assumed to be equal to, but independent of, those for the other elements. No correlation is assumed between the failure rate or timing of different elements. Then the probability that at least $n-m$ elements are operating successfully at any given time can be calculated as follows. The probability that all the elements are operating successfully is

$$P_0 = p^n \tag{B-1}$$

and the probability that $n-1$ elements are operating successfully is equal to

$$P_1 = n(1-p)p^{n-1} \tag{B-2}$$

since this is the sum of n conditional probabilities for the case when one element is not functioning but the rest are. The probability that $n-2$ elements are operating successfully is then given by

$$p_2 = \left[\frac{n(n-1)}{2}\right](1-p)^2 p^{n-2} \tag{B-3}$$

This can be repeated until the case when only $n-m$ elements are operating, for which case we have

$$P_{n-m} = C(n,m)(1-p)^m p^{n-m} \tag{B-4}$$

in which

$$C(n,m) = \frac{n!}{[(n-m)!\,m!]} \tag{B-5}$$

is the number of combinations of m elements taken from a pool of n elements, and the "!" sign designates the factorial function.

The total probability of success for the array is then the sum of all the above cases,

$$P = \sum_{k=0}^{m} C(n,k)(1-p)^k\, p^{n-k} \tag{B-6}$$

which is also a form of the cumulative Bernoulli or binomial probability distribution function. Remember that we are comparing array elements having the same overall G/T. Assuming that T is more or less constant for the array, then the comparison is for array elements of equal G, or, equivalently, equal collecting aperture. Thus, for a total required collecting area of A (this can be either physical area or effective area, whichever is most convenient), the individual element area of an array of $n-m$ elements can be written as

$$A_{n-m} = \frac{a}{(n-m)} \tag{B-7}$$

Adding m marginal elements of area A_{n-m}, the incremental increase in the collecting area is mA_{n-m}, and the percentage of increase in the collecting area is given as

$$\frac{mA_{n-m}}{((n-m)A_{n-m})} = \frac{m}{(n-m)} \tag{B-8}$$

References

[1] R. E. Barlow and K. D. Heidtmann, "Computing *k-out-of-n* System Reliability," *IEEE Trans. on Reliability*, vol. R-33, no. 4, October 1984.

[2] V. Jamnejad, T. Cwik, and G. Resch, "Cost and Reliability Study for a Large Array of Small Reflector Antennas for JPL/NASA Deep Space Network (DSN)," *IEEE 1993 Aerospace Applications Conference Digest*, February 1993.

Appendix C
Demodulation Process

C.1 Signal Model

Carrying over Eq. (5.1-1) from Chapter 5 with some simplification, and assuming the signal has been digitally sampled, the received signal from a deep-space spacecraft can be modeled as

$$\begin{aligned} s_j &= \sqrt{2P}\sin\left[\theta_{cj} + \Delta d_j\, Sqr(\theta_{scj})\right] + n_j \\ &= \sqrt{2P_c}\sin\theta_{cj} + \sqrt{2P_d}\, d_j\, Sqr(\theta_{scj})\cos\theta_{cj} + n_j \end{aligned} \tag{C-1}$$

where s_j is the sample at time t_j. The carrier and data powers, denoted P_c and P_d, are given by $P\cos^2\Delta$ and $P\sin^2\Delta$, respectively, and P is the total received signal power, Δ is the modulation index, $\theta_{cj} = \omega_c t_j + \theta_c$ is the total carrier phase at sample time t_j, n_j is the sampled form of an additive bandlimited white Gaussian noise process, d_j is the sampled form of the NRZ or Manchester data with a symbol time of T_s, and $Sqr()$ designates the sin square-wave subcarrier with total phase $\theta_{scj} = \omega_{sc} t_j + \theta_{sc}$. Here the first component, the residual carrier, typically is tracked by a phase-locked loop, and the second component, the suppressed carrier, can be tracked by a Costas loop. The narrowband noise n_j can be written as

$$n_j = \sqrt{2}n_{cj}\cos\theta_{cj} - \sqrt{2}n_{sj}\sin\theta_{cj} \tag{C-2}$$

where n_{cj} and n_{sj} are sampled versions of the statistically independent, stationary, bandlimited white Gaussian noise processes with one-sided spectral

density level N_0 (W/Hz) and one-sided bandwidth B (Hz) that is large compared to $1/T_s$. The demodulation process requires carrier, subcarrier, and symbol synchronization. The following sections treat each of these subprocesses in order.

C.2 Carrier Demodulation

The reference signal for demodulating the carrier consists of an in-phase component (I) as well as a quadrature-phase component (Q). The Q-component is used to provide a tracking signal, while the I-component is used to obtain the actual data signal of interest. Thus, for the rest of this discussion, we will deal only with the I-component. The I-component reference signal is

$$r_{cj} = \sqrt{2}\cos\left(\hat{\theta}_{cj}\right) \tag{C-3}$$

where $\hat{\theta}_{cj}$ is the carrier-reference phase. Multiplying Eq. (C-1) by this reference signal yields

$$s'_j = \sqrt{P_c}\sin\phi_{cj} + \sqrt{P_d}\,d_j Sqr(\theta_{scj})C_{cj} + n'_{jj} \tag{C-4}$$

where the first term is due to any residual carrier and drops out as the carrier loop achieves lock. The second term is the data modulated onto the subcarrier, while the third term is the noise. The residual-carrier phase is $\phi_{cj} = \theta_{cj} - \hat{\theta}_{cj}$ and $C_{cj} = \cos\phi_{cj}$.

C.3 Subcarrier Demodulation

The reference signal for subcarrier demodulation, like the carrier, also has in-phase and quadrature-phase components:

$$r_{scj} = \begin{cases} Sqr\left(\hat{\theta}_{scj}\right) \\ Cqr\left(\hat{\theta}_{scj}\right) \end{cases} \tag{C-5}$$

where $\hat{\theta}_{scj}$ is the subcarrier-reference phase and $Cqr()$ designates the cosine subcarrier square wave. Multiplying Eq. (C-4) by this reference signal yields a result containing the two terms:

$$\begin{aligned} Sqr(\theta_{scj}) x Sqr\left(\hat{\theta}_{scj}\right) \underline{\Delta} C_{scj} &= \left(1 - \frac{2}{\pi}\left|\phi_{scj}\right|\right) \\ Sqr(\theta_{scj}) x Cqr\left(\hat{\theta}_{scj}\right) \underline{\Delta} S_{scj} &= \frac{2}{\pi}\phi_{scj} \end{aligned} \tag{C-6}$$

where $\phi_{scj} = \theta_{scj} - \hat{\theta}_{scj}$, $\left|\phi_{scj}\right| < (\pi W_{sc}/2)$, and W_{sc} is the window in the subcarrier loop. The second term of Eq. (C-6) is the quadrature component, and it drops out as the subcarrier loop achieves lock. The in-phase component of the signal then becomes

$$s_j'' = \sqrt{P_d}\, d_j\, C_{cj} C_{scj} + n_j'' \tag{C-7}$$

C.4 Symbol Demodulation

The symbol modulation, d_j, is characterized by

$$d_j = \sum_{k=-\infty}^{\infty} d_k\, p(t_j - T_s) \tag{C-8}$$

where $d_k = \pm 1$ are the binary data , and $p(t)$ is the square-wave function that has a value of 1 for $0 \le t_j < T_s$ and a zero value elsewhere. The final output of the receiver, v_k, is then achieved by summing samples over the length of one symbol time, T_s , to get

$$v_k = \sum_{j=k+\lambda_{syk}}^{k+T_s+\lambda_{syk}} s_j'' \tag{C-9}$$

where $\lambda_{syk} = (\theta_{syk} - \hat{\theta}_{sck})/2\pi = \phi_{syk}/2\pi$ is the delay offset due to the symbol phase error. The symbol portion of the summation collapses to

$$\sum_{j=k+\lambda_{syk}}^{k+T_s+\lambda_{syk}} d_j\, p(t_j - T_s) = \left(1 - \left|\lambda_{syk}\right|\right) d_k = \left(1 - \frac{1}{2\pi}\left|\phi_{syk}\right|\right) d_k \tag{C-10}$$

Setting $C_{syk} = \left(1 - [1/2\pi]\,|\,\phi_{syk}\,|\right)$, the final receiver output reduces to

$$v_k = \sqrt{P_d}\, C_{ck} C_{sck} C_{syk} d_k + n_k \tag{C-11}$$

In practice, the time variation represented by k in the three reduction functions, C_{ck}, C_{sck}, and C_{syk}, is small.

Appendix D
Gamma Factors for DSN Antennas

Table D-1 summarizes the γ_i factors, defined by Eq. (6.1-10), for several DSN antennas and both S-band and X-band. Conceptually, these gamma factors represent the antenna gain–noise temperature ratios normalized by the gain/noise temperature of the largest antenna. Here HEF denotes a high-efficiency antenna and STD a standard antenna. While the STD antennas are no longer in use, they have been retained in the table for reference purposes. Gamma factors were obtained from [1]. The numbers presented in the table should be used in a relative sense and not in an absolute sense. For example, for a three-element array of one 34-m HEF antenna and two 34-m STD antennas at S-band, the master antenna (in this case, the 34-m HEF) would have $\gamma_i = 1$ and the other two antennas would have $\gamma_2 = \gamma_3 = 0.13/0.26 = 0.5$.

Table D-1. Gamma factors for DSN antennas.

Antenna Size	Frequency Band	γ_i
70 m	S-band	1.00
34-m STD	S-band	0.17
34-m HEF	S-band	0.07
70 m	X-band	1.00
34-m STD	X-band	0.13
34-m HEF	X-band	0.26

Reference

[1] *Deep Space Network/Flight Project Interface Design Handbook*, Document 810-5, Rev. D, vol. I, modules TCI-10, TCI-30, and TLM-10, Jet Propulsion Laboratory, Pasadena, California, 1992.

Appendix E
Closed-Loop Performance

Typically, one would like to limit the IF combining losses expressed by Eq. (6.1-31) to some pre-specified maximum value, say $D_{\max}$. Solving Eq. (6.1-31) for $\sigma^2_{\Delta\phi\,\max}$, we obtain

$$\sigma^2_{\Delta\phi\,\max} < -2\ln\left[\frac{10^{D_{\max}/10}L-1}{L-1}\right] \tag{E-1}$$

The variance of the phase estimate can be reduced either by increasing the correlation time T in Eq. (6.1-12) or by tracking the phase-error process in a closed-loop fashion. Note that the value of B in Eq. (6.1-12) is set by the bandwidth of the telemetry spectrum and cannot be reduced at will.

In the simplest closed-loop implementation of the full-spectrum combining scheme, phase-error estimates can be updated using the following difference equation:

$$\hat{\theta}(n) = \hat{\theta}(n+1) + \alpha\phi(n) \tag{E-2}$$

where the value of α can be set between 0.2 and 0.5, and $\hat{\theta}(n)$ is the filtered phase-error estimate. The above difference equation gives the following loop transfer function:

$$G(z) = \frac{\hat{\Theta}(z)}{\Phi(z)} = \frac{\alpha}{z-1} \tag{E-3}$$

The variance of the closed-loop phase-error process now will be

$$\sigma_{i1}^2 = I_1 \sigma_{\Delta\phi\, i1}^2 = I_1 \frac{N_{01} N_{oi} B}{2 P_1 P_i T} \tag{E-4}$$

where

$$I_1 = \frac{1}{2\pi j} \oint |H(z)|^2 \frac{dz}{z} \tag{E-5}$$

and $H(z) = G(z)/(1 + G(z))$. Using the above $G(z)$, we obtain

$$I_1 = \frac{\alpha}{2 - \alpha} \tag{E-6}$$

As an example, for α = 0.2, I_1= 0.11, and the variance of the phase jitter is reduced by a factor of ten.

Appendix F
Subcarrier and Symbol-Loop SNR Performance

F.1 Subcarrier I- and IQ-Loops

Compared to the conventional subcarrier loop (unmodified), which employs the I-arm as shown in Fig. F-1, the modified subcarrier loop, depicted in Fig. F-2, utilizes both the I- and Q-arms of the baseband signal for tracking. The loop SNRs for both schemes are derived here and compared to the case when the carrier is locked. For CSC, the I- and Q-channels at the input of the subcarrier loop are respectively given as

$$\begin{aligned} I(t_i) &= \sqrt{P}d(t_i)Sqr\left(\Delta\omega_{sc}t_i + \theta_{sc}\right)\cos(\Delta\omega_c t_i) + n_I(t_i) \\ Q(t_i) &= \sqrt{P}d(t_i)Sqr\left(\Delta\omega_{sc}t_i + \theta_{sc}\right)\sin(\Delta\omega_c t_i) + n_Q(t_i) \end{aligned} \tag{F-1}$$

where $n_I(t_i)$ and $n_Q(t_i)$ are independent Gaussian noise processes and all other parameters were previously defined. As shown in Fig. F-2, both the I- and Q-components are multiplied by the square-wave references and averaged over one symbol period (assuming perfect symbol synchronization), resulting in [1]

$$\begin{aligned} I_s(k) &= \sqrt{P}d(k)\,f(\phi_{sc})\cos(\Delta\omega_c t_k) + n_{I\,s}(k) \\ I_c(k) &= \sqrt{P}d(k)\,g(\phi_{sc})\cos(\Delta\omega_c t_k) + n_{I\,c}(k) \\ Q_s(k) &= \sqrt{P}d(k)\,f(\phi_{sc})\sin(\Delta\omega_c t_k) + n_{I\,s}(k) \\ Q_c(k) &= \sqrt{P}d(k)\,g(\phi_{sc})\sin(\Delta\omega_c t_k) + n_{I\,c}(k) \end{aligned} \tag{F-2}$$

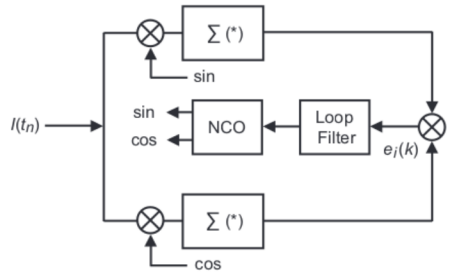

Fig. F-1. The unmodified subcarrier loop.

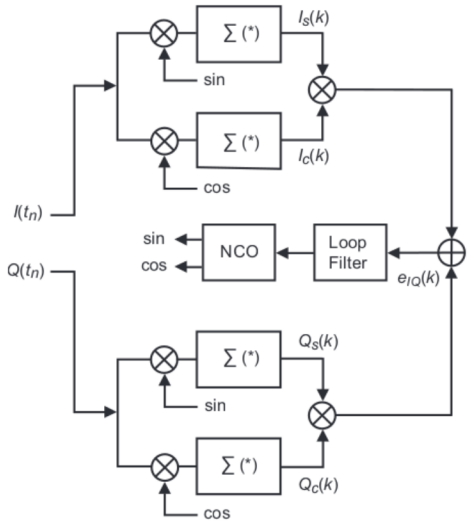

Fig. F-2. The modified subcarrier loop.

where k denotes the symbol index, $f(\phi_{sc}) = (1 - 2|\phi_{sc}|/\pi)$ for $|\phi_{sc}| \le \pi$, $g(\phi_{sc}) = 2\phi_{sc}/\pi$ for $|\phi_{sc}| \le \pi w_{sc}/2|, Var[n_{Is}(k)] = Var[n_{Ic}(k)] = Var[n_{Qs}(k)]$ $= \sigma_n^2 = N_0/2T_s$. The error signal of the conventional and modified subcarrier loops, respectively, are given as

$$\begin{aligned} e(k)_I &= P f(\phi_{sc}) g(\phi_{sc}) \cos^2(\Delta\omega_c t_k) + N_I(k) \\ e(k)_{IQ} &= P f(\phi_{sc}) g(\phi_{sc}) + N_{IQ}(k \end{aligned} \tag{F-3}$$

where the variances of the noise terms, respectively (after averaging over $\Delta\omega_c t_k$, assuming uniform distribution), are given as

$$\begin{aligned}\sigma^2_{N_{IQ}} &= P\sigma_n^2 + 2\sigma_n^4 \\ \sigma^2_{N_I} &= P\sigma_n^2/2 + \sigma_n^4\end{aligned} \tag{F-4}$$

The slope of the phase detector response curve can now be found by taking the first derivative of the average error signal with respect to ϕ_{sc}, and afterwards setting $\phi_{sc} = 0$. Accordingly, the slopes of the conventional and modified subcarrier loops are given as

$$\begin{aligned}K^I_{g\,sc} &= \frac{1}{\pi}P \\ K^{IQ}_{g\,sc} &= \frac{2}{\pi}P\end{aligned} \tag{F-5}$$

Note the slope of the IQ-arm is identical to the slope of the I-arm when the carrier is locked [1]. Assuming linear theory, the loop SNR for the subcarrier loop is given as

$$\rho_{sc} = \frac{1}{2B_{sc}T_s}\frac{K_g^2}{\sigma_N^2} \tag{F-6}$$

where B_{sc} is the one-sided noise bandwidth of the loop. Simplifying, the I- and IQ-arm loop SNRs are respectively given as

$$\begin{aligned}\rho^I_{sc} &= \left(\frac{2}{\pi}\right)^2 \frac{P/N_0}{2B_{sc}\,w_{sc}}\left(1 + \frac{1}{PT_s/N_0}\right)^{-1} \\ \rho^{IQ}_{sc} &= \left(\frac{2}{\pi}\right)^2 \frac{P/N_0}{B_{sc}\,w_{sc}}\left(1 + \frac{1}{PT_s/N_0}\right)^{-1}\end{aligned} \tag{F-7}$$

For comparison, the I-arm loop SNR when the carrier is locked is given in Eq. (5.2-7). Figure F-3 illustrates the subcarrier-loop SNRs when the I-arm, IQ-arm, and the I-arm with the carrier locked are used. For low symbol SNRs, the I-arm has a loop SNR that is 6 dB lower than the case when the carrier is locked. Using the IQ-arm, however, recovers 3 dB of the 6 dB but at the expense of more hardware. At high symbol SNRs, the performance of the IQ-arm is identical to that of the I-arm when the carrier is locked.

The behavior of the I-arm and IQ-arm for the subcarrier loop is investigated when the carrier is actually locked. For the I-arm, the subcarrier is normalized by a slope that is less than the actual operating slope. Consequently, the

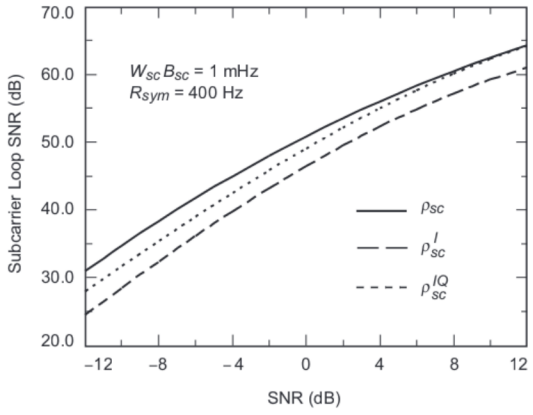

Fig. F-3. Subcarrier-loop SNR versus symbol SNR.

operating bandwidth of the loop is actually narrower that the one specified. Fortunately, for the IQ arm, the subcarrier is normalized by the correct slope.

F.2 Digital Data-Transition Tracking I- and IQ-Loops

Similar to the subcarrier loop, the conventional digital data-transition tracking loop (DTTL) shown in Fig. F-4 will be modified to utilize both the I- and Q-channels, as depicted in Fig. F-5. Assuming perfect subcarrier demodulation, the I- and Q-components for CSC are given as

$$\begin{aligned} I_k &= \sqrt{P}\, d_k \cos(\phi_c) + n_k^I \\ Q_k &= \sqrt{P}\, d_k \sin(\phi_c) + n_k^Q \end{aligned} \tag{F-8}$$

where n_k^I and n_k^Q are independent Gaussian random variables with variance $\sigma_n^2 = N_0/2T$ and $\phi_c = 2\pi\Delta f_c\, t + \theta_c$ is the difference between the predicted and actual IF carrier frequency.

The performance of the DTTL has been derived in [2] assuming the carrier is locked $(\phi_c = 0)$. When this is not the case, as in CSC, the loop suffers degradation, and the objective here is to quantify the decrease in performance for both the conventional and the modified DTTL. The analysis of the DTTL follows closely that of [2] with the difference now being that the data are modulated by a slowly varying cosine function. Assuming the equivalent mathematical model of the DTTL in terms of a phase-locked loop (PLL), all the relevant parameters (slope of the S-curve and normalized equivalent noise spectrum) are derived conditioned on ϕ_c. Afterwards, these parameters are averaged over ϕ_c, assuming ϕ_c is uniformly distributed from $-\pi$ to π.

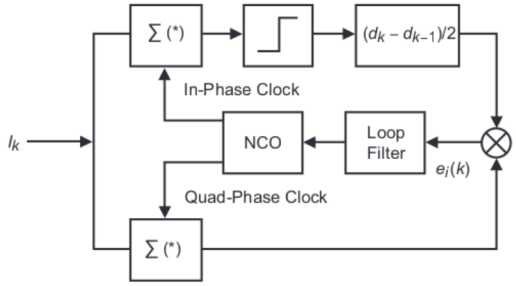

Fig. F-4. The unmodified digital DTTL.

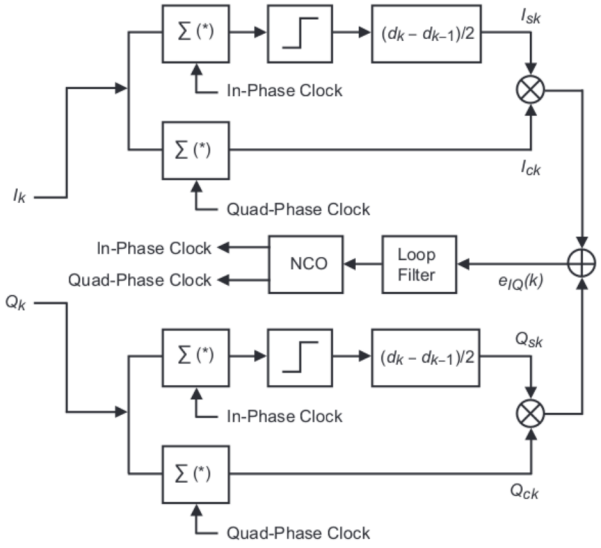

Fig. F-5. The modified digital DTTL.

The normalized mean of the error signal, e_k, conditioned on the normalized timing error, λ (in cycles), and the carrier predict error, ϕ_c, is the normalized phase detector characteristic $g_n(\lambda, \phi_c)$, commonly termed the loop S-curve. Following steps similar to those in [2], $g_n^I(\lambda, \phi_c)$ and $g_n^{IQ}(\lambda, \phi_c)$, the S-curves of the conventional and the modified DTTL, are respectively given as

$$
\begin{aligned}
g_n^I(\lambda,\phi_c) &= \lambda\left|\cos(\phi_c)\right|\mathrm{erf}(B) - \frac{w_{sy}-2\lambda}{8}\left|\cos(\phi_c)\right|\left[\mathrm{erf}(A)-\mathrm{erf}(B)\right] \\
g_n^{IQ}(\lambda,\phi_c) &= \lambda\left|\cos(\phi_c)\right|\mathrm{erf}(B) + \lambda\left|\sin(\phi_c)\right|\mathrm{erf}(B') \\
&\quad - \frac{w_{sy}-2\lambda}{8}\left|\cos(\phi_c)\right|\left[\mathrm{erf}(A)-\mathrm{erf}(B)\right] \\
&\quad - \frac{w_{sy}-2\lambda}{8}\left|\sin(\phi_c)\right|\left[\mathrm{erf}(A')-\mathrm{erf}(B')\right]
\end{aligned}
\tag{F-9}
$$

where
$A=\sqrt{E_s/N_0}\left|\cos(\phi_c)\right|$, $A'=\sqrt{E_s/N_0}\left|\sin(\phi_c)\right|$, $B=\sqrt{E_s/N_0}\,(1-2\lambda)\left|\cos(\phi_c)\right|$, and $B'=\sqrt{E_s/N_0}\,(1-2\lambda)\left|\sin(\phi_c)\right|$. To compute the S-curve conditioned only on λ, $g_n^I(\lambda,\phi_c)$ and $g_n^{IQ}(\lambda,\phi_c)$ are numerically integrated over ϕ_c, assuming uniform distribution. Setting ϕ_c to zero in Eq. (F-9) results in the same S-curve as in [2].

The first derivative of the S-curve at $\lambda=0$ is given as

$$
\begin{aligned}
K_{g,sy}^I(\phi_c) &= \left|\cos(\phi_c)\right|\mathrm{erf}(A) - \frac{w_{sy}}{2}\cos^2(\phi_c)\sqrt{\frac{E_s}{N_0\pi}}\,e^{-A^2} \\
K_{g,sy}^{IQ}(\phi_c) &= \left|\cos(\phi_c)\right|\mathrm{erf}(A) - \frac{w_{sy}}{2}\cos^2(\phi_c)\sqrt{\frac{E_s}{N_0\pi}}\,e^{-A^2} \\
&\quad + \left|\sin(\phi_c)\right|\mathrm{erf}(A') - \frac{w_{sy}}{2}\sin^2(\phi_c)\sqrt{\frac{E_s}{N_0\pi}}\,e^{-A'^2}
\end{aligned}
\tag{F-10}
$$

where $K_{g,sy}^I(\phi_c)$ and $K_{g,sy}^{IQ}(\phi_c)$ denote the slope of the S-curve for the conventional and modified DTTLs, respectively, conditioned on ϕ_c. Numerically integrating over the carrier phase, ϕ_c, results in the unconditional slopes, respectively denoted $K_{g,sy}^I$ and $K_{g,sy}^{IQ}$. Setting ϕ_c in Eq. (F-10) to zero results in

$$
K_{g,sy} = \mathrm{erf}\left(\sqrt{\frac{E_s}{N_0}}\right) - \frac{w_{sy}}{2}\sqrt{\frac{E_s}{N_0\pi}}\,e^{-E_s/N_0} \tag{F-11}
$$

which is identical to the slope given in [2]. Figure F-6 lists the ratio of $K_{g,sy}^I/K_{g,sy}$ and $K_{g,sy}^{IQ}/K_{g,sy}$ for different symbol SNRs and window sizes. At low symbol SNR, $K_{g,sy}$ and $K_{g,sy}^{IQ}$ are about the same, while $K_{g,sy}^I$ is about twice as large.

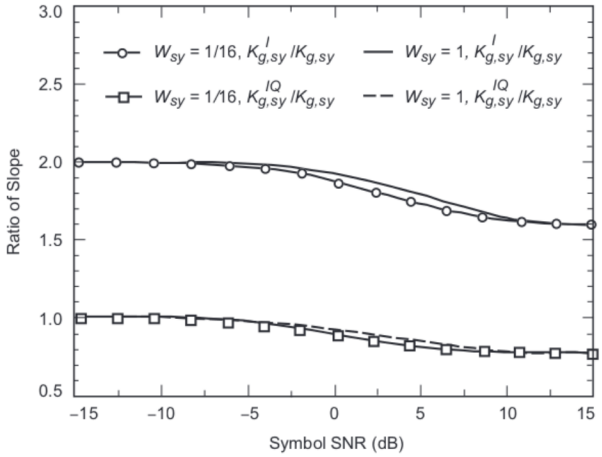

Fig. F-6. DTTL symbol versus ratio of slope.

Also, the normalized noise spectrum at $\lambda = 0$ can be shown to be

$$h^{I}(0,\phi_c) = 1 + 0.5\,w_{sy}\frac{E_s}{N_0}\cos^2(\phi_c) - \frac{w_{sy}}{2}\left[\frac{1}{\sqrt{\pi}}e^{-A^2} + \sqrt{\frac{E_s}{N_0}}\left|\cos(\phi_c)\right|\mathrm{erf}(A)\right]^2$$

$$h^{IQ}(0,\phi_c) = 2 + 0.5\,w_{sy}\frac{E_s}{N_0} - \frac{w_{sy}}{2}\left[\frac{1}{\sqrt{\pi}}e^{-A^2} + \sqrt{\frac{E_s}{N_0}}\left|\cos(\phi_c)\right|\mathrm{erf}(A)\right]^2$$
$$- \frac{w_{sy}}{2}\left[\frac{1}{\sqrt{\pi}}e^{-A'^2} + \sqrt{\frac{E_s}{N_0}}\left|\sin(\phi_c)\right|\mathrm{erf}(A')\right] \qquad \text{(F-12)}$$

where $h^{I}(0,\phi_c)$ and $h^{IQ}(0,\phi_c)$ denote the normalized noise spectra for the conventional and modified DTTLs, respectively, conditioned on ϕ_c. Numerically integrating over the carrier phase, ϕ_c, results in the unconditional normalized noise spectra, respectively denoted as $h^{I}(0)$ and $h^{IQ}(0)$. Setting ϕ_c in Eq. (F-12) to zero results in

$$h^{I}(0) = 1 + 0.5\,w_{sy}\frac{E_s}{N_0} - \frac{w_{sy}}{2}\left[\frac{1}{\sqrt{\pi}}e^{-E_s/N_0} + \sqrt{R_s}\,\mathrm{erf}\left(\sqrt{\frac{E_s}{N_0}}\right)\right]^2 \qquad \text{(F-13)}$$

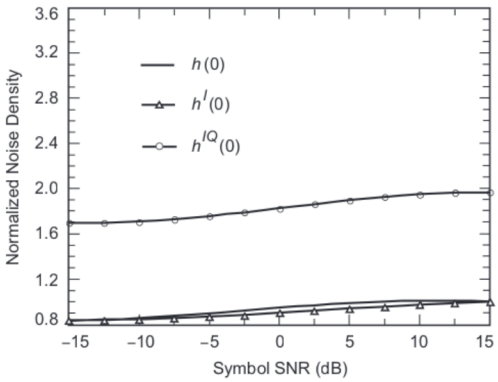

Fig. F-7. DTTL symbol SNR versus normalized noise density.

which is the same as the normalized noise spectrum given in [2]. Figure F-7 lists values of $h(0)$, $h^I(0)$, and $h^{IQ}(0)$ for different symbol SNRs at $w_{sy} = 1$. It is evident that $h(0)$ is slightly greater than $h^{IQ}(0)$ but significantly less than $h^I(0)$.

Assuming linear theory, the loop SNR for the DTTL is given as

$$\rho_{sy} = \frac{1}{2\pi^2} \frac{P}{N_0 w_{sy} B_{sy}} \mathrm{L} \tag{F-14}$$

where $\mathrm{L} = K_{g,sy}^2 / h(0)$. Furthermore, the loop SNRs for the conventional and modified DTTLs, denoted ρ_{sy}^I and ρ_{sy}^{IQ}, are found by normalizing Eq. (F-14) by $\mathrm{L}^I = (K_{g,sy}^I)^2 / h^I(0)$ or $\mathrm{L}^{IQ} = (K_{g,sy}^{IQ})^2 / h^{IQ}(0)$, respectively. Figure F-8 illustrates the loop SNR of the DTTL using the I-arm, IQ-arm, and I-arm when the carrier is locked. At low symbol SNR, it is clear that using only the I-arm reduces the loop SNR by 6 dB as compared to the case when the carrier is locked, and that utilizing the IQ-arm recovers 3 dB of the 6 dB.

The behavior of the I- and IQ-arms for the symbol loop is investigated when the carrier is actually locked. For the I-arm, the symbol loop is normalized by a slope that is less than the actual operating slope, as shown in Fig. F-6. Consequently, the operating bandwidth of the loop is actually narrower than the one specified. Fortunately, for the IQ-arm at a low symbol SNR, the symbol loop is normalized by the correct slope. For a high symbol SNR, however, the symbol loop for the IQ-arm is normalized by a slope that is greater than the actual operating slope. Consequently, the operating bandwidth of the loop is actually wider than the one specified.

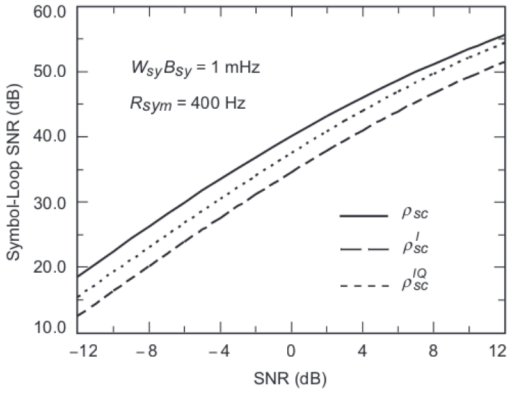

Fig. F-8. Symbol-loop SNR versus symbol SNR.

References

[1] W. J. Hurd and S. Aguirre, "A Method to Dramatically Improve Subcarrier Tracking," *The Telecommunications and Data Acquisition Progress Report 42-86, April–June 1986*, Jet Propulsion Laboratory, Pasadena, California, pp. 103–110, August 15, 1986. http://ipnpr.jpl.gov/progress_report/

[2] M. K. Simon, "Analysis of the Steady State Phase Noise Performance of a Digital Data-Transition Tracking Loop," *Space Programs Summary 37-55*, Jet Propulsion Laboratory, Pasadena, California, vol. 3, pp. 54–62, February 1969.

Appendix G
Derivation of Equations for Complex-Symbol Combining

G.1 Derivation of Eq. (6.2-5)

Substituting Eq. (6.2-2) into Eq. (6.2-4), one obtains

$$\mathbf{v}_k = \sum_{i=1}^{L} \beta_i \left(\sqrt{P_i}\, C_{sc\,i} C_{syi} d_k e^{j[\Delta\omega_c t_k + \Delta\phi_{i1}]} + \mathbf{n}_{k\,i} e^{-j\hat{\theta}_{i1}} \right) \tag{G-1}$$

where $\Delta\phi_{i1} = \theta_{i1} - \hat{\theta}_{i1}$ and all other symbols are defined in Eq. (6.2-1). The conditional combined power, denoted P', in Eq. (6.2-5) is found by deriving the conditional mean of $\mathbf{v}_k$, i.e.,

$$\begin{aligned} P' &= \mathrm{E}\left[\mathbf{v}_k \mid \phi_{sc_i}, \phi_{sy_i}, \Delta\phi_{i1} \right] \mathrm{E}^{*}\left[\mathbf{v}_k \mid \phi_{sc_j}, \phi_{sy_j}, \Delta\phi_{j1} \right] \\ &= \sum_{i=1}^{L} \sum_{j=1}^{L} \beta_i \beta_j \sqrt{P_i} \sqrt{P_j} C_{sc\,i} C_{sy\,i} C_{sc\,j} C_{sy\,j} e^{j[\Delta\phi_{i1} + \Delta\phi_{j1}]} \end{aligned} \tag{G-2}$$

which simplifies to Eq. (6.2-7). In addition, the phase $\theta_{\mathbf{v}}$ in Eq. (6.2-5) is given as

$$\theta_{\mathbf{v}} = \tan^{-1}\left[\frac{\Im\left[\sum_{i=1}^{L}\beta_i\sqrt{P_i}\,C_{sci}C_{syi}e^{j[\Delta\omega_c t_k+\Delta\phi_{i1}]}\right]}{\Re\left[\sum_{i=1}^{L}\beta_i\sqrt{P_i}\,C_{sci}C_{syi}e^{j[\Delta\omega_c t_k+\Delta\phi_{i1}]}\right]}\right] \tag{G-3}$$

G.2 Derivation of Eq. (6.2-11)

Let C_{syi} be the signal-reduction function due to symbol-timing errors in the ith symbol-synchronization loop. Then the ith matched-filter output in Eq. (6.2-2) can be rewritten as

$$\mathbf{v}_{ki} = \sqrt{P_i}C_{sci}C_{syi}d_k e^{j[\Delta\omega_c t_k+\theta_{i1}]} + \mathbf{n}_{ki} \tag{G-4}$$

The relative phase difference between antenna i and the reference antenna is estimated by performing the correlation operation shown in Fig. 6-8. Assuming perfect time alignment, the correlation output, $\mathbf{v}$, is given as

$$\mathbf{v} = \sum_{k=1}^{N}\mathbf{v}_{ki}\mathbf{v}_{k1}^{*} \tag{G-5}$$

where $N = T/T_s$ is the number of symbols used in the correlation. The correlation time and symbol time are denoted as T and T_s, respectively. Substituting the expressions for $\mathbf{v}_{ki}$ and $\mathbf{v}_{k1}$ into Eq. (G-5) (the performance of the full-spectrum correlator) yields

$$\mathbf{v} = \sqrt{P_1P_i}C_{sc1}C_{syi}C_{sc1}C_{syi}e^{j\theta_{i1}} + \mathbf{n}_{\mathbf{v}} \tag{G-6}$$

where

$$\mathrm{Var}(\mathbf{n}_{\mathbf{v}}) = 2P_1\overline{C_{sc1}^2}\,\overline{C_{sy1}^2}\frac{N_{0i}}{2T} + 2P_i\overline{C_{sci}^2}\,\overline{C_{syi}^2}\frac{N_{01}}{2T} + 2\frac{N_{01}N_{0i}}{2T_sT} \tag{G-7}$$

Defining the SNR for complex signals as $\mathrm{SNR} = E(\mathbf{v})E(\mathbf{v}^{*})/Var(\mathbf{v})$, the correlator SNR between antenna i and antenna 1 for CSC is given as

$$\mathrm{SNR}_{csci1} = \frac{\sqrt{P_1P_i}\,\overline{C}_{sc1}\overline{C}_{sci}\overline{C}_{sy1}\overline{C}_{syi}}{P_1\overline{C_{sc1}^2}\,\overline{C_{sy1}^2}\frac{N_{0i}}{T} + P_i\overline{C_{sci}^2}\,\overline{C_{syi}^2}\frac{N_{01}}{T} + \frac{N_{01}N_{0i}}{T_sT}} \tag{G-8}$$

and simplifying yields Eq. (6.2-11).

General Reference List

D. Abraham, "Science and Mission Perspective," Review of 70-m Long Term Equivalent Capability Study (JPL internal document), Jet Propulsion Laboratory, Pasadena, California, April 2001.

D. S. Abraham, "Identifying Future Mission Drivers on the Deep Space Network," SpaceOps 2002, October 9–12, 2002.

ASTRON, SKA Development, Dwingeloo, Netherlands, Technical Case, June 2002.

D. Bagri, "Prototype Array System Design," JPL informal review (internal document), Jet Propulsion Laboratory, Pasadena, California, 2001.

D. S. Bagri, "Prototype Array System," *Array Technology—FY02 Progress Report*, Jet Propulsion Laboratory, Pasadena, California, September 17, 2002

R. E. Barlow and K. D. Heidtmann, "Computing *k-out-of-n* System Reliability," *IEEE Trans. on Reliability*, vol. R-33, no. 4, October 1984.

C. D. Bartok, "Performance of the Real-Time Array Signal Combiner During the Voyager Mission," *The Telecommunications and Data Acquisition Progress Report 42-63, March and April 1981*, Jet Propulsion Laboratory, Pasadena, California, pp. 191–202, June 15, 1981.
http://ipnpr.jpl.nasa.gov/progress_report/

M. H. Brockman, "The Effect of Partial Coherence in Receiving System Noise Temperature on Array Gain for Telemetry and Radio Frequency Carrier Reception for Similar Receiving Systems," *The Telecommunications and Data Acquisition Progress Report 42-66, September and October 1981*, Jet Propulsion Laboratory, Pasadena, California, pp. 219–235, December 15, 1981.
http://ipnpr.jpl.nasa.gov/progress_report/

M. H. Brockman, "Enhanced Radio Frequency Carrier Margin Improvement for an Array of Receiving Systems With Unequal Predetection Signal-to-Noise Ratios," *The Telecommunications and Data Acquisition Progress Report 42-76, October–December 1983,* Jet Propulsion Laboratory, Pasadena, California, pp. 170–188, February 15, 1984. http://ipnpr.jpl.nasa.gov/progress_report/

M. H. Brockman, "Performance Characteristics for an Array of Two Receiving Systems with Equal Apertures and Enhanced Radio Frequency Carrier Margin Improvement," *The Telecommunications and Data Acquisition Progress Report 42-84, October–December 1985*, Jet Propulsion Laboratory, Pasadena, California, pp. 112–126, February 16, 1986.
http://ipnpr.jpl.nasa.gov/progress_report/

M. H. Brockman, "Performance Characteristics for an Array of Two Receiving Systems with Unequal Predetection Signal-to-Noise Ratios and Enhanced Radio Frequency Carrier Margin Improvement," *The Telecommunications and Data Acquisition Progress Report 42-84, October–December 1985*, Jet Propulsion Laboratory, Pasadena, California, pp. 101–111, February 16, 1986. http://ipnpr.jpl.nasa.gov/progress_report/

M. H. Brockman, "Radio-Frequency Carrier Arraying for High-Rate Telemetry Reception," *The Deep Space Network Progress Report 42-45, March and April 1978*, Jet Propulsion Laboratory, Pasadena, California, pp. 209–223, June 15, 1978. http://ipnpr.jpl.nasa.gov/progress_report/

M. H. Brockman, "Radio Frequency Carrier Arraying for Near Maximum Carrier Signal-to-Noise Ratio Improvement," *The Deep Space Network Progress Report 42-49, November and December 1978*, Jet Propulsion Laboratory, Pasadena, California, pp. 99–106, February 15, 1979. http://ipnpr.jpl.nasa.gov/progress_report/

D. W. Brown, W. D. Brundage, J. S. Ulvestad, S. S. Kent, and K. P. Bartos, "Interagency Telemetry Arraying for Voyager–Neptune Encounter," *The Telecommunications and Data Acquisition Progress Report 42-102, April–June 1990*, Jet Propulsion Laboratory, Pasadena, California, pp. 91–118, August 15, 1990. http://ipnpr.jpl.nasa.gov/progress_report/

D. W. Brown, H. W. Cooper, J. W. Armstrong, and S. S. Kent, "Parkes-CDSCC Telemetry Array: Equipment Design," *The Telecommunications and Data Acquisition Progress Report 42-85, January–March 1986*, Jet Propulsion Laboratory, Pasadena, California, pp. 85–110, May 15, 1986. http://ipnpr.jpl.nasa.gov/progress_report/

S. A. Butman, L. J. Deutsch, R. G. Lipes, and R. L. Miller, "Sideband-Aided Receiver Arraying," *The Telecommunications and Data Acquisition Progress Report 42-67, November–December 1981*, Jet Propulsion Laboratory, Pasadena, California, pp. 39–53, February 15, 1982. http://ipnpr.jpl.nasa.gov/progress_report/

K.-M. Cheung, "Eigen Theory for Optimal Signal Combining: A Unified Approach," *The Telecommunications and Data Acquisition Progress Report 42-126, April–June 1996*, Jet Propulsion Laboratory, Pasadena, California, pp. 1–9, August 15, 1996. http://ipnpr.jpl.nasa.gov/progress_report/

M. Connally, "Prototype Array System Requirements," DSMS 828-042, D-24531, Jet Propulsion Laboratory, Pasadena, California, August 2002.

D. DeBoer and J. Dreher, "A System Level Description of the ATA," ATA Memorandum no. 23, Radio Astronomy Laboratory, University of California, Berkeley, April 6, 2001.

R. J. Dewey, "The Effects of Correlated Noise in Intra-Complex DSN Arrays for S-Band Galileo Telemetry Reception," *The Telecommunications and Data Acquisition Progress Report 42-111, July–September 1992*, Jet Propulsion Laboratory, Pasadena, California, pp. 129–152 November 15, 1992. http://ipnpr.jpl.nasa.gov/progress_report/

R. M. Dickinson, D. L. Losh, R. D. Barber, and J. K. Dempsey, "A Phase-Control Approach for a Large-Element Coherent Microwave Power Uplink System," *IEEE Transactions on Antennas and Propagation*, vol. 47, no. 3, 1999.

D. Divsalar, "Symbol Stream Combining Versus Baseband Combining for Telemetry Arraying," *The Telecommunications and Data Acquisition Progress Report 42-74, April–June 1983*, Jet Propulsion Laboratory, Pasadena, California, pp. 13–28, August 15, 1983. http://ipnpr.jpl.nasa.gov/progress_report/

D. Divsalar, D. Hansen, and J. H. Yuen, "The Effect of Noisy Carrier Reference on Telemetry with Baseband Arraying," *The Telecommunications and Data Acquisition Progress Report 42-63, March and April 1981*, Jet Propulsion Laboratory, Pasadena, California, pp. 128–135, June 15, 1981. http://ipnpr.jpl.nasa.gov/progress_report/

D. Divsalar and J. H. Yuen, "Improved Carrier Tracking Performance with Coupled Phase-Locked Loops," *The Telecommunications and Data Acquisition Progress Report 42-66, September and October 1981*, Jet Propulsion Laboratory, Pasadena, California, pp. 148–171, December 15, 1981. http://ipnpr.jpl.nasa.gov/progress_report/

DSMS Telecommunications Link Design Handbook, JPL 810-5, D-10379, Rev. E, Jet Propulsion Laboratory, Pasadena, California, January 2001.

Y. Feria, "A Complex Symbol Signal-to-Noise Ratio Estimator and Its Performance," *The Telecommunications and Data Acquisition Progress Report 42-116, October–December 1993*, Jet Propulsion Laboratory, Pasadena, California, pp. 232–245, February 15, 1984.
http://ipnpr.jpl.nasa.gov/progress_report/

Y. Feria and J. Statman, "Signal-to-Noise Ratio Losses in Full Spectrum Combining of Signals With a Downconverted Subcarrier," *The Telecommunications and Data Acquisition Progress Report 42-113, January–March 1993*, Jet Propulsion Laboratory, Pasadena, California, pp. 123–129, May 15, 1993. http://ipnpr.jpl.nasa.gov/progress_report/

D. Fort, *Array Preliminary Design Review* (internal document), Jet Propulsion Laboratory, Pasadena, California, January 1998.

R. M. Hjellming, ed., *An Introduction to the NRAO Very Large Array*, National Radio Astronomy Observatory, Socorro, New Mexico, April 1993.

W. J. Hurd and S. Aguirre, "A Method to Dramatically Improve Subcarrier Tracking," *The Telecommunications and Data Acquisition Progress Report 42-86, April–June 1986*, Jet Propulsion Laboratory, Pasadena, California, pp. 103–110, August 15, 1986. http://ipnpr.jpl.gov/progress_report/

W. J. Hurd, F. Pollara, M. D. Russell, B. Siev, and P. U. Winter, "Intercontinental Antenna Arraying by Symbol Stream Combining ICE Giacobini-Zinner Encounter," *The Telecommunications and Data Acquisition Progress Report 42-84, October–December 1985*, Jet Propulsion Laboratory, Pasadena, California, pp. 220–228, February 15, 1986.
http://ipnpr.jpl.nasa.gov/progress_report/

W. Hurd, J. Rabkin, M. D. Russell, B. Siev, H. W. Cooper, T. O. Anderson, and P. U. Winter, "Antenna Arraying of Voyager Telemetry Signals by Symbol Stream Combining," *The Telecommunications and Data Acquisition Progress Report 42-86, April–June 1986*, Jet Propulsion Laboratory, Pasadena, California, pp. 132–142, August 15, 1986.
http://ipnpr.jpl.nasa.gov/progress_report/

W. J. Hurd, L. J. Reder, and M. D. Russell, "Symbol-Stream Combiner: Description and Demonstration Plans," *The Telecommunications and Data Acquisition Progress Report 42-78, April–June 1984*, Jet Propulsion Laboratory, Pasadena, California, pp. 115–121, August 15, 1984. http://ipnpr.jpl.nasa.gov/progress_report/

V. Jamnejad, T. Cwik, and G. Resch, "Cost and Reliability Study for a Large Array of Small Reflector Antennas for JPL/NASA Deep Space Network (DSN)," *IEEE 1993 Aerospace Applications Conference Digest*, February 1993.

R. Kahn, *Array Preliminary Design Review* (internal document), Jet Propulsion Laboratory, Pasadena, California, January 1998.

J. W. Layland and D.W. Brown, "Planning for VLA/DSN Arrayed Support to the Voyager at Neptune," *The Telecommunications and Data Acquisition Progress Report 42-82, April–June 1985*, Jet Propulsion Laboratory, Pasadena, California, pp. 125–135, August 15, 1985.
http://ipnpr.jpl.nasa.gov/progress_report/

J. W. Layland, F. D. McLaughlin, P. E. Beyer, D. J. Mudgway, D. W. Brown, R. W. Burt, R. J. Wallace, J. M. Ludwindki, B. D. Madsen, J. C. McKinney, N. Renzetti, and J. S. Ulvestad, "Galileo Array Study Team Report," *The Telecommunications and Data Acquisition Progress Report 42-103, July–September 1990*, Jet Propulsion Laboratory, Pasadena, California, pp. 161–169, November 15, 1990. http://ipnpr.jpl.nasa.gov/progress_report/

J. W. Layland, P. J. Napier, and A. R. Thompson, "A VLA Experiment—Planning for Voyager at Neptune," *The Telecommunications and Data Acquisition Progress Report 42-82, April–June 1985*, Jet Propulsion Laboratory, Pasadena, California, pp. 136–142, August 15, 1985. http://ipnpr.jpl.nasa.gov/progress_report/

J. W. Layland, A. M. Ruskin, D. A. Bathker, R. C. Rydgig, D. W. Brown, B. D. Madsen, R. C. Clauss, G. S. Levy, S. J. Kerridge, M. J. Klein, C. E. Kohlhase, J. I. Molinder, R. D. Shaffer, and M. R. Traxler, "Interagency Array Study Report," *The Telecommunications and Data Acquisition Progress Report 42-74, April–June 1983*, Jet Propulsion Laboratory, Pasadena, California, pp. 117–148, Aug. 15, 1983. http://ipnpr.jpl.nasa.gov/progress_report/

W. Lindsey and M. K. Simon, *Telecommunication Systems Engineering*, New Jersey: Prentice-Hall, 1973.

A. Mileant and S. Hinedi, "Costas Loop Lock Detection in the Advanced Receiver," *The Telecommunications and Data Acquisition Progress Report 42-99, July–September 1989*, Jet Propulsion Laboratory, Pasadena, pp. 72–89, November 15, 1989. http://ipnpr.jpl.nasa.gov/progress_report/

A. Mileant and S. Hinedi, "Overview of Arraying Techniques in the Deep Space Network," *The Telecommunications and Data Acquisition Progress Report 42-104, October–December 1990*, Jet Propulsion Laboratory, Pasadena, California, pp. 109–139, February 15, 1991.
http://ipnpr.jpl.nasa.gov/progress_report/

S. Million, B. Shah, and S. Hinedi, "A Comparison of Full-Spectrum and Complex-Symbol Combining Techniques for the Galileo S-Band Mission," *The Telecommunications and Data Acquisition Progress Report 42-116, October–December 1993*, Jet Propulsion Laboratory, Pasadena, California, pp. 128–162, February 15, 1994. http://ipnpr.jpl.nasa.gov/progress_report/

R. Navarro and D. Fort, "Signal Processing," *Array Technology—FY02 Progress Report*, Jet Propulsion Laboratory, Pasadena, California, September 17, 2002

T. T. Pham, A. P. Jongeling, and D. H. Rogstad, "Enhancing Telemetry and Navigation Performance with Full Spectrum Arraying," IEEE Aerospace Conference, Big Sky, Montana, March 2000.

T. T. Pham, S. Shambayati, D. E. Hardi, and S. G. Finley, "Tracking the Galileo Spacecraft With the DSCC Galileo Telemetry Prototype," *The Telecommunications and Data Acquisition Progress Report 42-119, July–September 1994*, Jet Propulsion Laboratory, Pasadena, California, pp. 221–235, November 15, 1994. http://ipnpr.jpl.nasa.gov/progress_report/

P. D. Potter, W. D. Merrick, and A. C. Ludwig, *Large Antenna Apertures and Arrays for Deep Space Communications*, JPL Technical Report 32-848, Jet Propulsion Laboratory, Pasadena, California, November 1, 1965.

G. M. Resch, T. A. Cwik, V. Jamnejad, R. T. Logan, R. B. Miller, and D. H. Rogstad, *Synthesis of a Large Communications Aperture Using Small Antenna*, JPL Publication 94-15, Jet Propulsion Laboratory, Pasadena, California, 1994.

D. H. Rogstad, "Suppressed Carrier Full-Spectrum Combining," *The Telecommunications and Data Acquisition Progress Report 42-107, July–September 1991*, Jet Propulsion Laboratory, Pasadena, California, pp. 12–20, November 15, 1991. http://ipnpr.jpl.nasa.gov/progress_report/

J. Ruze, "Antenna Tolerance Theory—A Review," *Proceedings of the IEEE*, vol. 54, no. 4, pp. 633–640, April 1966.

R. Sfeir, S. Aguirre, and W. J. Hurd, "Coherent Digital Demodulation of a Residual Signal Using IF Sampling," *The Telecommunications and Data Acquisition Progress Report 42-78, April–June 1984*, Jet Propulsion Laboratory, Pasadena, California, pp. 135–142, August 15, 1984. http://ipnpr.jpl.nasa.gov/progress_report/

M. Shihabi, T. Nguyen, and S. Hinedi, "A Comparison of Telemetry Signals in the Presence and Absence of Subcarrier," *IEEE Transactions on EMC*, vol. 76, no. 1, pp. 60–73, February 1994.

M. Shihabi, B. Shah, S. Hinedi, and S. Million, "Residual and Suppressed-Carrier Arraying Techniques for Deep-Space Communications," *The Telecommunications and Data Acquisition Progress Report 42-121, January–March 1995*, Jet Propulsion Laboratory, Pasadena, California, pp. 173–201, May 15, 1995. http://ipnpr.jpl.nasa.gov/progress_report/

M. K. Simon, "Analysis of the Steady State Phase Noise Performance of a Digital Data-Transition Tracking Loop," *Space Programs Summary 37-55*, Jet Propulsion Laboratory, Pasadena, California, vol. 3, pp. 54–62, February 1969.

M. K. Simon and A. Mileant, *Performance Analysis of the DSN Baseband Assembly Real-Time Combiner*, JPL Publication 84-94, Rev. 1, May 1, 1985.

J. I. Statman, "Optimizing the Galileo Space Communication Link," *The Telecommunications and Data Acquisition Progress Report 42-116, October–December 1993*, Jet Propulsion Laboratory, Pasadena, California, pp. 114–120, February 15, 1994. http://ipnpr.jpl.nasa.gov/progress_report/

C. T. Stelzried, A. L. Berman, and G. K. Noreen, "Antenna Arraying Performance for Deep Space Telecommunications Systems," *The Telecommunications and Data Acquisition Progress Report 42-72, October–December 1982*, Jet Propulsion Laboratory, Pasadena, California, pp. 83–88, February 15, 1983. http://ipnpr.jpl.nasa.gov/progress_report/

R. Stevens, "Applications of Telemetry Arraying in the DSN," *The Telecommunications and Data Acquisition Progress Report 42-72, October–December 1982*, Jet Propulsion Laboratory, Pasadena, California, pp. 78–82, February 15, 1983. http://ipnpr.jpl.nasa.gov/progress_report/

H. H. Tan, "Optimum Combining of Residual Carrier Array Signals in Correlated Noise," *The Telecommunications and Data Acquisition Progress Report 42-124, October–December 1995*, Jet Propulsion Laboratory, Pasadena, California, pp. 33–52, February 15, 1996.
http://ipnpr.jpl.nasa.gov/progress_report/

A. R. Thompson, J. M. Moran, and G. W. Swenson, Jr., *Interferometry and Synthesis in Radio Astronomy*, New York: Wiley, 1986.

J. S. Ulvestad, "Phasing the Antennas of the Very Large Array for Reception of Telemetry from Voyager 2 at Neptune Encounter," *The Telecommunications and Data Acquisition Progress Report 42-94, April–June 1988*, Jet Propulsion Laboratory, Pasadena, California, pp. 257–273, August 15, 1988. http://ipnpr.jpl.nasa.gov/progress_report/

U.S. Square-Kilometer Array Consortium, *The Square Kilometer Array, Preliminary Strawman Design Large N–Small D*, July 2002.

P. Vazirani, "Effects of Correlated Noise on the Full Spectrum Combining and Complex-Symbol Combining Arraying Techniques," *The Telecommunications and Data Acquisition Progress Report 42-121, January–March 1995*, Jet Propulsion Laboratory, Pasadena, California, pp. 211–241, May 15, 1995. http://ipnpr.jpl.nasa.gov/progress_report/

V. Vilnrotter and E. R. Rodemich, "Real-Time Combining of Residual Carrier Array Signals Using ML Weight Estimates," *IEEE Trans. Comm.*, vol. COM-40, no. 3, pp. 604–615, March 1992.

H. Wilck, "A Signal Combiner for Antenna Arraying," *The Deep Space Network Progress Report 42-25, November and December 1974*, Jet Propulsion Laboratory, Pasadena, California, pp. 111–117, February 15, 1975. http://ipnpr.jpl.nasa.gov/progress_report/

R. A. Winkelstein, "Analysis of the Signal Combiner for Multiple Antenna Arraying," *The Deep Space Network Progress Report 42-26, January and February 1975*, Jet Propulsion Laboratory, Pasadena, California, pp. 102-118, April 15, 1975. http://ipnpr.jpl.nasa.gov/progress_report/

J. Yuen, *Deep Space Telecommunications Systems Engineering*, New York: Plenum Press, 1983.

Acronyms and Abbreviations

A/D	analog-to-digital converter
BBA	baseband assembly
BC	baseband combining
BPSK	binary phase-shift keying
BWG	beam waveguide (DSN antenna)
CA	carrier arraying
CA/BC	carrier arraying with baseband combining
CA/SA/BC	carrier arraying with sideband aiding and baseband combining
CA/SSC	carrier arraying with symbol-stream combining
C-band	4 GHz
CPM	continuous phase modulation
CSC	complex-symbol combining
CSCA	complex-symbol combining with aiding
CSIRO	Commonwealth Scientific and Industrial Research Organization
D/A	digital-to-analog converter
dB	decibel
dB-Hz	decibel in one-hertz bandwidth
delta DOR	delta differential one-way ranging

DESCANSO	Deep Space Communications and Navigation Systems Center of Excellence
DSN	Deep Space Network
DSS	Deep Space Station
DTTL	data-transition tracking loop
EIRP	equivalent isotropic radiative power
FFT	fast Fourier transform
FPGA	field programmable gate array
FSC	full-spectrum combining Full Spectrum Combiner
FSPA	Full Spectrum Processing Array
FSPS	Full Spectrum Processing Subsystem
FSR	Full Spectrum Receiver
GHz	gigahertz
GPS	Global Positioning System
G*/*T	gain divided by temperature
HEF	high-efficiency (DSN antenna)
HEMT	high electron mobility transistor
Hz	hertz
I	in phase
IF	intermediate frequency
IQ	in phase/quadrature phase
JPL	Jet Propulsion Laboratory
K	kelvin
Ka-band	32 GHz
kHz	kilohertz
kb/s	kilobits per second
ksym/s	kilosymbols per second
Ku-band	13 GHz
LNA	low-noise amplifier
Mb/s	megabits per second
MER	Mars Exploration Rover
MHz	megahertz

mHz	millihertz
MMIC	monolithic microwave integrated circuit
Msym	megasymbol
Msym/s	megasymbols per second
NASA	National Aeronautics and Space Administration
NRZ	nonreturn to zero
pdf	probability density function
PLL	phase-locked loop
Q	quadrature phase
QPSK	quadrature phase-shift keying
RF	radio frequency
RFI	radio frequency interference
rms	root-mean-square
RTC	real-time combiner
s	second
SA	sideband aiding
S-band	2.3 GHz
SER	symbol-error rate
SKA	Square Kilometer Array
SNR	signal-to-noise ratio
s/s	symbols per second
SSC	symbol-stream combining
STD	standard (DSN antenna)
sym	symbol
VLA	Very Large Array
VLBI	very long baseline interferometry
W	watt
X-band	8.4 GHz